Reduction of Dimensionality in Karyopherinβ1 Mediated Transport on FG Domains

Inauguraldissertation
zur
Erlangung der Würde eines Doktors der Philosophie
vorgelegt der
Philosophisch-Naturwissenschaftlichen Fakultät
der Universität Basel

von

Kai D. Schleicher
aus Deutschland

Basel, 2016

Genehmigt von der Philosophisch-Naturwissenschaftlichen Fakultät

auf Antrag von

Prof. Dr. Roderick Lim

Dr. Sylvia Jeney

Basel, den 24. Juni 2014

Prof. Dr. Jörg Schibler

Dekan

Preface

"A drunk man will eventually return home but a drunk bird will loose its way in space."

This phrase, attributed to the Hungarian mathematician George Pólya, illustrates that finding one's destination by random diffusion is almost assured when moving in two dimensions. In three dimensions, however, the effort is guaranteed to fail.

Remarkably, many molecular transport processes in living cells proceed by facilitated diffusion in two dimensions instead of three, but how this process works remains poorly understood. Originally coined "reduction of dimensionality" (ROD) by Adam and the Nobel Laureate Max Delbrück in 1968, this phenomenon has been implicated to underlie the molecular transport that occurs through nuclear pore complexes (NPCs) in living cells [1], [2].

NPCs are remarkable molecular machines that perforate the nuclear envelope (NE) of eukaryotic cells and represent the sole regulator of molecular flux between the nucleus and cytoplasm [3]. Despite their putative diameters of ∼50 nm [4], NPC-mediated nucleocytoplasmic transport (NCT) is accomplished in an efficient and selective manner. The upper limit for passive transport through the NPC is ∼40 kDa [5], thus, small molecules diffuse freely through the NPC, whereas macromolecules >∼5 nm in size are withheld [6]. Exclusive access is limited to cargo-carrying transport receptors (karyopherins

or Kaps, e.g. Kapβ1), which interact with several intrinsically disordered Phe-Gly (FG)-repeat rich domains (i.e. FG domains) that pave the central pore. As each Kapβ1 molecule contains ~10 hydrophobic pockets that bind FG repeats, Kap-FG domain binding involves highly multivalent interactions, which are generally known to impart a strong avidity that enhances stability and specificity [7]. This is paradoxical in the context of the NPC, because the high submicromolar Kapβ1-FG domain binding affinities [8]–[10] predict slow kinetic off rates (given a diffusion-limited on rate) that contradict the rapid (∼5 ms) in vivo dwell time [11]. As this implies, Kap-FG binding ought to be sufficiently strong to ensure selectivity, but also weak enough to promote fast translocation through the NPC. Nonetheless, an explanation as to how Kap-FG interaction balances the tradeoff between mobility and specificity during NCT is still lacking.

The purpose of my PhD is to resolve this conundrum *in vitro* using optical trapping-based photonic force microscopy (PFM). By measuring the thermal fluctuations of Kap-functionalized colloidal probes in contact with FG domain layers, I found that Kap-FG interactions *per se* attenuate diffusive motion due to strong specific binding. Strikingly, this can be controlled by varying the amount of free Kaps in solution, which indirectly modulate FG binding site accessibility in the layer and produces differential behavior ranging from highly constrained to near-passive diffusion. With the optical trap switched off, I found that the probes exhibited two-dimensional diffusion at physiological Kap concentrations. In this dissertation I will explain how multivalent interactions strike a balance between binding affinity and Kap-facilitated mobility on FG domains, leading to "reduction of dimensionality" in selective transport processes with implications for the NPC.

Table of Contents

List of Figures

List of Tables

Glossary

AFM	Atomic-force microscopy
APTES	(3-Aminopropyl)triethoxysilane
ATP	Adenosine triphosphate
BSA	Bovine serum albumin
ConA	Concanavalin A
DTT	Dithiothreitol
EM	Electron-microscopy
EGFP	Enhanced GFP
FRAP	Fluorescence recovery after photobleaching
GA	Glutaraldehyde
GAP	GTPase-activating protein
GDP	Guanosine diphosphate
GEF	Guanine nucleotide exchange factor
GRAVY	Grand average of hydropathicity
GTP	Guanosine triphosphate
IDP	Intrinsically disordered protein
IMCF	Imaging Core facility
Kap	Karyopherin
Kapβ1	Karyopherin β1
MBL	Mannose-bindig lectins
MD	Molecular dynamics
MSD	Mean square displacement
Mw	Molecular weight
MWCO	Molecular weight cut-off

NA	Numerical aperture
NCT	Nucleocytoplasmic transport
NE	Nuclear envelope
NF	Neutral density filter
NLS	Nuclear localization signal
NPC	Nuclear pore complex
NTA	Nitrilotriacetic acid
Nup153	Nucleoporin 153
PAGE	Polyacrylamide gel electrophoresis
PBS	Phosphate buffered saline
PFM	Photonic force microscopy
PONDR	Predictors of natural disordered regions
PSD	Power spectrum density
QD	Quantum dot
ROD	Reduction of dimensionality
SD	Standard deviation
SDS	Sodium dodecyl sulfate
SEM	Standard error of the mean
SIM	Structured illumination microscopy
SPR	Surface plasmon resonance
Sulfo-SMCC	Sulfosuccinimidyl-4-(N-maleimidomethyl)cyclohexane-1-carboxylate
WGA	Wheat germ agglutinin

Chapter 1

1 Introduction

1.1 The Nuclear pore complex

Eukaryotes are considered a milestone in the evolution of life. The origin of prokaryotes like bacteria or archaea dates ~3.5 billion years back, whereas the oldest fossils of eukaryotic organisms are 1.8 billion years old [12]. In contrast to prokaryotes, they possess a double lipid bilayer called the nuclear envelope (NE) that engulfs their genetic material and defines the nucleus. Several advantages come with this structure: It protects the genome from external or internal causes of damage due to shear stress or large moving objects (e.g. cytoskeleton and organelles) and serves as a barrier that shields the DNA from pathogens like viruses. Moreover, the subdivision into nucleoplasm and cytoplasm allows for the efficient regulation of compartment specific processes. Specialized proteins and structures can localize predominantly to one compartment and therefore reach their effective concentration at lower copy numbers. For example, transcription of DNA to RNA via polymerases and subsequent processing to mRNA (e.g. capping, splicing) is confined to the nucleus, while mRNA translation to proteins by ribosomes is located in the cytoplasm. This spatial regulation of gene expression ensures that only mature mRNA is translated into proteins [13].

Despite these advantages, eukaryotes face the challenge to overcome the NE-barrier. For example, the cell must ensure that mature mRNA is exported into the cytoplasm, but at the same time allow transcription factors to travel into the nucleus to initiate transcription. This bidirectional traffic is accomplished by nuclear pore complexes (NPCs) that perforate the NE in large numbers (up to several thousand per cell [14]) and represent the sole gateway between the nucleus and the cytoplasm (Figure 1-1). The following examples illustrate some of its many remarkable properties.

(1) NPCs are highly promiscuous and manage the transport of a multitude of several distinct Kap-cargo-complexes in parallel through the same pore [11], [15], [16].
(2) NPCs are remarkably flexible and able to transport large cargos up to 39 nm in size [17].
(3) They possess a duality of function, being a molecular sorting machinery and transporter at the same time.
(4) No motor proteins are needed for translocation through NPCs. Energy is only required to impart transport directionality.
(5) Cargos are transported and accumulated inside their target compartment against concentration gradients.
(6) NPC access is based on binding affinity, but rather counterintuitively, nuclear accumulation of NPC-affine cargo is orders of magnitude more rapid than passively diffusing one, even when of similar size [15], [18].

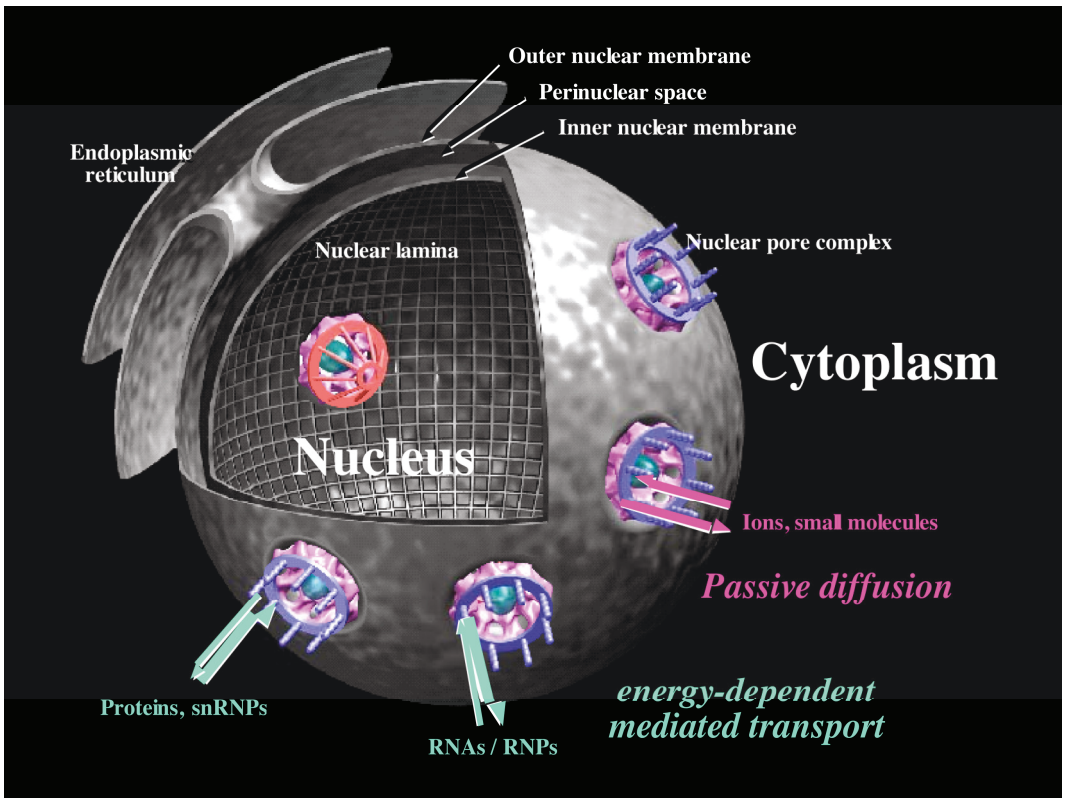

Figure 1-1 – Nuclear pore complexes perforate the NE of eukaryotic cells. NPCs are large macromolecular complexes located in the nuclear envelope of eukaryotes and represent the sole connection between the nucleus and the cytoplasm. They mediate all bidirectional traffic of macromolecules across the NE. While ions and small molecules below ~5 nm in size pass through NPCs by free diffusion, larger proteins like ribonucleoproteins (RNPs) require transport receptors for their directed import or export. With permission Ueli Aebi.

1.2 Thesis Layout

Chapter 1 introduces the NPC in terms of its structural and functional components. Current biochemical understanding of cargo translocation through nuclear pores is summarized and followed by a detailed account of present models that explain NPC functionality and its transport mechanism. Materials and methods concerning the proteins used in this work are introduced in **chapter 2** and followed by their characterization using a

combination of biochemical and biophysical methods. Thereafter, **chapter 3** introduces photonic force microscopy (PFM), the main measurement technique used in this work. Further, Kap-probe and cNup153-surface functionalization is explained and subsequently characterized. **Chapter 4** contains results obtained for local mobility of Kap-probes on a cNup153-layer measured with PFM, while results acquired on the ensemble probe-level are presented in **chapter 5**. Finally, **chapter 6** concludes the thesis and provides an outlook on future experiments.

1.3 Nuclear Pore Complex Structure and Composition

Each NPC is composed of about 30 different proteins, termed nucleoporins or Nups (Figure 1-2), that are present in multiple copies per NPC [19]. NPC size differs between species, but shares a common general makeup with an 8-fold symmetry (Figure 1-1b, d and e). Transmembrane Nups serve as anchor points to the NE and, together with linker Nups and inner ring Nups, constitute the NPCs central framework of ~40–90 nm height that surrounds the aqueous channel. The pore is lined with central channel Nups on its periphery and has an inner diameter of ~40–75 nm [20]–[24]. All central channel Nups contain intrinsically disordered domains rich in FG repeats (FG Nups), which are presumed to collectively contribute to a selective barrier that regulates cargo translocation through the NPC.

On the cytoplasmic side, the outer ring Nups and cytoplasmic FG Nups cover the central framework, with eight filaments extending into the cytoplasm for ~30–50 nm [21], [22], [25]. Likewise, FG Nups and outer ring Nups on the nuclear side are connected to a distal ring via eight filaments and form the

nuclear basket, which extends into the nucleoplasm for ~50–75 nm from the inner nuclear membrane [20]–[24] (Figure 1-2).

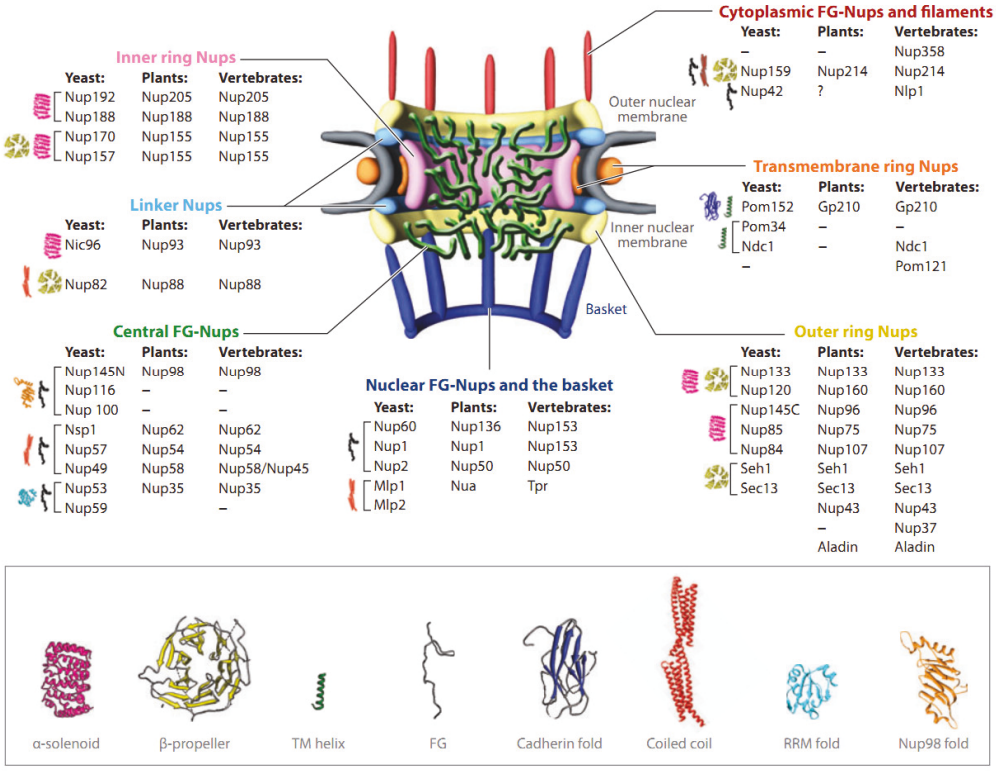

Figure 1-2 – Protein composition of the NPC. The Nups are grouped according to their position and structural characteristics. The central framework (outer ring Nups, linker Nups, inner ring Nups, TM ring Nups, and central FG Nups) is capped by FG Nups and filaments on the cytoplasmic and the basket on the nuclear side, respectively. The outer and inner nuclear membranes are depicted in gray. The structural motifs that appear next to each Nup refer to the predicted protein fold in yeast and are described in the legend. Reproduced from Grossman *et al.* [14].

1.4 Nucleocytoplasmic Transport

Successful transport between nucleus and cytoplasm of cargo molecules larger than 5 nm in size is accomplished by a sequence of protein-protein interactions that is orchestrated by Kaps that exhibit exclusive access through NPCs [26] (Figure 1-3).

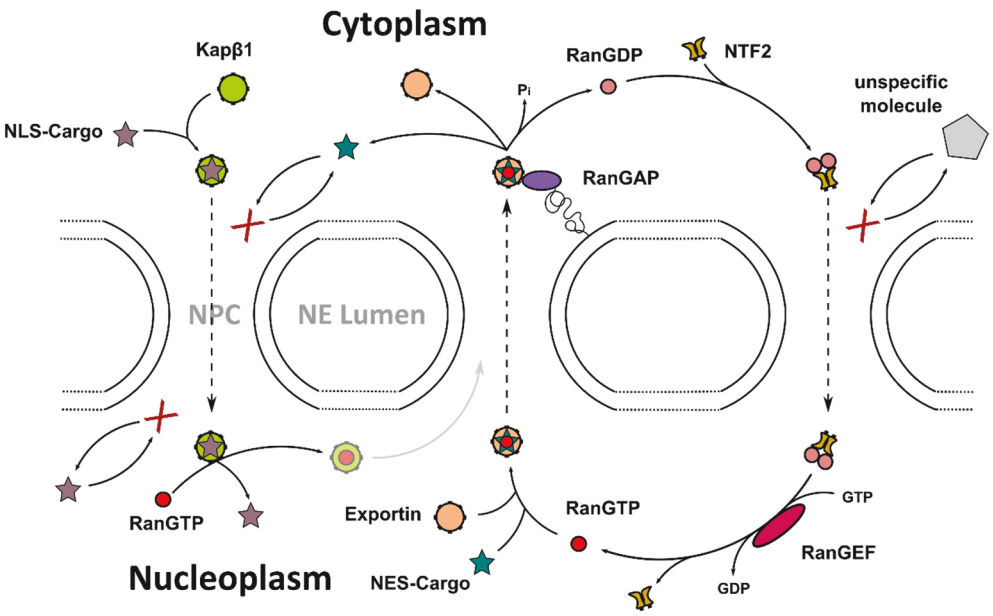

Figure 1-3 – The biochemistry of nucleocytoplasmic transport. NLS-cargos are ferried through NPCs by specialized Kaps (importins, e.g. Kapβ1) and released into the nucleoplasm upon interaction with RanGTP, which can shuttle back to the cytoplasm in complex with Kapβ1. In contrast, exportins require RanGTP to recognize NES-cargo. After translocation, the export-complex is dissociated via RanGAP-stimulated hydrolysis of RanGTP to RanGDP in the cytoplasm. RanGDP is imported back into the nucleus via NTF2, where it is recharged into RanGTP by chromatin-bound RanGEF. In the absence of Kaps, neither specific nor large nonspecific cargos can access the NPC. This figure was prepared for & reproduced from Fuxreiter *et al.* [27].

For import from the cytoplasm into the nucleus, transport receptors such as the classical import receptor Importinβ (also referred to as Importins, e.g. Impβ1 or Kapβ1), recognize their cargo by binding to short signaling peptides called nuclear localization signals (NLS) either directly or via small adaptor molecules (karyopherinα) [28]. Based on their binding affinity to the FG domains, multivalent Kaps overcome the selective barrier [29] and ferry their cargo through NPCs. Single-molecule-fluorescence studies revealed that Kap-cargo-complexes undergo a bidirectional random walk inside the central channel during translocation, which is indicative of Brownian motion that *per*

se neither imparts directionality nor consumes energy beyond k_BT [30], [31] (Figure 1-4).

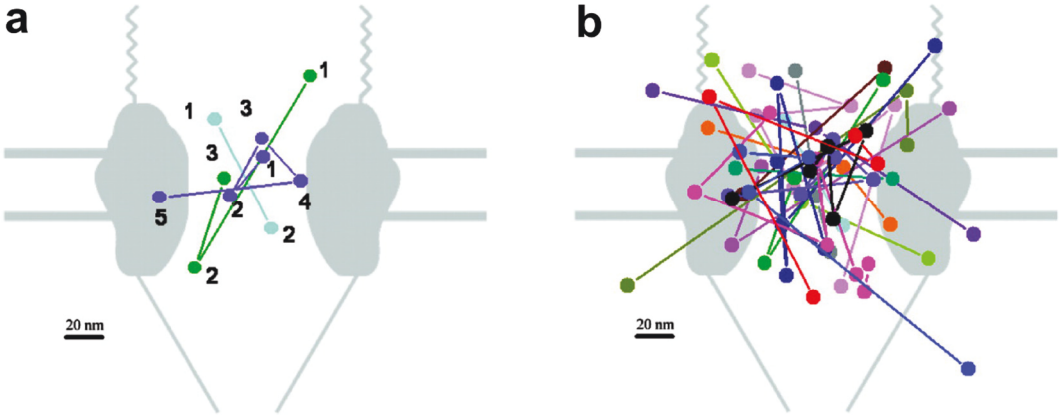

Figure 1-4 – Kap-cargo complexes perform a random walk inside the central channel of NPCs. **a**, Trajectories of three individual Kapβ1-specific import cargos (NLS-2xGFP) in transit through a NPC based on single molecule fluorescence microscopy in permeabilized HeLa cells. For each trajectory, the points are numbered in sequence. **b**, Superimposed plots of 17 trajectories (64 points) from 11 NPCs. Single molecule tracking reveals that transport complexes spend most of their transit time randomly moving in the central channel of the NPC with an average position that coincided with the midplane of the NE, indicative of undirected Brownian motion. Reproduced from Yang *et al.* [31].

On the trans side of the NPC, Kaps dissociate from their cargo upon interaction with RanGTP [32], a small guanosine triphosphate hydrolase (GTPase) of the Ras family. While the Kap-RanGTP complex can shuttle back to the cytoplasm [25], [33]–[37], the released cargo is free to diffuse in the nucleoplasm but cannot return to the cytoplasm on its own. Export into the cytoplasm is accomplished by designated export receptors (exportins), which bind to nuclear export signal sequences (NES [38]) that are displayed by their cargo. In contrast to NLS-recognition, exportins require association with RanGTP for efficient NES-binding [39]. The exportin-RanGTP-cargo-complex then shuttles through the NPCs central channel in a fashion similar to import, but is dissociated in the cytoplasm upon RanGTP hydrolysis to

RanGDP by the GTPase-activating protein RanGAP, which is located within the cytoplasmic filaments (Nup358 or RanBP2 in vertebrates, see Figure 1-2) [40]. Afterwards, RanGDP is shuttled back into the nucleus by its specific transport receptor NTF2 [41], [42], where it is recharged to RanGTP by the chromatin-bound guanine nucleotide exchange factors RanGEF (RCC1 in vertebrates) [43]. Transport directionality is accomplished by the asymmetric distribution of RanGAP and RanGEF, which maintain a steep concentration gradient of RanGTP that is ~200-1000 fold higher in the nucleus than in the cytoplasm [44], [45]. In this manner, nucleocytoplasmic transport (NCT) operates like a thermal ratchet, where the random motion of a particle (i.e. Kap or Kap-cargo-complex) is biased so that there is net movement in a particular direction [33]. The energetic toll to accumulate cargo against a concentration gradient is hence indirectly paid by GTP hydrolysis. Accordingly, an artificial inversion of the RanGTP gradient reversed transport directionality [46].

1.4.1 FG Nups are Intrinsically Disordered Proteins

The central transport channel of NPCs is filled with numerous copies of intrinsically disordered FG Nups. Together, they contribute about 3500 FG repeats per NPC [47] that serve as a selective binding platform for ~20 distinct transport receptors in humans (Table 1-1) [26]. Despite being redundant to a large extent, they were found to be vital for NPC barrier functionality and cell viability [48]. FG domains are generally classified according to their FG-repeat motifs, namely FG, FxFG or GLFG, as listened in Table 1-1 [47].

Table 1-1 – Copy number and number of FG repeats in mammalian FG Nucleoporins. If not stated otherwise, values are taken from Peleg *et al.* [47]. Copy number of all other Nups can be found in Cronshaw *et al.* [19]. Wherever multiple FG motifs are present, the most abundant is marked in bold.

FG domain Nup	FG domain copy number per NPC	# FG repeats per domain	Repeat motifs
Nup358/RanBP2	8	21	**FxFG**, **FG**
Nup214	8	46	FxFG, GFLG, **FG**
Pom121	8	22	FxFG, **FG**
Cg1/Nlp1	16	16	FG
Nup98	8	45	FxFG, GFLG, **FG**
Nup62	16 (128) [49]	17	**FxFG**, FG
Nup58/45	32-48	13	FxFG, GFLG, **FG**
Nup54	32-48 (64) [49]	12	FxFG, GFLG, **FG**
Nup35	16–32	4	FG
Nup153	8	39	**FxFG**, **FG**
Nup50	32	5	FG

Intrinsically disordered proteins (IDPs, also known as intrinsically unstructured proteins or natively unfolded proteins), represent a unique class of proteins. An estimated 10% of all proteins are fully disordered, whereas approximately 40% of eukaryotic proteins contain at least one long (>50 amino acids) disordered loop [50]. IDPs are involved in many important tasks such as signaling, control, or regulation of cellular function [3], [51] and display physiochemical characteristics reminiscent of random coils [52]. Compared to structured proteins, IDPs are considerably depleted in order-promoting amino acids (i.e. hydrophobic residues, ILVWYFCN), but enriched in disorder-

promoting amino acids (i.e. charged and polar residues, ARGQSEKP). The combination of low mean hydrophobicity (leading to low driving force for protein compaction) and high net charge (leading to strong electrostatic repulsion) represent further criteria for the absence of compact structure in IDPs [53]. Many IDPs are known to be promiscuous and as such involved in numerous interactions with multiple binding partners [53]. Hence, they often serve as nodes, or hubs, in protein interaction networks. Other hallmarks of IDPs include (i) fast binding kinetics (e.g. high dissociation rates), (ii) decoupled specificity and strength of binding (e.g. high specificity with low affinity) as well as (iii) one-to-many and many-to-one binding interactions, which underlies their promiscuous behavior [53]–[55].

These properties likely play an important role for NPC barrier functionality, as FG domain flexibility seems ideally suited to quickly alleviate any spatial constraints that arise during transport of large cargos. Additionally, they provide the promiscuity necessary to interact with several distinct Kaps. To harness these properties, not only IDPs in general, but specifically FG Nups have been recognized as nanomaterial building blocks *in vitro* [56], where they reconstitute the functional selectivity of NPCs when surface-tethered to biomimetic nanopores [57], [58], nanostructures [59], [60] and microbeads [52], [61], [62].

1.4.2 Karyopherins and Multivalent Binding

Karyopherins in humans share similar structure, molecular weights (90 - 150 kDa) and isoelectric points with pI values ranging between 4 and 5 [63]. Extensive studies on Kapβ1 identified ~10 binding pockets that recognize FG

repeats [64] and hence, multivalency is likely to play an important role in NCT.

In general, multivalent interactions are involved in many central processes of an organism, such as (i) recognition, (ii) regulation (iii) signaling and (iv) organization of cellular life. For example, multivalency plays a major role during leukocyte extravasation from the bloodstream (diapedesis) or for recognition, stable adhesion and subsequent uptake of bacteria and viruses by cells of the immune system [7], [65]. In this context, recognition is accomplished by multivalent interactions including antibodies and antigens or lectins and carbohydrates, e.g. through mannose-bindig lectins (MBL) in mammals or wheat germ agglutinin (WGA) in plants [3], [7], [66]. By binding to glycosylated Nucleoporins, WGA acts as a potent inhibitor of NCT [67], a process which is itself rich in multivalent interactions. Like IDPs, multivalency has been proposed "to be the rule, rather than the exception, in signaling biology" [68], [69]. Several subcellular bodies (e.g. Cajal bodies, P bodies and P granules) are enriched in multivalent proteins, which are thought to control their spatial organization [70].

Multivalent interactions are accomplished via several specialized binding pockets on receptor molecules that bind specifically to (often times repetitively) displayed regions on their target molecules (ligands). In contrast to weak monovalent binding, this offers the advantage of multiple and thus dramatically enhanced binding on a molecular scale, a concept also known in biochemistry as avidity [7]. Figure 1-5 and Figure 1-6 illustrate how these hallmark features manifest on the single protein level in the transport receptor Kapβ1.

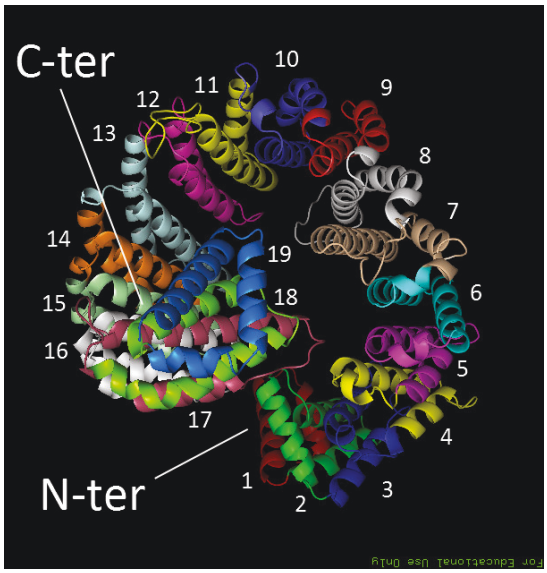

Figure 1-5 – Structure of Kapβ1. PDB 1QGK shows Kapβ1 in a "transport-competent state" bound to its binding domain on karyopherinα (excluded from the picture). HEAT repeats 1-19 of Kapβ1 are depicted according to Cingolani *et al.* [71]. The amino-terminus is facing the back of the image (dark red, HEAT-repeat 1) while the carboxy-terminus is facing the front (blue, HEAT-repeat 19). The structure has been displayed and arranged in PyMol.

Kapβ1 consists of 19 heat repeats, each comprised of 2 helices A and B (facing the outside or the inside of the molecule, respectively), which form a flexible alpha-solenoid fold as show in Figure 1-5 [71], [72]. FG-binding domains are distributed throughout the molecules solvent-exposed surface from the N-terminal HEAT repeat 3 to the C-terminal HEAT-repeat 17. Outlined in Figure 1-6 are binding sites verified experimentally and predicted by simulation (MD) or sequence alignment (conserved), respectively. Simulations predict that only few residues are necessary to form a FG repeat binding site (4 on average) [64].

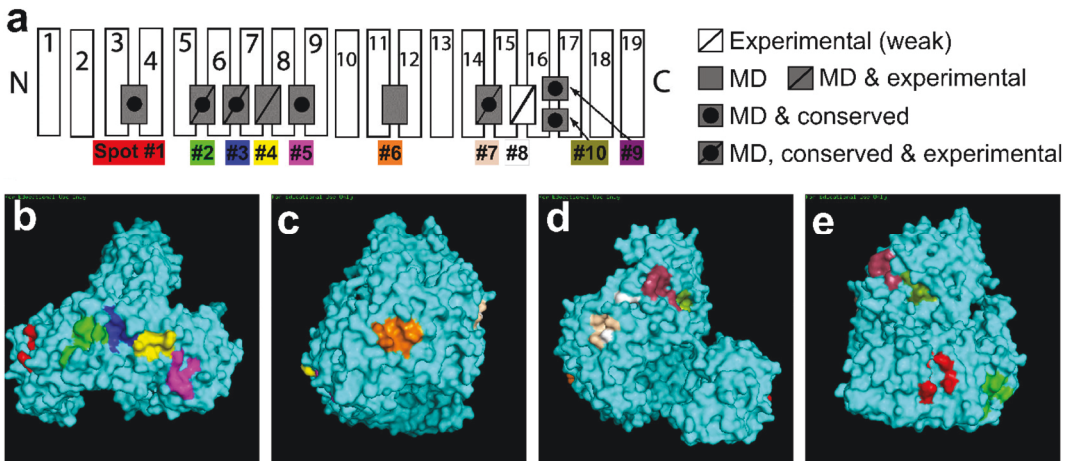

Figure 1-6 – Kapβ1 has multiple FG-binding sites. **a** Distribution of FG repeat binding pockets along HEAT-repeats 1-19 in Kapβ1 (cyan in **b**-**e**). All binding spots occur on hydrophobic patches of the Kapβ1 surface [64]. Binding spots identified by molecular dynamics simulations (MD) are labeled in gray, while experimentally known spots are labeled with a black slash. Conserved binding spots are labeled with a black dot. Each binding spot is labeled with a number and color and is shown in context of the whole molecule (PDB 1QGK) in **b** (spot 1-5), **c** (spot 6), **d** (spot 7-10) and **e** (spot 9, 10, 1, 2), respectively. The structure has been displayed and arranged in PyMol. Adapted from Isgro *et al.* [64].

As anticipated for multivalent interactions, dissociation constants between Kapβ1 and Nup153 have classically been reported to be very low (K_D~1-10 nM) [8], [9]. Mutations of binding pockets #2-4 significantly weakened the interaction (>5 fold), thus verifying the affinity-enhancing effect of multivalency [8].

In addition to enhanced affinity, more recently reported effects in multivalent systems include superselectivity [73], [74], “hopping” and “sliding” (i.e. lateral diffusion without complete dissociation) of multivalent receptors across (multivalent) ligand surfaces or polymers [75]–[77].

1.4.3 Transport Models

Despite the high FG repeat density inside the pore that follows from the abundance of FG domains in the NPC (estimated to be on the order of 10

mM [78]), transport through the pore allows for a molecular flux of up to 20 $MDa \cdot NPC^{-1} \cdot s^{-1}$ that consist of ~100-500 parallel translocation events [11], [15], [16]. How such high transport rates are accomplished remains a central question in the field. The challenge lies in understanding how precisely FG Nup architecture correlates with function and is, to date, still not very well known. Although their position within the NPC has been determined by immuno-electron [25], [79], [80] and fluorescence microscopy [81], [82], a structural determination of FG domain-conformation inside the NPC remains elusive. This is most likely due to their low electron density and high flexibility that is typical for IDPs [83]. Thus, in order to explain how NPC barrier functionality is derived from their collective morphological features, much work resorted to FG domain characterization *in vitro*. Based on these efforts, several models have been proposed to explain NCT.

1.4.3.1 The selective phase model

Based on the hypothesis that FG domains assemble into a "selective phase" conveyed by a meshwork of hydrophobic inter-FG-repeat-interactions within the NPC [15], work by Frey *et al.* demonstrated that highly concentrated FG domains (~1-100 mM) form hydrogels up to a few millimeters in size when exposed to non-physiological conditions [84]–[86] (Figure 1-7). Interference with hydrophobic interactions using cyclohexane-1,2-diol has been shown to reversibly disruption the NPCs permeability barrier in cells [87]. Accordingly, FG hydrogels were dissolved by chaotropic agents such as 6 M guanidinium chloride [84].

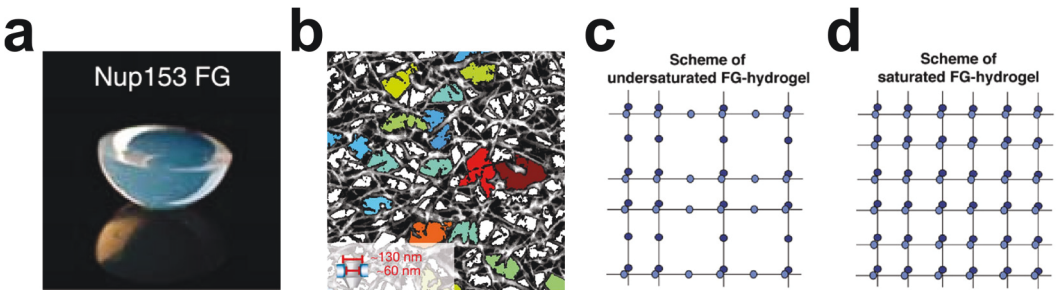

Figure 1-7 – The hydrogel model. **a**, Macroscopic hydrogels form at high FG domain concentration (200mg/ml or ~1-100 mM) under non-physiological conditions [84]–[86], [88]. **b,** Studies on the composition of the FG domain-hydrogels showed that they consist of amyloid fibers [86]. Interlacing amyloid fibers give rise to aqueous pores with diameters between 50-150 nm (see inset). **c, d**, Undersaturated and saturated hydrogel, where every FG repeat (blue) interacts with its next neighbor. The hydrogel model propose that the FG domains crosslink to form a highly organized three-dimensional network within the NPC. **A,** Reproduced from Labokha *et al.* [88]. **b**, Reproduced from Milles *et al.* [86]. **c, d,** Reproduced from Frey *et al.* [89].

By binding to FG repeats, multivalent Kaps are hypothesized to partition into the gel phase. Transient interactions of Kaps with FG domains are thought to open the FG-FG bonds [84] and thereby "dissolve" into the meshwork, which otherwise poses a physical barrier that blocks entry of unspecific molecules [15]. The size of the meshwork sets the size limit for small molecules to passively traverse the barrier. Spectroscopic measurements [90], [91] and electron microscopy [86] revealed that the backbone structure of the hydrogel is composed of interlacing amyloid fibrils that give rise to aqueous pores, which are randomly distributed throughout the gel (Figure 1-7b). Pore sizes in the fibrous meshwork range from 50-150 nm and are inversely correlated to the FG domain concentration used during gel formation [86] (Figure 1-7b inset). Under saturating conditions (Figure 1-7d), hydrogels reproduce the permeability properties of the NPC and allow for the facilitated translocation of Kap-cargo complexes while hindering the traversal of non-specific molecules [89]. Intra-gel diffusion coefficients obtained for large cargos

are in a similar range as those measured for diffusion of mRNPs inside the central channel of NPCs (~0.06 um^2/s) [11], [92]. In agreement with the observation of enhanced Kap accumulation in the nucleus of cells compared to passively diffusing molecules of the same size [15], [18], hydrogels showed an increased uptake of Kaps compared to same sized passive molecules [89]. Pre-incubation with Kaps after gel formation resulted in more efficient rejection of non-specific molecules, but also hampered the diffusion of Kap-cargo complexes[85]. This is opposed to observations in cells, where rising Kap concentration leads to reduced NPC-interaction time [30]. Inside a hydrogel-containing NPC, Kap-cargo complexes as well as small passively diffusing molecules are assumed to move randomly with overlapping spatial routs [15]. In contrast, data obtained by single particle fluorescence microscopy *in vivo*[93] and post-embedding immunogold electron-microscopy of high-pressure frozen yeast cells[94] revealed that receptor-mediated and passive diffusion take distinct spatial routs during translocation.

Although reproducing NPC selectivity on a macroscopic scale, it remains less clear whether such gels retain their functional properties on a nanoscopic scale relevant for NCT. Transport assays presented in Frey *et al.* reported that ~ 15 % of unspecific cargo penetrates into the gel for several tens of micrometers [85]. Due to the combined localization uncertainty of the fluorescent cargo and the gel boundary of ~500 nm, however, the percentage of unspecific molecules penetrating the first several 100 nm of the gel can be much higher. Notably, non-specific penetration was reduced when the gel was preincubated with Kaps after formation [85]. Due to the macroscopic nature of the gel-assays based on fluorescent molecules, their functionality remains unclear in context of NCT, as the NPCs central channel spans only ~100 nm, a length scale not accessible to the assay. Nonetheless, the concept of phase separation

based on repetitively displayed ligands and multivalent binding partners has been noticed as a general organization principle for several sub-cellular structures [70]. In contrast to the selective phase, multivalent proteins are generally thought to initiate and stabilize the sol-gel transition in these self-assembly-processes [70] rather than to dissolve through the network itself [84]–[86], [89]. Accordingly, FG domain hydrogels were unable to assemble in the presence of Kaps [86]. Experiments *in vitro* and *in vivo* by Patel *et al.* demonstrated that the same FG domain successfully used for gelation assays [84], [85] did neither interact with itself nor with other FG domains under physiological conditions. The authors concluded that due to the non-physiological conditions necessary for gel formation, it is unlikely that the NPC barrier in a living organism is exclusively composed of a FG domain-hydrogel [61].

1.4.3.2 The virtual gating model

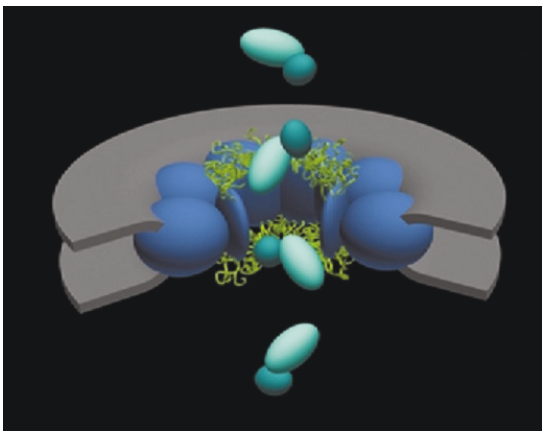

Figure 1-8 - The virtual gating model. The model suggest that stochastic movements of the FG domain (green) at the pore peripheries act as an entropic barrier against inert cargo. This energetic barrier is overcome by Kaps (dark turquoise) interacting with FG domains to ferry cargos (light turquoise) across the NPC (blue). Reproduced from Rout *et al.* [95].

In comparison to phase transition based on free FG domains from solution, FG Nups within the NPC ex- and interior are end-tethered to the pore walls [80]. According to the "virtual gating" or "Brownian affinity gating" model by Rout *et al.* [80], [95] (Figure 1-8), entering the NPCs narrow central channel is coupled to a large loss in a molecules entropy. Since the entropic cost rises with the molecules size, a narrow pore represents a quasi-impenetrable barrier for large cargos. Densely packed FG Nups add to the entropic cost, since they occupy additional space inside and around the pore. Based on their thermal motion, FG Nups bristling out of the NPC further exclude non-specific molecules at the pore periphery from entering the central channel. They are therefore not assumed to adopt an ordered structural conformation, but rather repel themselves and other molecules. Kaps overcome the entropic barrier via FG repeat binding [80], [95]. The energetic gain from Kap-FG interaction, e.g. in terms of Gibbs free energy, serves as an "activation energy" to overcome the entropic cost of entering the pore and allows Kap-cargo access to the NPC interior. This rationalizes the observation that nuclear accumulation of transport receptors is orders magnitude faster than that of passively traversing molecules of the same size [15], [18]. To efficiently translocate through the complete central channel, the virtual gating model assumes that sufficient Kap-FG affinity to overcome the entropic barrier is combined with high kinetic off-rates that allow Kaps to traverse the NPC in a fast manner [95]. This can be achieved via many low-affinity binding sites in the multivalent Kap molecule [64], [95]. As the NPC is presumably filled with FG repeats, Kaps can bind to several different FG Nups at the same time and travel in this manner from one FG Nup to the next. Therefore, it is binding avidity, rather than affinity, which promotes transport in the virtual gating model (see subsection 1.4.2). To achieve transport rates in the

ms range as observed *in vivo* [11], the model assumes diffusion limited on-rates of approximately $7x10^9\,M^{-1}s^{-1}$ [95], [96]. Considering previously measured on-rates of protein-IDP interactions [97] and the high cellular viscosity [93], [98], the assumed on-rate seems unlikely high.

1.4.3.3 The polymer brush model

Based on their end-on attachment at the peripheries of the NPC[80], the polymer brush model emanates from the notion that close proximity between FG Nup anchoring sites causes the FG domains to extend away from the NPC, resembling a polymer brush. By definition, a brush is formed by a monolayer of polymers that are closely grafted on one end to a surface while their other end is free to explore the solvent [99]. In that manner, polymer brush formation is a conformational response to an underlying two-dimensional interface (Figure 1-9) [60], [99].

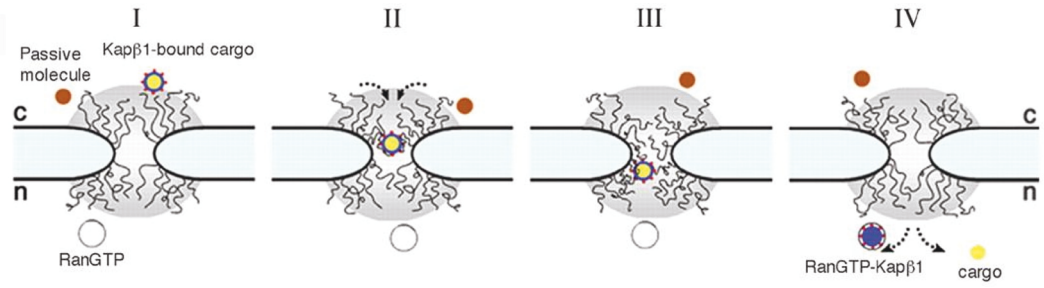

Figure 1-9 – The polymer brush model. I: The FG domains form an entropic barrier surrounding the NPC in the absence of Kapβ1-FG binding interactions. The range of the barrier and the stochastic fluctuations of the FG domains are highlighted by the gray area. II: Kap-FG binding causes a local collapse of the involved FG domains towards their anchoring site, which draws Kap-cargo complexes into the pore. III: Kap-cargo complexes translocate to the nuclear periphery via a continuous binding-collapsing and unbinding-distending processes. IV: In the nucleus, RanGTP dissociates the cargo and stays complexed with Kap, which prevents further Kap-FG interactions. The entropic barrier is maintained by non-Kap-bound FG domains, which exclude passive molecules in the vicinity of the NPC.

The cytoplasmic filaments and the nuclear basket have been omitted to emphasize the generality of selective gating. Reproduced from Lim *et al.*[60].

In subsequent studies on nanostructures, Lim *et al.* showed that end-grafted FG domains displayed compression characteristics resembling those of molecular brushes, but not hydrogels [60]. Like its disrupting effect on the NPC barrier in cells, addition of hexanediol led to the collapse of the brushes that was fully reversible after hexanediol was removed [60].

Such FG domain brushes retained their affinity to Kaps and underwent a disorder-to-order transition upon Kap-binding, which collapsed the FG domains towards their base [59], [60]. Consecutive Kap unbinding reversed the collapse and reestablished the entropic barrier. Following this concept, the model proposes that extended FG domains form a corona-like entropic barrier on both ends of the NPC that repels non-specific molecules from entering the central channel due to their stochastic fluctuations. Access is only granted to Kaps, which overcome the barrier locally and are drawn into the pore as the FG domains collapse towards their anchoring sites. Kaps (and Kap-cargo complexes) are then thought to randomly move from one FG domain to the next, where each binding event is accompanied by another local collapse. In turn, each unbinding event results in their re-extension and therefore the restoration of the barrier. This collapsing and distending of FG domain is likely orders of magnitude faster than the millisecond transport rates in NCT, as the relaxation time of a random peptide coil is on the order of microseconds [100]. This allows for simultaneous Kap translocation while maintaining barrier integrity towards non-specific molecules [60]. During their translocation, Kaps face the same kinetic limitations as discussed for the virtual gating model.

As a consequence of the polymer brush model, Kaps localize frequently towards the wall of the central channel, which is consistent with observations in cells [93]. As several FG Nups were shown to exhibit cohesive properties which can interfere with brush formation [52], collapsing and distending may not represent a uniform mechanism throughout the pore. Furthermore, the experimentally observed FG domain collapse was induced at low, non-physiological Kap concentrations in the nanomolar range [60]. Successive analysis of Kap binding to planar molecular brushes revealed that the collapse at low concentrations is rectified at increasing Kap concentrations [101]. It was shown that FG domains extend even further upon incorporating large amounts of Kap molecules at physiological concentrations [102]–[104]. This emphasizes the sensitivity of end-tethered FG domain conformation in response to Kap binding. It is therefore likely that structural changes induced by Kap-FG interactions play an important role in the NPCs barrier functionality.

1.4.3.4 The forest/two-gate model

Work by Patel *et al.* and Yamada *et al.* revealed that FG domains can be classified into separate categories [52], [61]. FG domains with low charge content adopt a globular collapsed coil conformation (i.e. cohesive “shrubs”), while others are highly charged and adopt a dynamic, non-cohesive extended coil conformation. FG domains featuring both characteristics represent a third class termed “trees”. Based on this bimodal distribution of FG domain categories, the “forest” model (Figure 1-10) suggests a topology of FG domains in the NPC which leads to two distinct transport zones that differ in their physiochemical properties [52]. In the central channel, sticky globular

conformations located at the tip of FG Nups cohere into a gel-like state (zone 1). These globular FG Nups are connected to the NPC scaffold via non-cohesive FG domains in a relaxed or extended conformation reminiscent of a molecular brush (zone 2). A similar architecture was obtain using simulations of an NPC exclusively filled with "trees", albeit only under the assumption that tethering effects are minimal in the central channel of the pore [105].

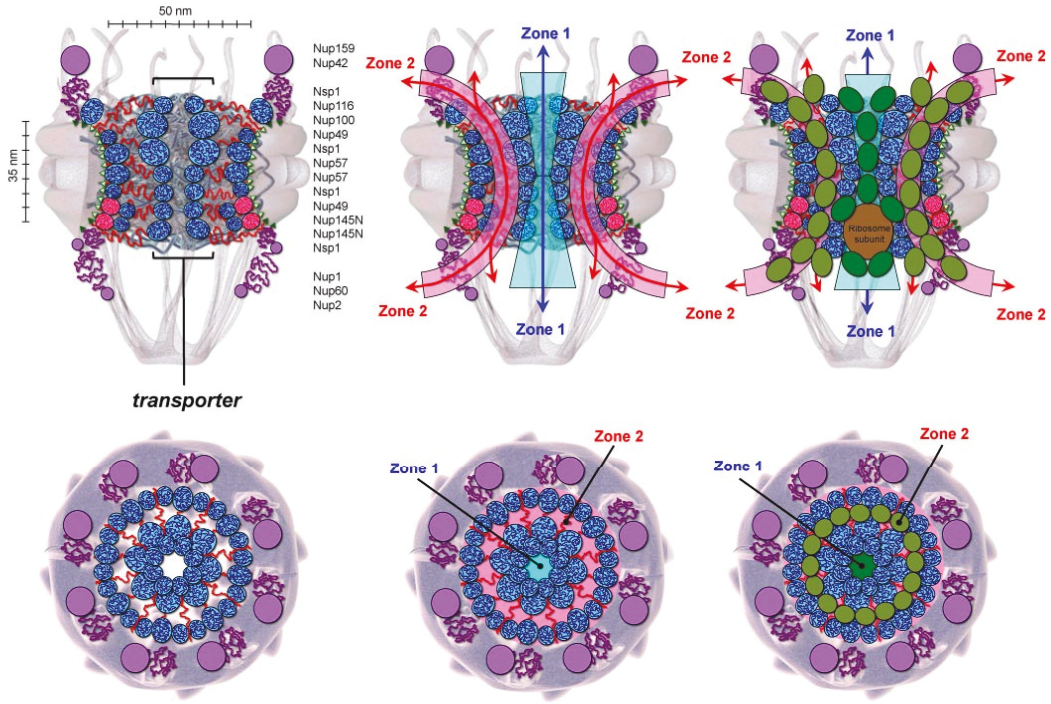

Figure 1-10 – The forest/two-gate model. The model is based on characteristics of yeast FG Nups. FG domains with cohesive properties (blue) that are oriented towards the central channel form zone 1 (transporter), whereas more extended non-cohesive (red) FG domains closer to the channel wall form zone 2. Kaps in transit are depicted in dark green (zone 1) or light green (zone 2). See text for details. Reproduced from Yamada *et al.*[52].

In the forest model, zone 2 allows for the translocation of Kaps alone or Kaps loaded with small cargos. Depending on spatial demand and Kap interaction, the relaxed FG domains in zone 2 can respond with contraction or expansion

[60], [104]. This flexibility allows Kaps carrying large cargos, e.g. ribosomal subunits and mRNA, to pass through zone 1. Both zones permit the passive diffusion of small molecules. Finally, the entrances to zone 2 are flanked by non-cohesive, extended coil FG domains that can function as entropic bristles as proposed by the virtual gate and polymer brush model. Post-embedding immunogold electron-microscopy agreed to a large extent with the proposed spatial zones, where Kaps were observed at the NPC periphery, while small GFP molecules were distributed evenly throughout the pore. Moreover, transport receptors involved in mRNP export located to the central channel[94]. These results are opposed by findings obtained from single molecule trajectories in functional NPCs, which showed that small passively diffusing molecules localize preferentially to the central channel [93].

1.4.3.5 The reduction of dimensionality model

Reduction of dimensionality (ROD) was originally proposed in 1968 by Adam and Delbrück [1] as a means to enhance the rate of diffusion-limited protein-protein association in biological systems [106]. Inside a cell, the time necessary for a diffusing molecule to localize its binding partner is strongly dependent on their size in relation to the space the search process has to cover during a three-dimensional random walk. This time reduces significantly when the search is confined to one or two dimensions. Thus, rather than increasing protein concentrations to maintain sufficient reaction rates, one binding partner can be confined to a much larger structure of lower dimensionality. The initial search for said structure would then occur in three dimensions, while the consecutive search for the target takes place in two or one, thereby increasing the overall association rate. Berg and Von Hippel [106] note that

efficient one- or two-dimensional diffusion requires a high affinity towards the lower dimensionality structure, but must further be effectively delocalized (i.e. evenly distributed over a molecules surface) so that diffusion along the guiding structure is not severely impeded. This is realized in multivalent molecules, where individual low affinity binding pockets are defined by high off-rates that collectively contribute to an overall high binding affinity (see subsection 1.4.2). Then the ligands search along the diffusional guide is characterized by many transient low affinity interactions that are interrupted with events of complete unbinding, which can carry the molecule to other regions of the surface. In this manner, three dimensional diffusion is coupled to one- or two dimensional diffusion in the overall reaction. Such delocalized non-specific affinity has been reported for the one-dimensional diffusion of the *E. coli lac* repressor along DNA[107], whose association is entirely electrostatic in nature[108], [109]. Similar to electrostatic interactions, Berg and Von Hippel envisioned facilitated one- or two dimensional diffusion of a protein along a hydrophobic surface interacting with hydrophobic patches on the molecules exterior. As a case in point, studies on synthetic and biological systems have shown that surface bound molecules experience ROD during their diffusion [76], [107], [110].

Based on this framework, Peters *et al.* proposed ROD as the mechanism underlying nucleocytoplasmic transport of Kaps through NPCs (Figure 1-11)[2], [78], [111]. Extending on the notion that the intrinsically disordered FG domain conformation is highly sensitive to ligand binding[60], the ROD model suggests that all FG domains are permanently collapsed *in vivo*. As the intracellular concentration of transport receptors by far exceeds the number of NPCs, it is likely that all FG repeats are saturated at steady state[78], [103]. Inside the central channel, the continuously collapsed FG domains

represent a uniform, FG repeat-rich layer along the pore wall reminiscent of the “hydrophobic surface” envisioned by Berg and Von Hippel.

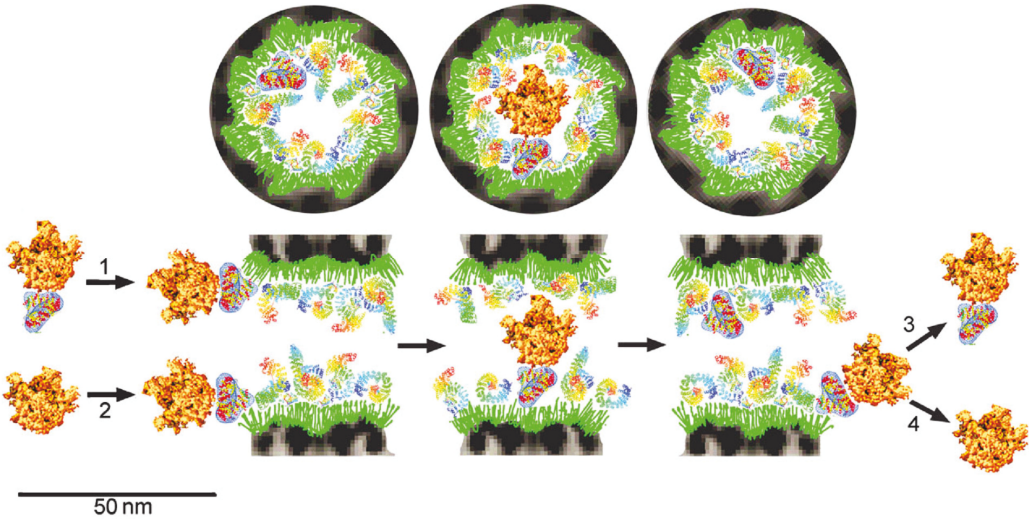

Figure 1-11 – The ROD model. Kap-cargo-complexes form in the cytoplasm (1) or directly at the NPC (2) and diffuse in two dimensions along the pore wall on the hydrophobic surface provide by the FG domains. After Kap-cargo translocation through the central channel, cargo is released with (3) or without (4) Kap-FG dissociation. At steady state, many distinct Kaps populate the pore, leaving a free central channel for passive diffusion. Reproduced from Peters *et al.*[78].

In continuation of this analogy, Kaps are hypothesized to bind to this layer due to their FG domain affinity, but retain a substantial degree of lateral mobility owing to their ~10 delocalized hydrophobic binding pockets[64] (see subsection 1.4.2 and Figure 1-6). Upon binding, Kap-cargo complexes diffusive randomly along the channel walls in two dimensions. Despite the possibility that surface and bulk diffusion might be coupled under such circumstances[76], [112], the cylindrical shape of the NPCs central channel would drastically enhance the re-capture rate of a Kap in case of unbinding. As a consequence to ROD, transport times are significantly shortened due to the confinement to two dimension instead of three, therefore reducing the duration of the diffusional search process for the pore exit[1]. In this manner,

ROD poses an explanation to the counterintuitive observation that nuclear accumulation of FG binding Kaps is 10-100 times faster than the one of passively diffusing molecules similar in size [15], [18]. In contrast to other models discussed so far, FG Nups are not directly involved in the ROD models gating mechanism. Barrier functionality is achieved by FG domain-bound Kaps that exclude non-specific molecules from entering the pore by preoccupying the central channel. Interestingly, this Kap-enhanced barrier functionality has been observed on FG domain-functionalized artificial nanopores *in vitro*[58]. In agreement with observations based on single molecule tracking experiments[93], the ROD model predicts that Kap-facilitated translocation occurs along the channel wall, while passive molecules diffuse through center of the pore.

Despite experimental evidence for ROD in artificial and biological systems other than the NPC, no study has been able to clarify the role of reduction of dimensionality during NCT *in vivo*. Towards this end, the work presented in chapter 5 represents the first experimental evidence to demonstrate the physical relevance of ROD in the context of Kaps and FG domains in an artificial environment.

1.4.3.6 Kap-centric barrier mechanism

The thus far discussed models focus mainly on the FG domains as barrier constituents, but discuss to a less extent how Kap-FG interaction influences NPC barrier shape, dynamics and functionality.

To resolve how mechanistic barrier control is balanced with Kap-FG binding kinetics, Lim and coworkers deployed a novel method based on surface plasmon resonance (SPR). This method allows direct correlation of

conformational changes in surface-tethered FG domains upon multivalent Kapβ1–FG interactions [102], [104]. Experiments revealed that FG domain conformation is sensitive to grafting distance and forms molecular brush layers. Layers-heights were found to decrease when adding low concentrations of Kaps, but underwent a self-healing re-extension and swelling beyond their initial height as Kap concentrations approached physiological levels [102], [104]. Interestingly, this effect has been predicted in computational models[113], [114]. While initial affinities at low Kap concentrations to pristine FG domain layers are strong (K_D~100 nM), the incorporation of Kaps into the layer at rising concentrations is accompanied by the emergence of weakly bound Kap species (K_D~10 µM). This reduced affinity showed elevated kinetic on and off-rates by 4-5 orders of magnitude [104].

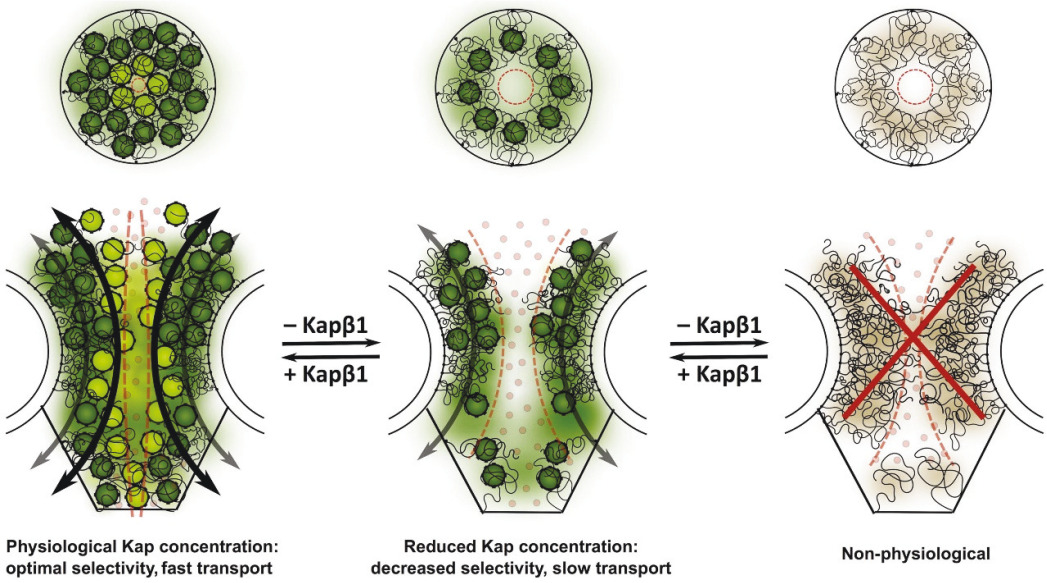

Figure 1-12 – The Kap-centric barrier mechanism. Karyopherins form an essential component of the NPCs barrier functionality. *Left:* At physiological concentrations, strongly bound Kaps (dark green) cause the FG domains to swell, effectively reducing the width of the central channel. While this narrowing enhances NPC selectivity, competition for space and limited FG domains results in transiently bound Kap-species (light green) that traverse the barrier more rapidly. *Middle:* Kap

reduction results in an apparent contraction of the barrier, rendering the NPC more penetrable to passive and unspecific molecules (i.e. "leaky"). Without competing Kaps, individual transport receptors are "trapped" by the FG domains and transport is slowed down until enough Kaps accumulate to reestablish steady state. *Right:* An NPC devoid of any transport receptors is expected to be a non-physiological scenario. Figure reproduced from Kapinos *et al.*[104].

Based on their high cellular concentration and FG domain-affinity, it is likely for NPCs to be filled with Kaps at steady-state[78], [115]. In contrast to the frequently depicted "empty pore" [11], [60], [89], ~100 Kaps [103], [116] were observed to reside within a single NPC. Single molecule fluorescence studies revealed enriched Kap-populations along the channel walls, while passively diffusing cargo localized to the central channel [93], [117]. Thus, at physiological concentrations, tightly bound Kaps likely form an integral component of the NPC barrier [101], [104] (Figure 1-12, left). Kap-dependent inhibition of nonspecific transport has been observed in FG domain-functionalized nanopores [58]. Depending on the inter-Kap-competition for limited FG repeats inside NPCs at rising Kap concentrations, numerous distinct transport rates exist. This poses an explanation to *in vivo* observations of translocation times that shorten with increasing Kap concentration [30]. Further, translocation is only efficient at sufficiently high amounts of Kapβ1 (> 1.5 µM) [30]. In this model, the reduction of Kaps rather than FG domains would lead to loss of NPC barrier functionality. This serves as possible explanation to the observation that NPC functionality is robust even to substantial deletion of FG domains [48], [118].

The NPC selective barrier is thought of as a combined effect of FG Nups and Kaps, in which Kap-FG domain binding causes the barrier to swell or contract depending on Kap-binding, occupancy and cargo size [119]. Besides enhancing barrier functionality, competing Kaps can at the same time display increased

diffusivity as their affinity decreases while competing for FG repeats at high Kap occupancy. Such delocalized affinity of multivalent receptors was envisioned previously by the ROD model, but has thus far not been verified experimentally. As a case in point, the results presented in chapter 5 of this thesis show evidence that the effect invoked by the Kap-centric model, i.e. enhanced diffusivity on top of a FG domain layer, is what drives fast diffusion at high Kap concentrations *in vitro*.

1.5 Ambiguities

Thus far, no comprehensive experimental evidence is available to clearly verify these or other proposed models (e.g. the "oily spaghetti model"[96]) in living cells. This is, to a large extent, due to the technical difficulties associated with the length- and timescale of NCT. Other problems include uncertainties such as the notion that the FG Nups still elude structural/conformational determination inside the NPC. Further difficulties involve the following:

(1) Given their high cellular abundance and FG domain affinity, it seems certain that Kap occupancy must be taken into account for barrier-functionality and transport studies, which is not the case in several models proposed (i.e. gel, brush, virtual gate).

(2) Short ms-dwell-times imply low affinity binding constants which allow for transient complexes. This is at odds with the fact that insufficient binding leads to NPC rejection[29], [120].

(3) Sufficient Kap-FG domain affinity is required for selective & facilitated transport. How this is balanced with the necessary receptor mobility for rapid translocation is still not well understood.

(4) Several models propose a delocalized affinity that leads to facilitated surface diffusion, which has not been shown in context of FG domains and Kaps.

1.6 Aim of the Thesis

The objective of this thesis was to reconcile the apparent paradox of high Kap-FG affinities measured *in vitro* and rapid transport rates *in vivo* and further to understand how the tradeoff between mobility and selectivity is achieved by Kapβ1. I experimentally address the proposed surface diffusion as means to expedited Kap-facilitated cargo translocation on a layer of FG domains, i.e. two-dimensional diffusion. To explore said effects, I employed photonic force microscopy to study the interaction and motion of Kap-functionalized colloidal probes diffusing on an FG domain-presenting surface. Results are obtained from the single colloid perspective as well as on the ensemble level. I purified and characterized Kapβ1 and the FG domain of Nup153. In addition, the surface chemistry for their attachment to colloids and surfaces was established. The obtained observations demonstrate that biochemical Kap-FG interactions *per se* severely impede mobility on a FG domain layer. However, elevated Kap-occupancy in the layer at rising Kap levels in solution lead to a gradual increase in mobility due to weakened probe-surface interactions. Ensemble level analysis at high Kap concentrations revealed probe diffusion in two dimensions on top of the layer. These novel

observations complement current understanding of nucleocytoplasmic transport, while at the same time providing insight into selective, two-dimensional surface transport in an artificial context.

Chapter 2

2 Cloning, expression and characterization of cNup153 & Kapβ1

Studies using immuno-EM revealed that Nup153 is located at the nuclear side of the NPC, where it is anchored to the distal ring and nuclear basket by its amino-terminus and zinc finger motif, respectively. The flexible FG domain of Nup153 is located between the zinc finger motif and its carboxy-terminus, which is not restricted to one particular subdomain of the NPC but can protrude to the cytoplasmic face of the pore (Figure 2-1) [121].

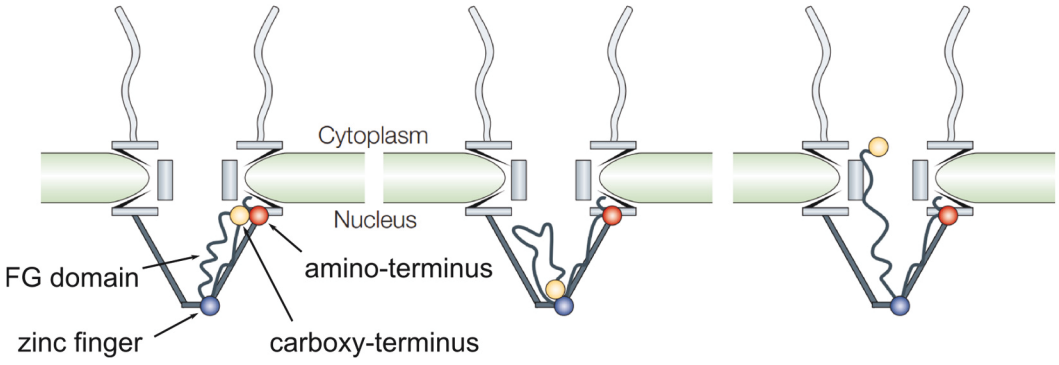

Figure 2-1 – Nup153 domain topography in the NPC. Adapted from Fahrenkrog *et al.* [25]

Single molecule studies using atomic force microscopy (AFM) by Lim *et al.* [122] revealed that the FG domain of Nup153 is highly flexible and can be reversibly stretched and relaxed without any change to its intrinsic elasticity, indicating a lack of intra-FG interactions. As a consequence, surface-tethered Nup153 FG domains were observed to form extensible brush-like layers [59], [60], [104]. In addition, Lim *et al.* revealed complex binding topologies during

the interaction between the FG domain of Nup153 and Kapβ1, which is indicative of promiscuous interactions [122]. Binding of Kapβ1 to the FG domain of Nup153 has been studied in several assays with binding affinities in the low nM range [8], [9]. Kapβ1 itself has been studied intensively in the past, and ~10 FG repeat binding sites have been identified on the solvent exposed surface of the molecule (see Figure 1-6) [64]. In a synthetic context, Kapβ1 was shown to selectively translocate through nanopores functionalized with Nup153 FG domains, while transport of non-specific molecules was hindered [57]. This shows that both proteins alone reconstitute functional properties of NCT in an artificial context.

Since both proteins have been well characterized and were shown to retain their functionality in a biomimetic context, I used them in my experiments as representatives for Kap-FG domain interactions.

2.1 Cloning and expression

In the following, I describe how I expressed and purified both proteins. The 602 amino acid (aa) C-terminal FG repeat domain of human Nup153 (aa 874-1475, cNup153) was cloned, expressed and purified as described [57]. This construct contains an N-terminal His_6-tag followed by 36 residues of a short laminin linker and a TEV protease cleavage site. Three cysteines where added to the N-terminus to allow attachment of the recombinant cNup153 fragment to maleimide-functionalized glass surfaces. The cNup153 fragment used in this thesis is identical to the cNup153 used in the aforementioned studies by Lim *et al.*[59], [60]. cNup153 was expressed at 37 °C for 5 hours in E. coli BL21 (DE3) competent cells (Novagen). The expressed protein was purified under denaturing conditions (8 M urea, 100 mM Na_2HPO_4, 10 mM DTT, and 10

mM Tris-HCl, pH 8.5) using a Ni-NTA column. TEV protease was used to remove the His_6-tag from cNup153 (Figure 2-2). The His_6-tag-free protein fragments were then eluted with a buffer containing 8 M urea, 100 mM Na_2HPO_4, 10 mM DTT, and 10 mM Tris-HCl, pH 8.5. To ensure that (i) the pHis antibody had no unspecific affinity towards cNup153 and (ii) all uncleaved His_6-cNup153 was removed after TEV protease treatment, I analyzed fractions of cNup153 on SDS page using coomassie staining and western blotting, respectively. His_6-cNup153 was cleaved using TEV protease (lane 1 in Figure 2-2) and the fraction was subjected to western blotting using pHis-antibody, which exclusively reacted with the uncleaved His6-cNup153 species (i.e., the His_6-tag). Subsequent purification on a Ni-NTA column resulted in complete separation of uncleaved His_6-cNup153 (lane 2).

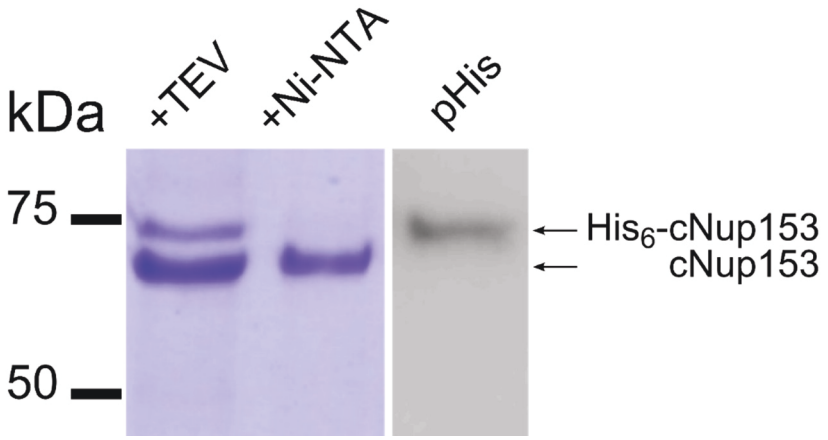

Figure 2-2 – Removal of the His_6-tag from cNup153. Coomassie staining (12 % PAGE with 0.1% SDS) reveals that cNup153 is separated from the His_6-tag by TEV cleavage (lane 1) followed by a Ni-NTA column (lane 2). The fraction from lane 1 was analyzed by western blotting using the pHis antibody, which was solely bound to uncleaved His_6-cNup153 demonstrating its exclusive specificity towards the His_6-tag.

Full-length human Kapβ1 was amplified by PCR and inserted into an *Nco*I–*Bam*HI digested pETM-11 expression vector (EMBL Protein Expression and Purification Facility). N-terminal His_6-tagged Kapβ1 was expressed in E. coli

BL21 (DE3) cells at 25 °C overnight and purified on a Ni-NTA column (10 mM TrisHCl, pH 8, 100 mM NaCl, 1mM DTT; eluted with 30–80 mM imidazole) followed by gel-filtration using Superdex 200 column (Figure 2-3).

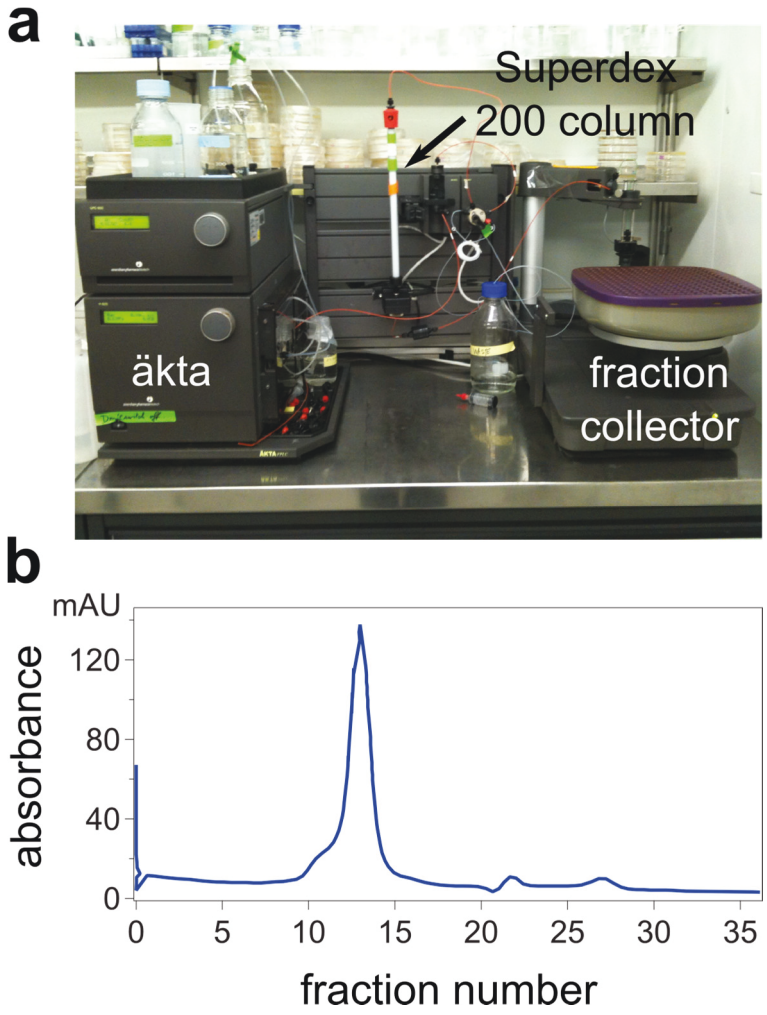

Figure 2-3 – Gel filtration of Kapβ1. **a,** gel-filtration was performed using a Superdex 200 column in an ÄKTA Purifier 100/10 system (Both GE Healthcare). **b**, elution profile obtained for Kapβ1 after two rounds of size exclusion. The peak shows that most of the protein is contained in a single fraction.

Purified proteins were pooled, analyzed by SDS–PAGE (Figure 2-4) and aliquots stored at -80°C.

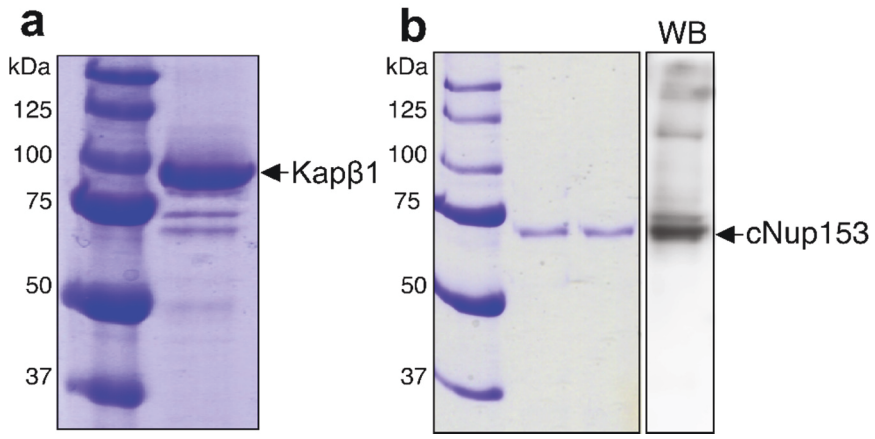

Figure 2-4 – Protein purity. Quality of Kapβ1 (**a**) and cNup153 (**b**) as analyzed by 12% PAGE (with 0.1 % SDS). cNup153 was identified by western blotting using α-Nup153 antibody (WB).

2.2 Sequence analysis of cNup153

After purification, I analyzed the proteins to characterize their properties and interaction behavior *in vitro*.

Sequence analysis of cNup153 revealed that it is characterized by a total of 63.5% disorder-promoting amino acids, a low hydrophobicity with a GRAVY (Grand average of hydropathicity [123]) index of -0.44 and highly charged regions (Figure 2-5). In addition, cNup153 contains several "non-cohesive" FG-repeat motifs (i.e. FxFG), but no cohesive motifs (i.e. GLFG) [61], [124]. PONDR [125], a web-based tool that localizes disordered (values > 0.5) and ordered structures (values < 0.5) in proteins, predicts cNup153 to be almost exclusively disorder (solid red line in Figure 2-5). Further predictions based on molecular mass (61 kDa Figure 2-2) and known stokes diameter [126] (11.3 nm [57]) as well as *in vivo* studies [124] show that cNup153 is likely to adopt an overall relaxed coil conformation with non-cohesive properties. Overall, cNup153 shows all characteristics of an IDP.

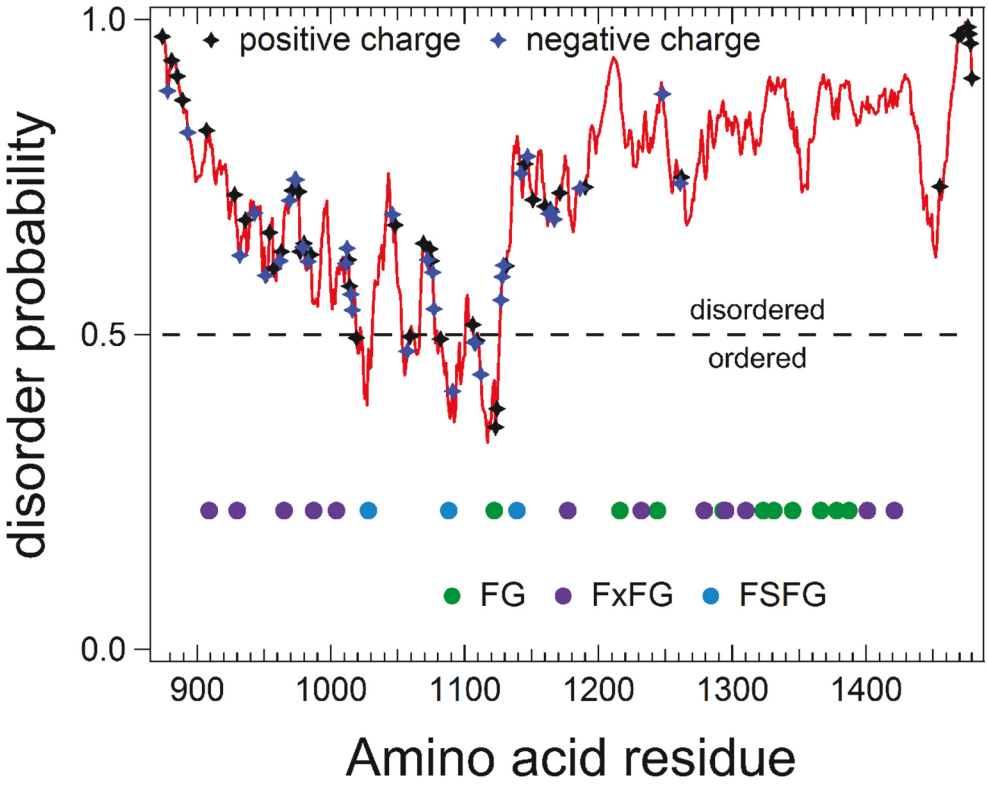

Figure 2-5 – Sequence properties of the cNup153 construct. The plot shown in red was generated using PONDR-FIT and predicts the location of disordered structures (values>0.5) and ordered structures (values<0.5). The exact positions of (i) charged residues and (ii) distinct FG repeat motifs (i.e., GLFG, FSFG, FxFG, and FG)[52], [61] are color-coded along and below the plot, respectively. Positively charge amino acids (Arg, Lys) are shown in black while negatively charge residues (Asp, Glu) are blue. General FG repeats are colored in green, specific repeat motives such as FxFG and FSFG are purple and light blue, respectively. Notably, cNup153 does not contain GLFG repeats. The amino acid residue of cNup153 is shown with respect to full length human Nup153. PONDR-FIT is freely available at http://www.disprot.org/pondr-fit.php.

2.3 SPR analysis of Kapβ1 binding to cNup153

SPR measurements were performed to verify that the purified proteins retained their binding-functionality in solution. Based on a newly developed method by Schoch *et al.*, SPR further allows to quantitatively attain the

relationship between Kap-FG binding affinity and the conformation of end-tethered FG domains [102], [104], [127].

After immobilization of cNup153, Kapβ1 binding was monitored by titration in the following sequence: 0.062, 0.125, 0.25, 0.5, 1, 2, 4 and 11 µM (Figure 2-6). By plotting the respective equilibrium response (R_{eq}) obtained from the sensogram for each injection against the corresponding receptor concentration, equilibrium binding constants (i.e., K_D) can be calculated (Figure 2-6a).

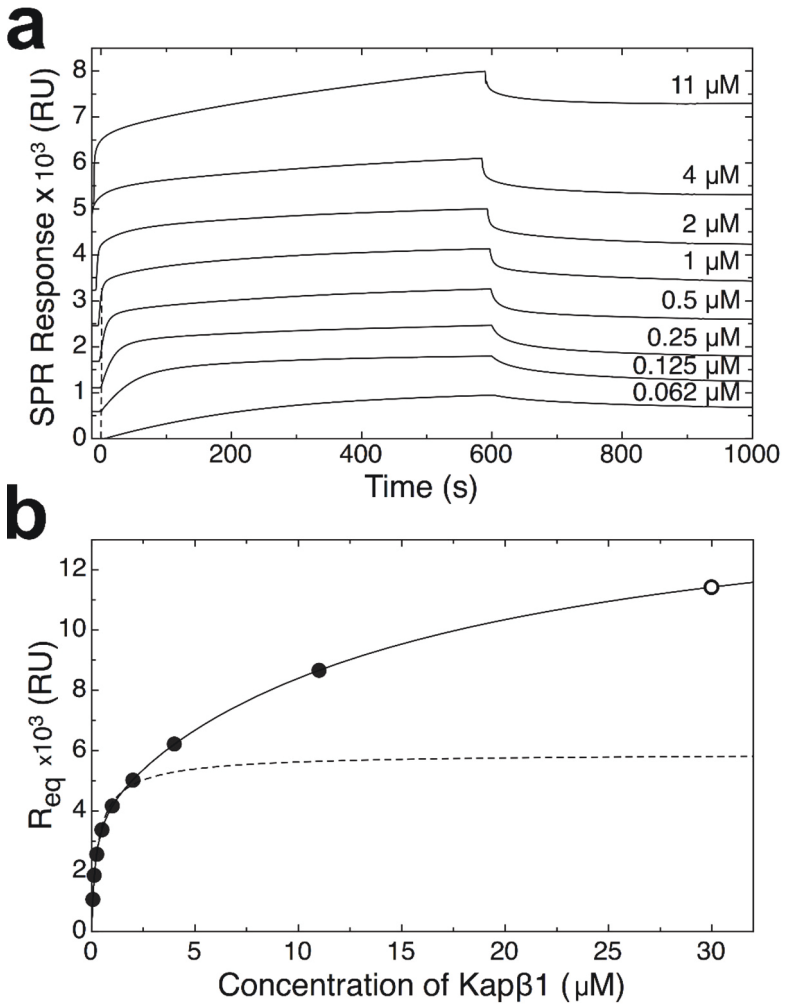

Figure 2-6 – Raw sensogram of Kapβ1 binding to the FG domain layer of cNup153. (**a**) The SPR sensogram represents Kapβ1 binding to the cNup153 layer (initial height: $d_{initial}$ = 12.6±0.1 nm; inter-FG domain grafting distance: g = 5.8±0.06 nm). (**b**) Dependence of the SPR equilibrium response (R_{eq}) on the injected Kapβ1 concentration. The solid line represents a best-fit two-component Langmuir isotherm with K_{D1} = 174 ± 12 nM and K_{D2} = 15.3 ± 2.9 µM to R_{eq} (black circles; the total amount of Kapβ1 bound). The dashed line represents a best-fit single-component Langmuir isotherm with K_D =

245 ± 26 nM within the range of 62.5 nM to 2 µM Kapβ1. The open circles at 30 µM are obtained by the extrapolation of the Langmuir isotherm to this concentration.

The Kapβ1-cNup153 binding equilibrium is only poorly described by a single Langmuir Isotherm, as resulting fits where not acceptable over the whole range of concentrations (Figure 2-6b, dashed line). Instead, the experimental Kapβ1 binding data obtained requires a two-component Langmuir isotherm fit (full line in Figure 2-6 and section 2.3.1). This behavior is not limited to cNup153, but was observed for several other FG domain bearing proteins (e.g., Nup214, Nup62, Nup98) [104].

In addition to common SPR applications, where the binding and unbinding of different analytes is measured, injections of non-interacting BSA molecules allow measurements of the total exclusion volume of surface-tethered proteins. This gives their average layer-thickness d [101], [127]. Figure 2-7 shows how subsequent changes in FG domain thickness due to Kapβ1-binding can be correlated to the relative arrangement of Kapβ1 molecules bound within the layer (section 2.3.2). The layer thickness is related to the number of Kapβ1 layers formed. This relation is given as 2200 RU or 1000 Da/nm^2 based on the amount of material that corresponds to the equivalent of 1 (net) Kapβ1 layer [101] (section 2.3.3 and 2.3.4). Starting from an initial layer-thickness $d_{initial}$ ~12.5 nm, the empty cNup153 layers thickness increases non-monotonically with Kapβ1-concentration. At 0.25 µM, the first layer of Kapβ1 is formed. This is accompanied by a marginal expansion of the FG domain layer (d_{layer1}~14 nm , i.e. within d_h of Kapβ1=12 nm[57]). At high Kapβ1 concentrations, the cNup153 layer can incorporate up to five layers while simultaneously expanding more than two-fold in thickness [104] (Figure 2-7).

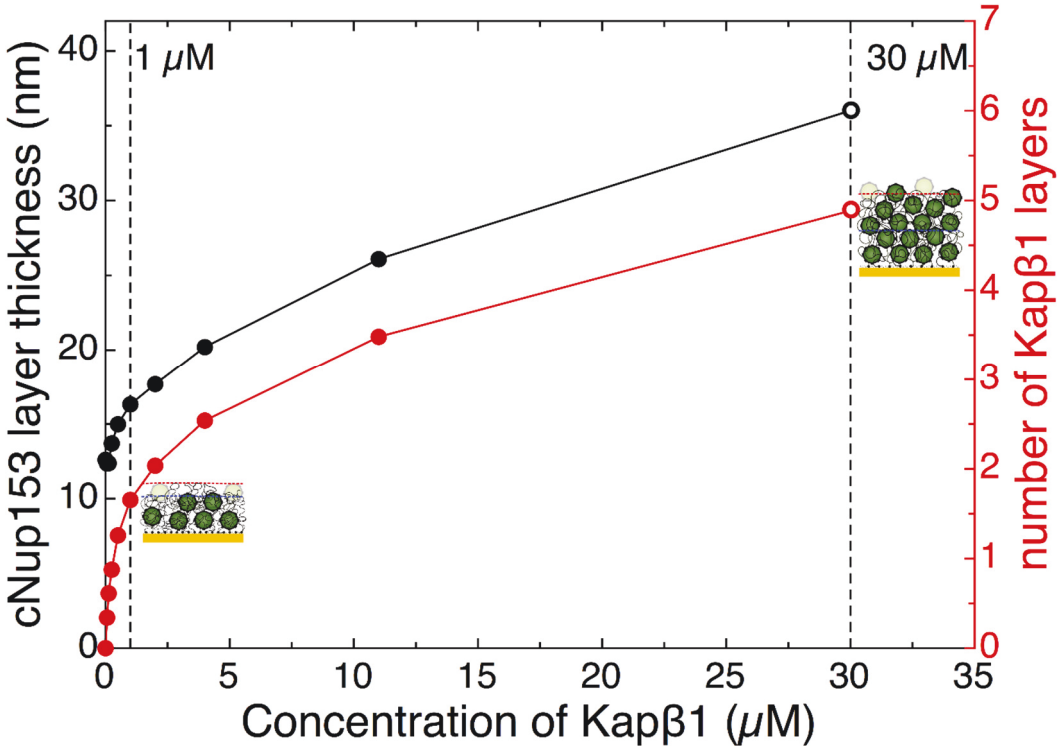

Figure 2-7 – Influence of Kapβ1 concentration on the thickness of the cNup153 layer and the number of Kapβ1 layers bound. Height changes in the cNup153 layer (black) were measured using BSA at increasing Kapβ1 concentrations as described previously [102], [127]. The number of Kapβ1 layers (red) that occupy cNup153 can be calculated based on the SPR-derived surface density of bound Kapβ1. The closed circles are experimental data points; the open circles result from the extrapolation to 30 µM.

The representative molecular occupancy of Kapβ1 that is reached within the cNup153 layer at low and high applied Kapβ1 concentrations (see cartoon insets in Figure 2-7) can be correlated to the equilibrium analysis in Figure 2-6b. Here, a high affinity species (K_{D1} ~175 nM) describes binding of Kapβ1 to a pristine cNup153-layer early on (i.e. at low concentrations). The increase in Kapβ1 occupancy at higher concentrations leads to a reduction of free FG repeats within the layer, which results in a second low affinity species (K_{D2} ~15 µM). At that stage, fewer FG repeats are available and Kapβ1 binding becomes weak as avidity is reduced. As considered in chapter 1.4.2, I attribute the emergence of a second K_D to restricted access to FG domains, where

receptors start to sterically hinder each other with increasing occupancy. This results in Kapβ1-cNup153 configurations decreased in bound sites per Kapβ1 and a consequently lower affinity. In context of nucleocytoplasmic transport, these results support the notion that at physiological Kapβ1 concentrations (~10 µM [103]), several kinetic species exist inside a NPC that is preoccupied by ~100 Kapβ1 molecules [103], [116] (see subsection 1.4.3.6).

2.3.1 Determination of the binding equilibrium constants

The effective equilibrium dissociation constant (K_D) was determined by fitting the SPR-response of bound Kapβ1 at steady state versus Kapβ1 bulk concentration with a Langmuir absorption isotherm of i components with i= 1 or 2,

$$R_{eq} = \sum_i R_{max,i} \frac{C_{\mathrm{Kap\,\beta1}}}{C_{\mathrm{Kap\,\beta1}} + K_{D,i}} \qquad \text{Eq. 2-1}$$

where $C_{\mathrm{Kap\,\beta1}}$ is the bulk Kapβ1 concentration and $R_{max,i}$ denotes the maximal binding responses for the species with $K_{D,i}$. At high ligand surface density the experimental data points were best fit by a two-component Langmuir isotherm.

2.3.2 Measurement of the FG-layer thickness

Following the approach developed by Schoch *et al.* [102], [127], the layer thickness for the FG domains immobilized on the sensor chip surface is calculated using

$$d_2 = \frac{l_d}{2} \ln\left(\frac{R_1}{R_2}\frac{m_2}{m_1}\right) + d_1 \qquad \text{Eq. 2-2}$$

, where R_1 and R_2 are the responses measured for the injection of BSA in the reference cell and sample cell, respectively. l_d is the decay length for the

evanescent field, m_2/m_1 is a measure of the respective cells sensitivity and was shown to be 1 for the instrument used [127]. d_2 and d_1 denote the molecular layers thickness in the corresponding cells [102], [127]. Here, BSA acts as a non-interacting probe, whose response is a function of its penetration depth into the evanescent field above the sensor surface. This depth is directly coupled to the height of the layer, which restricts the BSA molecules from approaching the surface and allows to directly correlate surface density of FG domain-bound Kapβ1 with the change in FG-layer thickness (Figure 2-7).

2.3.3 Measuring the grafting distance of surface anchored proteins using SPR.

All SPR measurements were performed at 25 °C in a four flow cell Biacore T100 instrument (GE Healthcare) as described before [102]. Briefly, $C_{17}H_{36}O_4S$ (PUT, Nanoscience) and the cysteine-modified FG domains of cNup153 were semi-covalently grafted via thiol-binding to a reference- and sample cell, respectively. Bovine serum albumin solution was prepared in phosphate buffered saline (PBS, pH7.2) at 10 mg/ml. Kapβ1 was dialyzed prior to experimentation into PBS pH 7.2. All buffer solutions were filtered and degassed before use. All reagents and protein samples were centrifuged for 10 min at 13000 rpm to remove air bubbles. It was previously shown that there is a linear dependence between the change of the surface resonance response upon ligand binding (RU) and the amount of the bound protein per surface area (1300 RU=1 ng/mm²). Therefore a surface grafting distance (g in nm) in between molecules of mass M_W can be calculated using:

$$g = \sqrt{\frac{1300 \quad M_W \quad 10^{21}}{N_A \quad RU}} \qquad \text{Eq. 2-3}$$

Where N_A is the Avogadro constant [102], [127].

2.3.4 Definition of a Kapβ1 layer

Eq. 2-3 is used to estimate the next-neighbor distance between Kapβ1 molecules within the cNup153 layer. This distance can be smaller than the average diameter of a Kapβ1 molecule because Eq. 2-3 provides a projection of all bound molecules into a single plane. In this case, more than one Kapβ1 layer is formed [104].

2.4 Evaluating non-specific binding to FG domain cNup153

Since nucleocytoplasmic transport takes place within the crowded environment of the cell, I intended to clarify whether FG domains are truly repulsive, or if they exhibit binding interactions with non-specific proteins from cell lysate. To this end, pull-down assays with cNup153-functionalized beads in bacterial cell lysate were performed. As bacteria do not possess NPCs or proteins functionally associated with NCT, no proteins from the lysate are expected to interact with cNup153 in a specific manner.

2.4.1 Preparation of His-depleted *Escherichia coli* Lysate

Rosetta *E. coli* BL21 (DE3) cells were grown overnight at 37 °C, harvested and frozen. Thawed pellets were lysed by sonication in lysis buffer (10 mM TrisHCl, pH 8, 100 mM NaCl, 1mM DTT supplemented with DNAase, lysozyme and Roche protease inhibitor cocktail), cleared by centrifugation and the lysate incubated over night with His-select Ni-NTA beads (Sigma-

Aldrich). PMSF was added to 0.1 mM to the cleared lysate and stored at 4 °C until use.

2.4.2 Pull-down of *E. coli* lysate using cNup153

Maleimido-functionalized melamine resin beads (nominal diameter 0.96 µm, microparticles GMBH) were diluted to ~0.014% solids in PBS containing cNup153 or BSA, respectively, and incubated for 2 hours at room temperature with end-over-end mixing to allow covalent attachment. Beads were then blocked 1 hour at room temperature by adding BSA to 1% w/v, washed twice by centrifugation and were resuspended in PBS containing 1% BSA. His-depleted *E.coli* lysate was added to 0.3 mg/ml to the beads and incubated for 1 hour at room temperature, then washed 3 times as described above. The pellet was resuspended in sample buffer and boiled for 5 minutes at 95 °C before 12% SDS-PAGE (0.1% SDS) and stained with coomassie blue.

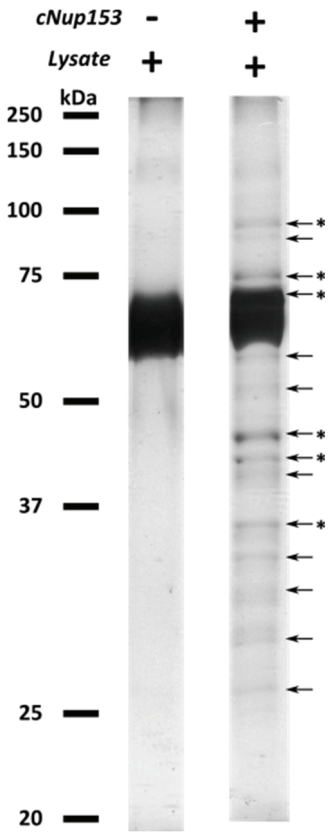

Figure 2-8 – Several proteins from *E.coli* lysate bind to cNup153. The most prominent bands were identified by mass-spectrometry (indicated with *).

Figure 2-8 shows several proteins from *E.coli* lysate which bound to cNup153, but not to passivated beads. Analysis of the six most prominent bands in Figure 2-8 using mass-spectrometry identified at total of 136 proteins. Table 1-1 lists the proteins with the highest score in each band.

Table 2-1 – Most prominent *E. coli* proteins interacting with cNup153. The six most prominent bands of the pull-down in Figure 2-8 as identified by mass-spectrometry. Listed are the proteins with the highest score in each band.

Band	**MW [kDa]**	**Calc. pI**	**Name (Protein from *E. coli*)**
1	77.5	5.38	Elongation factor G
2	72.2	5.67	Transketolase 1

3	70.5	8.72	Cold-shock DEAD box protein A
4	43.3	5.45	Elongation factor Tu 1
5	41.1	5.22	Phosphoglycerate kinase
6	39.3	4.96	Outer membrane protein F

The complete mass-spectrometry result can be found in the Appendix (Table 10-1). The majority (89%) of all proteins identified had a predicted pI < 7.2 (on average 6.08 ± 1.06 SD) and are hence positively charged at pH 7.2. As cNup153 is negatively charged at pH 7.2 (predicted pI of 9.1), these interactions are likely of electrostatic nature. *In vivo*, FG Nups and Kaps are in general of opposite charge at neutral pH (i.e., FG Nups are positively charged while Kaps tend to be negatively charged [128], [129]). Interestingly, enhanced transport rates of charged cargo through NPCs were observed with increased negative net charge [130]. This is possibly due to enhanced association-rates by electrostatic attraction [55]. In addition to my result, analysis of Kap-FG binding in the presence of bacterial lysate revealed that competition from non-specific proteins weakens the affinity of Kaps to FG Domains [62].

Based on the unspecific interactions of proteins from the lysate with FG domains, I conclude that in the complex environment of the living cell, unspecific protein interactions with FG domains are likely to play are role in nucleocytoplasmic transport.

Chapter 3

3 Setting up the PFM experiment

Kaps access NPCs by interacting with FG-domains. Single molecule fluorescence studies revealed that during their translocation, Kap and Kap-cargo complexes perform a random walk inside the pore [11]. Hence, Kap-FG domain mediated translocation through NPCs is driven by Brownian motion, which describes the erratic motion of particles in a fluid that results from collisions with atoms or molecules in the liquid. Optical-trap-based photonic force microscopy (PFM) provides an effective means to study such random motion of particles in suspension [131]–[134]. Here, I use PFM as a biophysical tool to explore the effect of Kap concentration on the diffusion of Kapβ1-functionalized colloids (Kap-probes) on a layer of FG domains from Nup153.

3.1 The Photonic Force Microscope

I used a custom-built experimental setup that combines optical trapping, single particle interferometric tracking and ensemble particle tracking by video microscopy to scrutinize probe-surface interactions on the local and ensemble level, respectively. In the following, I explain the experimental setup, introduce optical trapping and describe how Kap-probe trapping is accomplished in PFM.

3.1.1 The PFM setup

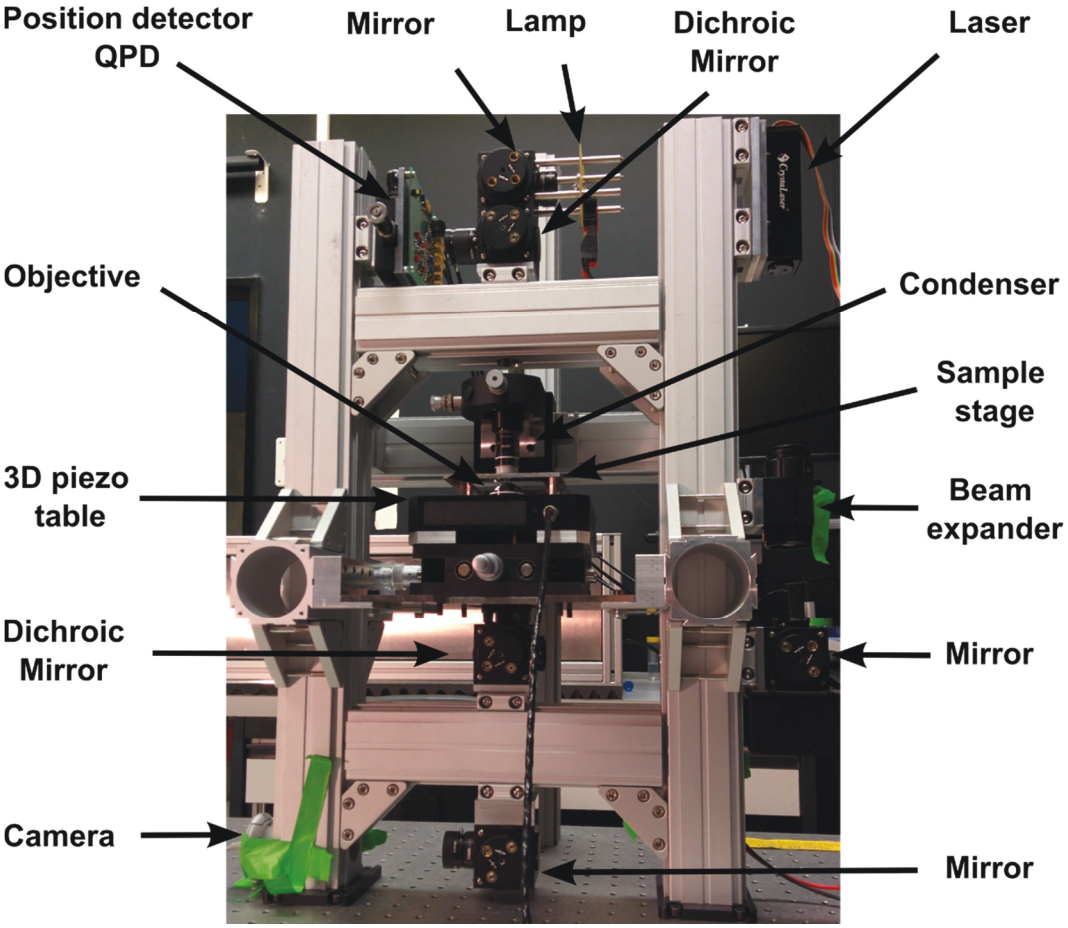

Figure 3-1 – Photography of the photonic force microscope setup. The PFM is mounted on a Benchtop vibration isolation optical table to dampen low frequency noise (Newport). See text for description.

The laser beam (IR, red) is expanded 10-fold by a beam expander (Sill optics), attenuated if necessary by a neutral density filter (NF), reflected by a dichroic mirror (AHF Analysetechnik AG) and focused by the objective lens (1.2 NA 60x water immersion, Olympus UPLSAPO) into the sample chamber. The scattered IR light is collected by a condenser (0.9 NA 63x water immersion, Zeiss Achroplan) and directed by a second dichroic mirror onto the quadrant photodiode (QPD) which is fixed on a XY-translational stage (OWIS) to allow manual centering of the detector relative to the IR-beam. A 50 W halogen light source (Lamp) illuminating the object plane is reflected by a mirror but

transmitted through both dichroic mirrors. The image created by the condenser and the objective is reflected by another mirror onto the camera (Microsoft, 14 px/µm)[135]. A schematic of the setup used in this work is given in Figure 3-2.

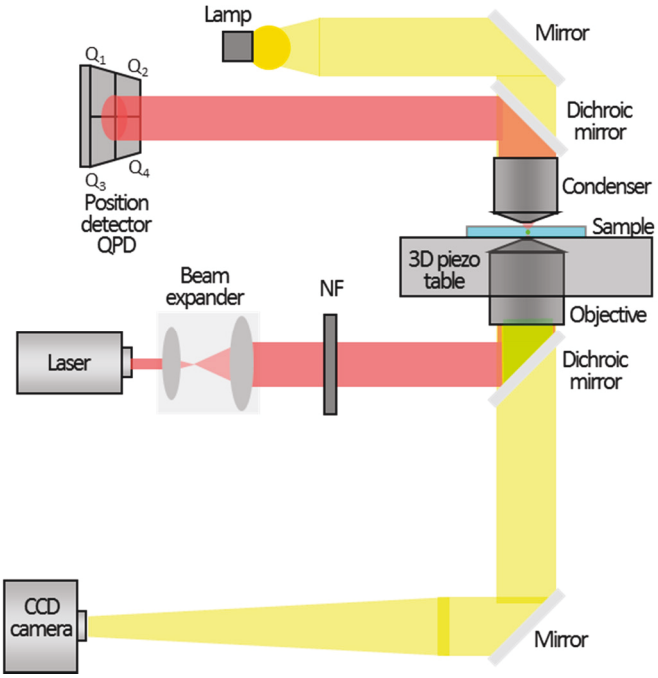

Figure 3-2 – Beam paths in the PFM. Schematic layout of the infrared (IR, red) and visible (yellow) light paths in the experimental setup used in this work. Adapted from Jeney *et al.* [135].

3.1.2 Optical trapping

In general, optical trapping is achieved by focusing a laser beam through an objective with high numerical aperture (NA) [136]. In the focus, the optical forces sum up to a harmonic restoring force, $F_{trap} = \quad kx$, where k is the traps stiffness and x the probes displacement from the focus [135]. The forces any dielectric particle experiences near the focus can classically be decomposed into two components: Scattering force and gradient force [137]. The scattering force describes the momentum transfer from scattered and adsorbed photons on the probe (also known as radiation pressure or photon pressure). It acts directly parallel to the optical axis, pushing the probe in the direction of light

propagation (i.e. away from the focus). The gradient force is of electromagnetic nature and acts along the gradient in the electromagnetic field, effectively pulling the probe towards the region of maximum field strength. For stable optical trapping, the gradient force must exceed the scattering force. This requirement can be met by using high numerical aperture objectives to create a steep gradient in the beam. The gradient can further be supported by utilizing a laser with a Gaussian intensity profile, as the electromagnetic field and therefore the gradient force is proportional to the lasers intensity [137]. While these two forces only provide a rough yet intuitive understanding of the optical forces acting on the probe, a complete theoretical description in the special case where the probes size is comparable to the wavelength λ of the laser light is still unavailable to date [137]. In practice, however, the majority of objects used or studied in an optical trap fall into this size regime of 0.1-10 λ , as is the case for this thesis.

3.1.3 Particle tracking and data acquisition

A Kap-probe trapped within the beam focus will scatter the laser light. Subsequent probe tracking is accomplished by collecting the resulting interference pattern on the QPD in the back focal plane of the condenser along the optical axis [136]. Known as single particle tracking by interferometric position detection (or optical tracking interferometry, OTI) [138], [139], this method ensures that the probe always remains within detection range, as optical trap and detection beam are intrinsically aligned. Ensemble tracking was realized using conventional video microscopy by collecting the visible light (yellow in Figure 3-2) in the imaging plane conjugated to the sample stage. This allowed for the analysis of collective probe behavior captured within the complete field of view (~ 57 x 43 µm). A

detailed description of the ensemble probe tracking and analysis based on our experimental data presented in chapter 5 is given sections 5.1-5.3.

The sample chamber in this setup is mounted onto a 3D-piezo stage (P-561.3CD with E-710 digital controller, Physkalische Instrumente) [131], [140]. Probes are trapped in the focus of a Gaussian trapping beam produced by a diode-pumped, ultralow-noise Nd:YAG laser with a wavelength of λ=1064 nm and a maximal output power of 500 mW in continuous-wave mode (CrystaLaser). Fluctuations in the position of the probe are detected in 3D by an InGaAs quadrant photodiode with a diameter of 2.0 mm (G6849, Hamamatsu Photonics). The signals from the quadrant photodiode are fed into a custom-built preamplifier [141], [142], which provides two differential signals between the photodiode quadrants, giving the fluctuations in the X and Y directions, and one signal that is proportional to the total light intensity, yielding the fluctuation in the direction parallel to the optical axis, Z. Subsequently, differential amplifiers were used to adjust the preamplifier signals for optimal digitalization by the data acquisition board with a dynamic range of 14 bits. The conversion of raw data from V to nm and the trap stiffness (k) was performed as described in section 3.4

3.2 Probe-functionalization and analysis

In the following, I explain how probe functionalization with Kapβ1 molecules was realized and verified. To this end, I used antibodies to (i) couple Kapβ1 to the probes and (ii) perform indirect immunofluorescence microscopy to test for successful probe functionalization and biochemical activity.

3.2.1 Antibodies

I used the following antibodies for probe-functionalization and indirect immunofluorescence microscopy:

Primary antibodies: Mouse monoclonal penta-His Antibody devoid of bovine serum albumin (BSA-free, α-pHis, 34660,) was purchased from Qiagen. The dissociation constant (K_D) for this antibody to its epitope is between 1 and 50 nM (manufacturer's value). Rabbit polyclonal Anti-NTF97/ Kapβ1 antibody (α-Kapβ1, ab45901) and mouse monoclonal anti-Nup153 antibody (α-Nup153/QE5, ab 24700) were purchased from Abcam. *Secondary antibodies* were purchased as follows: Alexa Fluor 488 goat anti-mouse IgG (Invitrogen), Alexa Fluor 488 goat anti-rabbit IgG (Molecular Probes), Alexa Fluor 568 goat anti-rabbi IgG (Invitrogen), Alexa Fluor 568 goat anti-mouse IgG (Invitrogen) and anti-mouse IgG conjugated with alkaline phosphatase for Western Blot (A3562, Sigma).

3.2.2 Fluorescence imaging

Fluorescence imaging was done using an inverted microscope setup described previously [143]. In brief, fluorescence images were obtained with a 1.46 NA TIRF 100x oil immersion objective (Leica Microsystems, Germany) with an additional tube magnification of 1.6x in a Leica DMI6000 B inverted microscope. Fluorescence was excited using a mercury short-arc reflector lamp (Leica EL6000) and appropriate bandpass filter cubes for the dyes used. Images were taken with an EMCCD camera (C9100-02, Hamamatsu, Japan) in 14-bit mode with a resulting pixel size of 50 nm/pixel.

3.2.3 Generation of Kap-probes

Figure 3-3 illustrates how His_6-Kapβ1 was attached to the probes via high affinity His-tag antibodies (section 3.2.1) cross-linked to polystyrene microspheres presenting primary amines. This strategy allowed for the formation of stably bound probe-protein complexes while ensuring the native conformation of Kapβ1.

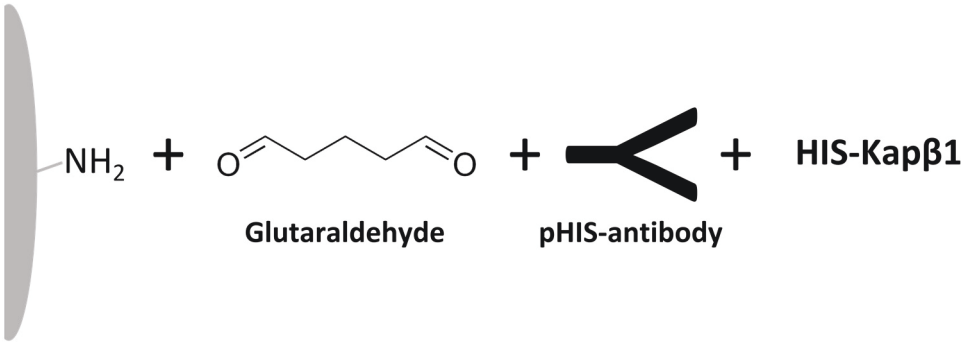

Figure 3-3 – Schematic of the probe chemistry. Glutaraldehyde reacts rapidly and irreversibly with amine groups around neutral pH (7-9) [144], [145], thereby crosslinking the penta-his antibody (pHIS) to the probe. His_6-Kapβ1 is captured by the pHIS antibody from solution, forming a stable complex with $K_D \approx$ 1-50 nM (supplier value).

Polystyrene (PS)-NH_2-Beads (PA03N, Bangs Laboratories, Inc., nominal diameter 900 nm) were suspended in 1 ml filtered PBS pH 7.2 (Gibco) to 0.1% solids in low protein adsorbance tubes (Sarstedt), washed 3x with 1 ml PBS pH 7.2 by 4 min centrifugation at 13.5 krpm in a tabletop centrifuge (Eppendorf). Resulting pellets were resuspended by pipetting and briefly vortexed followed by ultrasonication for 2 min (Bandelin Sonorex RK100). Washed pellets were resuspended in PBS containing 10% glutaraldehyde (GA, Sigma-Aldrich, G5882) at pH 7.5 [144], [145], briefly vortexed and ultrasonicated for 5 min before being incubated for 6 h in a Hulamixer at

room temperature (Invitrogen). Beads were subsequently washed 3x in filtered PBS pH 7.2 as described above until no residual GA could be detected in the supernatant. A volume of 100 µl GA-activated beads at 0.1% solids was added to 900 µl PBS containing 40 µl 0.2 µg/µl BSA-free IgG pentaHis (Qiagen), gently mixed by pipetting and incubated overnight at 4 °C in a Hulamixer. The next day BSA (Sigma-Aldrich) was added to 1% and incubated for 1 h at 4 °C in a Hulamixer. Afterwards, the beads were washed twice with 1% BSA in PBS pH 7.2 using centrifugation, gently resuspended by pipetting and stored at 4°C. Prior to experimentation, beads were incubated in 500 µl PBS pH 7.2 containing 1% BSA and 25 µg Kapβ1 for two hours at room temperature on a rotating shaker. Unbound Kapβ1 was removed by centrifugation and probes were gently resuspended in PBS pH 7.2 containing 1% BSA and the desired concentration of Kapβ1.

3.2.4 Analysis of Kap-probes

To measure the amount of Kapβ1 molecules bound per probe, beads were functionalized with pHis antibody and stored in PBS pH 7.2 containing 1% BSA as described above. 25 µg Kapβ1 was added and allowed to bind to the probes for two hours at room temperature on a Hulamixer. Afterwards, probes were washed twice in PBS by centrifugation and their concentration was determined using a reference curve obtained from GA-activated beads of the same lot recorded at a wavelength of 700 nm in PBS pH 7.2 (Figure 3-4a) [146].The final pellet was separated from its supernatant (S/N), dissolved in sample buffer, boiled for 5 minutes at 95 °C and then analyzed using 15% SDS PAGE (0.1% SDS) in combination with silver-staining [147] (Figure 3-4b). The concentration of the bound fraction was calculated by comparing

band intensity to a dilution series of purified Kapβ1 of known concentrations using FIJI (ImageJ). This resulted in a final amount of ~1.8x10^{-2} g Kapβ1 per g probes (i.e. ~7.3 fg Kapβ1 per single probe) or ~1 Kapβ1 molecule per 58 nm^2, respectively.

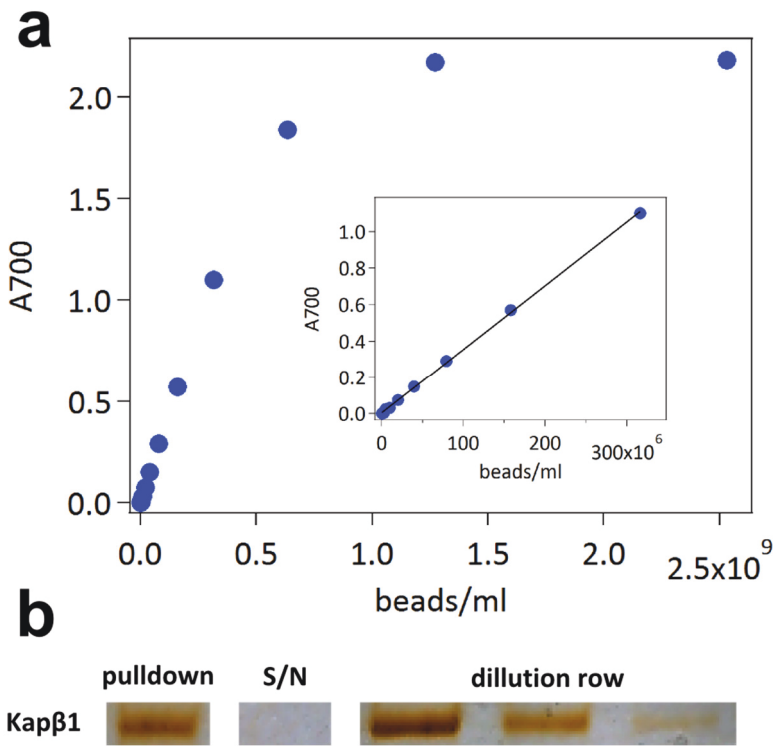

Figure 3-4 – Estimation of bound Kapβ1 per probe. Probes were prepared as described above and separated from solution after loading with Kapβ1. Quantitative analysis of Kapβ1 molecules pulled down and subsequent comparison to standard curves of (**a**) probes and (**b**) solutions of known Kapβ1 concentrations revealed dense packing of individual molecules on the Kap-probes surface. The inset depicts data points within the linear region of (**a**).

To further verify successful probe functionalization with (i) GA, (ii) pHis, (iii) Kapβ1 and to assay the overall biochemical activity of the probes, I applied indirect immunofluorescence staining and fluorescence microscopy (Figure 3-5 – and Figure 3-13).

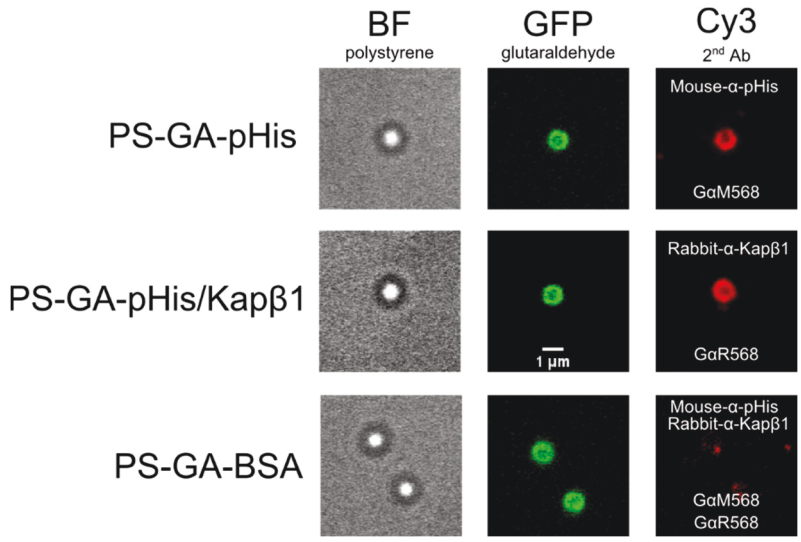

Figure 3-5 – Biochemical activity of Kap-probes. Probes were prepared as described above and individual components identified by fluorescence microscopy. While glutaraldehyde-functionalization could be revealed by observing its autofluorescence in the GFP channel (middle column), the presence of (i) pHis antibodies and (ii) subsequently bound Kapβ1 was revealed by indirect immunofluorescence microscopy (top row and middle row, respectively).

Probes were prepared as described above, functionalized with the pHis-antibody or BSA as a negative control, respectively (Figure 3-5, 1st & 3rd row) and incubated for 2 h at room temperature with Kapβ1 (2nd row) as indicated. Glass slides were cleaned as described in section 3.3 and activated with 0.01% poly-l-lysine (Sigma-Aldrich) for 1 h at room temperature to aid attachment of the probes. After incubation for 1 h at room temperature with the glass slides, probes were blocked for 1 h at room temperature in PBS pH 7.2 containing 1% BSA, gently washed in an excess of PBS pH 7.2 containing 1% BSA and incubated with the primary antibodies dissolved in PBS pH 7.2 containing 1% BSA as indicated in Figure 3-5, 3rd column, for 1 h at room temperature. Unbound primary antibodies were removed by gentle washing in an excess of PBS pH 7.2 containing 1% BSA followed by incubation with the secondary antibodies dissolved in PBS pH 7.2 containing 1% BSA as

indicated in Figure 3-5, 3rd column, for 1 h at room temperature. The slides were subsequently washed gently in an excess of PBS pH 7.2, mounted on standard microscope slides in MOWIOL (Sigma-Aldrich) and imaged (see section 3.2.2) using the brightfield (BF), GFP and Cy3 channel to detect the polystyrene probes, their glutaraldehyde functionalization and the 2nd antibody, respectively. Note that glutaraldehyde is known to be autofluorescent in the GFP channel [148].

3.3 Surface functionalization & chamber preparation

In order to covalently attach cNup153 in an orientated manner to the chamber surface, clean glass surface were silanized and cNup153 subsequently cross-linked to the surface via its thiol-exposing N-terminal cysteine-tag in an "end-on" fashion (Figure 3-6).

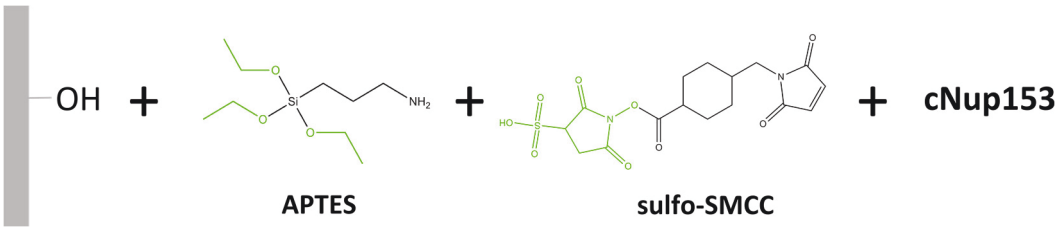

Figure 3-6 – Schematic of the surface chemistry for the covalent grafting of cNup153 to a clean glass surface. After UV-ozone treatment, exposed OH groups react with (3-Aminopropyl)triethoxysilane (APTES), thereby generating free amines (NH_2). Subsequently, the amine reactive NHS ester of sulfosuccinimidyl-4-(N-maleimidomethyl)cyclohexane-1-carboxylate (sulfo-SMCC) will form a stable amid bond with the surface at pH 7-9. In a final step, its second functional group, a thiol-reactive maleimide, will form a stable thioester bond with the cysteine-tag of cNup153 at pH 6.5-7.5. Leaving groups are marked in green.

Coverslips #1 (20 x 20 mm, Menzel-Gläser) were cleaned for 15 min in 200 mM HCl at room temperature, rinsed with H_2O, incubated with 2% Hellmanex III (Hellma) for 1 h at 37 °C, rinsed thoroughly with H_2O, dried with N_2, subjected to UV-Ozone (Jelight Company, Model No. 42A-220) for 30 min, immediately immersed in 1% (v/v) APTES in anhydrous toluene (both Sigma-Aldrich) and incubated for 2 h at room temperature inside a desiccator under argon atmosphere. Coverslips were subsequently rinsed with a large volume of 1) H_2O, 2) ethanol and then 3) H_2O again before being dried with N_2. A volume of 500 µl/slide of 2 mg/1.5 ml Sulfo-SMCC (Lubio Science) in PBS pH 7.2 was added and incubated for 1 h at room temperature in a

humidified chamber [57], [149]. Slides were again rinsed with large volumes of H_2O, ethanol, and H_2O before being dried with N_2. The PFM sample chamber was then assembled as follows: Standard microscope slides (76 x 26 mm, Thermo Scientific) were rinsed with ethanol and dried under N_2. Double-sided scotch tape was glued on the long sides to approx. 8 mm left and right, leaving a 10 mm gap in between. The activated coverslips were then inversely mounted onto the scotch tape with the maleimide-residues facing the inside, resulting in a chamber with a height of ~100 µm. cNup153 was dialyzed to PBS pH 7.2 for 3 h at room temperature (Spectrapore, 3.5 kDa MWCO). 30 µl cNup153/slide were flushed into the sample chamber and incubated upside down over night at 4 °C in a humidified chamber to allow covalent binding. The next day, the cNup153 solution was replaced by flushing 3x with 100 µl PBS pH 7.2 containing 1% BSA using a pipette and filter paper (Whatman) and blocked for 1 h at 4 °C in PBS pH 7.2 containing 1% BSA upside down in a humidified chamber.

3.3.1 Verification of surface chemistry

To verify the surface chemistry and protein binding functionality, I applied quartz crystal microbalance with dissipation (QCM-D) measurements on a sensor crystal functionalized with the surface chemistry described above.

Briefly, QCM-D measures changes in resonance frequency (Δf) and dissipation (ΔD) of an oscillating sensor crystal upon interaction of molecules with its surface. To a first approximation, a decrease in Δf indicates a mass increase, whereas high (low) values of ΔD indicate a soft (rigid) film [150]. We used an APTES-functionalized SiO_2-sensor and monitored the subsequent binding of (i) sulfo-SMCC, (ii) cNup153 and (iii) Kapβ1 to the surface by recording the shift in frequency as well as dissipation (Figure 3-7). Even

though the interpretation of the data presented in Figure 3-7 is to remain qualitative, the pronounced shifts observed in Δf and ΔD upon injection of cNup153 indicate the successful formation of a soft and hydrated film [151].

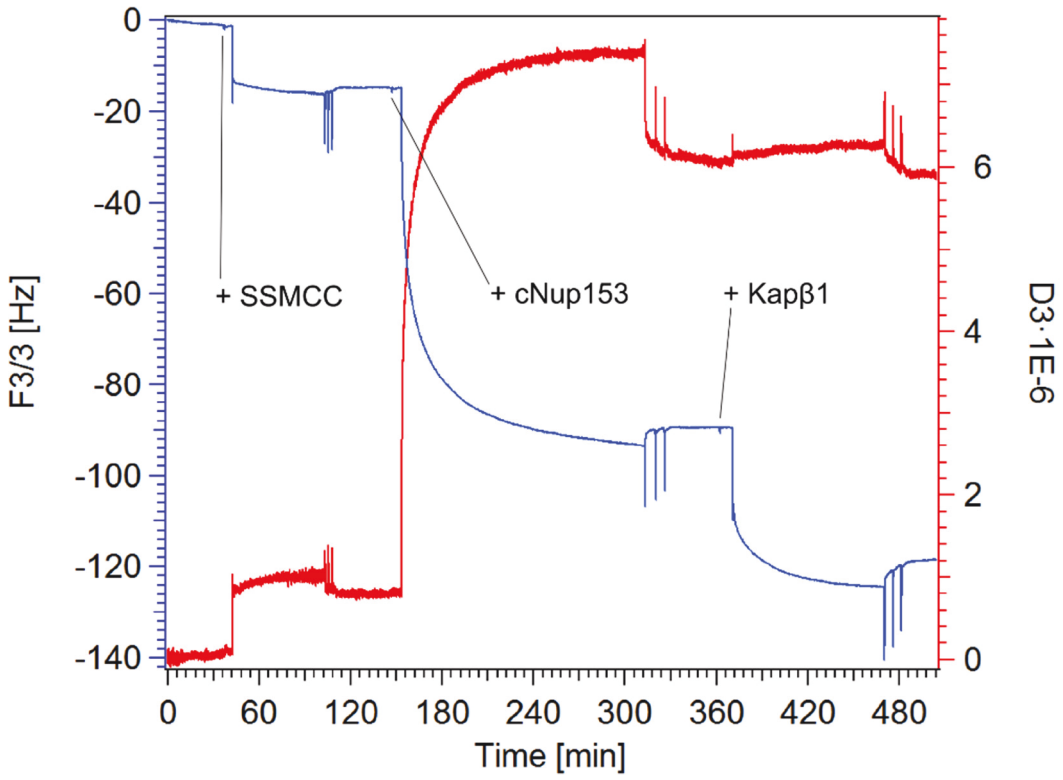

Figure 3-7 – QCM-D analysis of surface chemistry and Kapβ1 binding. Raw QCM-D sensogram recorded with 0.8 Hz depicts the subsequent binding of sulfo-SMCC, cNup153 and Kapβ1 at the indicated positions. Changes in frequency shifts normalized by its overtone number (1st y-axis, blue) and dissipation (2nd y-axis, red) confirm the crosslinking chemistry and subsequent formation of a soft cNup153 layer capable of Kapβ1 binding. Shown here is the 3rd overtone.

SiO_2-crystals (QSX303, q-sense) were cleaned in 2 % Hellmanex III in H_2O for 30 min at 37 °C, rinsed thoroughly with H_2O, dried with N_2 and subjected to UV-Ozone (Model No.42A-220, Jelight Company Inc.) for 30 min [151]. After UV-ozone treatment, the sensor was rinsed with toluene and incubated in 1% (v/v) 3-Aminopropyltriethoxysilane (APTES) in anhydrous toluene solution

inside a desiccator under argon atmosphere for 2 h at room temperature for silanization [149]. The crystal was then subsequently rinsed with toluene, H_2O, ethanol and H_2O again, dried with N_2 and mounted into the instrument (Q-Sense D300). Kapβ1 and cNup153 were dialyzed into PBS pH 7.2. Measurements were performed at room temperature with concentrations indicated below. The sensor was washed in between injections with degassed PBS. Crystals silanized with APTES showed subsequent binding of the crosslinker sulfo-SMCC (2 mg/1.5 ml), cNup153 (3 µM) and Kapβ1 (300 nM), thus confirming the surface chemistry and the solution binding ability of the proteins.

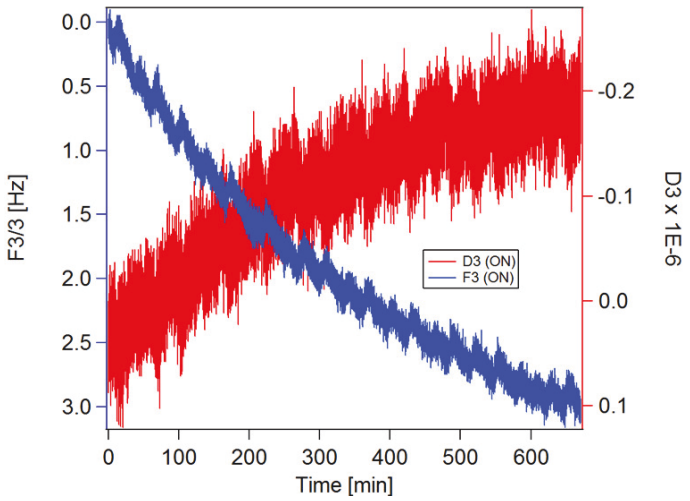

Figure 3-8 – Stability of the APTES-sulfo-SMCC-cNup153 layer. Changes in dissipation and frequency shift of the layer presented in Figure 3-7 were recorded overnight to monitor the layers integrity in time. A minimal frequency shift of ~3 Hz is indicative of a very stable layer with minimal loss of material over ~20 h total measurement time.

Immediately following the QCM-D measurement presented in Figure 3-7, the system was left as is overnight at room temperature to test the stability of the APTES-sulfo-SMCC-cNup153 layer. The frequency only changed for

approximately 3 Hz, indicating that the system is stable even after 20 h of total measurement.

To further characterize the functionalized glass surfaces with respect to cNup153 and Kap binding, I performed indirect immunofluorescence microscopy (similar to section 3.2.4, Figure 3-9).

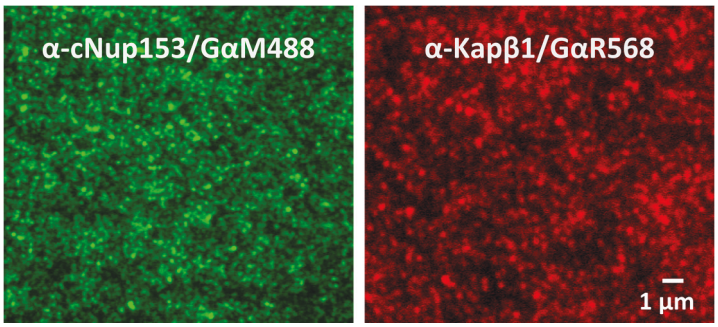

Figure 3-9 – Indirect immunofluorescence microscopy of Nup153-functionalized glass slides.

A glass surface functionalized with cNup153 was washed with PBS pH 7.2, blocked for 1h in PBS pH 7.2 containing 1% w/v BSA and rinsed gently with PBS pH 7.2. Primary mouse anti Nup153 antibody and a secondary goat-anti-mouse Alexa 488 were used to stain for cNup153 (Figure 3-9, left). Fluorescence microscopy revealed successful attachment of cNup153 to the glass surface. A similarly prepared surface with covalently attached cNup153 was incubated with 1 µM Kapβ1 for 1 h at room temperature, washed with PBS pH 7.2 and blocked for 1h in PBS pH 7.2 containing 1% w/v BSA before gentle rinsing with PBS pH 7.2. Subsequent staining with primary rabbit anti Kapβ1 antibody and secondary goat anti rabbit alexa568 revealed the presence of Kapβ1 on the cNup153 presenting surface.

3.4 Analysis of Kap-probe motion recorded in PFM

After generation of Kap-probes and cNup153-surfaces, I analyzed their behavior in the PFM. In the following I will introduced the data recording and analysis procedure.

In the optical trap, the probes position x_i as captured by the QPD in direction i is recorded in units of volt and connected to the probes real position in meters by a calibration factor β_i, where $x_i\,[m] = \beta_i \;\; x_i\,[V]$. I obtained this calibration factor by fitting an experimentally obtain power spectral density (PSD) calculated for a probe ~12 µm away from the surface to a theoretically generated one [152]–[154] (Figure 3-10, solid red line). Besides β, the traps stiffness k can be obtained simultaneously with this method. Figure 3-10 shows a one-dimensional PSD of a 900 nm-diameter probe recorder over 20 s as calculated from raw data (inset). Data was obtained under typical experimental conditions in a solution of PBS pH 7.2 containing 1% w/v BSA at T= 22 °C.

The power spectral density of a perfectly random process typically results in a constant power density over the whole frequency regime (i.e. white noise). In an optical trapping potential, however, the Brownian motion is only free for a certain time τ_k after which the harmonic restoring force acts on the probe, effectively slowing it down [135]. This is reflected in a prominent decay of the PSD at a characteristic corner frequency $\omega_{c,i}$, which is intimately linked to the traps stiffness k_i by $\omega_{c,i} = \frac{k_i}{6\pi\eta r}$, where η and r denote the fluids dynamic viscosity and the probes radius, respectively. The characteristic timescale of the harmonic restoring force can therefore be expressed as $\tau_k = \omega_{c,i}^{-1}$, i.e. ~2 ms for a probe under the aforementioned conditions [135].

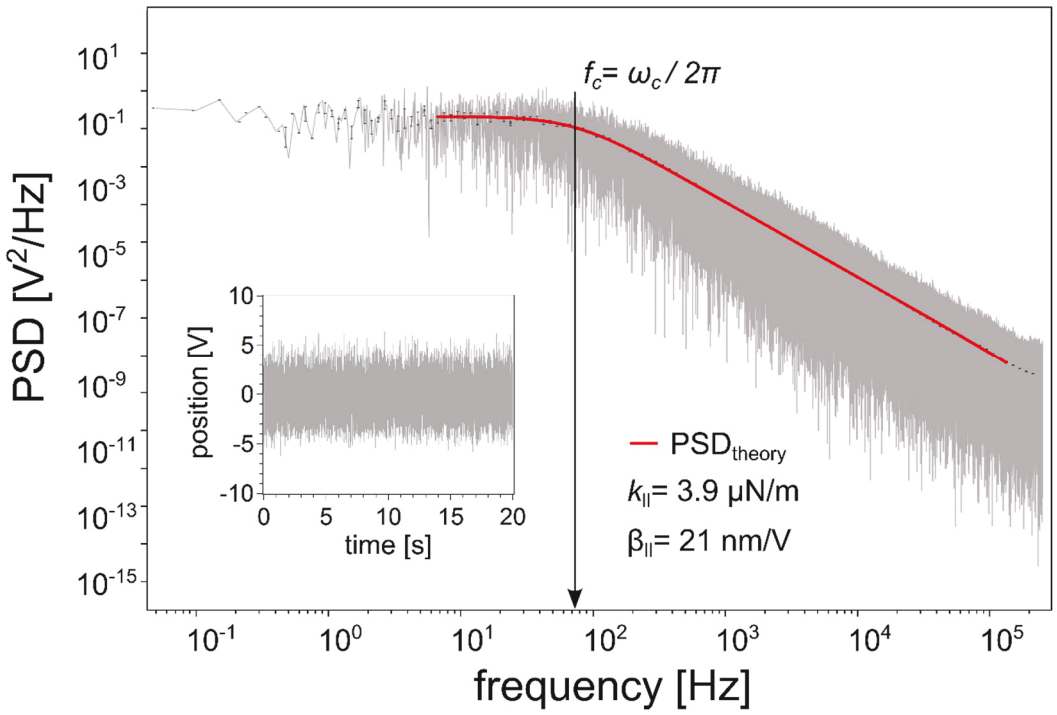

Figure 3-10 – Instrument calibration. Power spectral density of a probe with radius 450 nm recorded at a frequency of 0.5 MHz in the X-direction, i.e. parallel to the surface, at a height of ~12 µm calculated from raw data (inset, shown is the full acquisition range). The PSD is blocked in 20 bins per decade and fitted to a theoretical PSD (solid red line) according to supporting references [152]–[154] using a custom-made software, yielding k= 3.9 µN/m and β= 21 nm/V in the respective direction. Arrow indicates the corner frequency f_c. Error bars on the bins represent the standard error of the mean.

The as-obtained calibration factor was used to convert the probes position fluctuations from volts to nanometers. The corresponding timetrace of the henceforth calibrated dataset is shown in Figure 3-11a, which is characterized by its mean position (red) and standard deviation σ (Eq. 3-1):

$$\sigma = \sqrt{\frac{1}{N} \sum_{1} (x - \bar{x})^2} \qquad \text{Eq. 3-1}$$

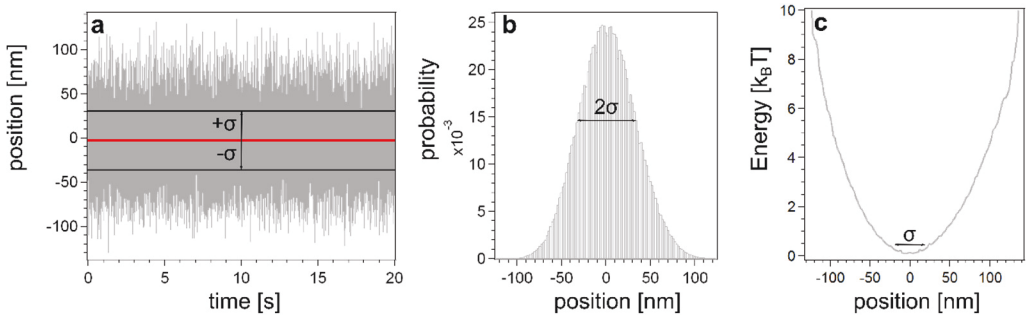

Figure 3-11 – Calibrated dataset. Plotted are the position fluctuations **(a)**, probability distribution **(b)** and free energy landscape **(c)** corresponding to the probe shown in Figure 3-10 with bin size 2 nm and standard deviation $\sigma \approx 32.47$ nm.

Accordingly, the standard deviation is the shape-defining parameter of the resulting Gaussian probability distribution (Figure 3-11b) and free energy landscape, which can be calculated using Boltzmann statistics [133]:

$$p_x = \frac{1}{Q} e^{-E_x/k_B T} \qquad \text{Eq. 3-2}$$

$$\frac{E_x}{k_B T} = -ln(p_x) \quad ln(Q) \qquad \text{Eq. 3-3}$$

Where E_x is the energy at position x divided by Boltzmann's constant k_B times the absolute temperature T and p_x its population probability normalized by the partition function Q. Figure 3-11c depicts the potential energy landscape created by the optical trapping forces as derived from measurement and illustrates that it can be well approximated by a harmonic potential. Notably, σ is closely related to the traps stiffness k in the respective direction i by the equipartition-theorem [155]:

$$\frac{1}{2} k_B T = \frac{1}{2} k_i \sigma_i^2 \qquad \text{Eq. 3-4}$$

$$k_i = \frac{k_B T}{\sigma_i^2} \qquad \text{Eq. 3-5}$$

In the particular case of the data presented in Figure 3-10 and Figure 3-11 (i.e. $\sigma \approx 32.47$ nm), this results in a trapping stiffness of about 3.86 µN/m, in

excellent agreement with the stiffness obtained from fitting the PSD (~3.9 µN/m).

From the position fluctuations of a probe, the diffusion coefficient D can be readily obtained from a line fit to its mean square displacement using Eq. 3-6 [156], which states that the slope of the MSD in one dimension in the case of free diffusion is equal to $2D$:

$$MSD\ (t) = 2Dt \qquad \text{Eq. 3-6}$$

For the same reasons as described above for the PSD, the optical confinement in the PFM will reduce the probes free motion. This results in an attenuation of the MSDs linear growth after τ_k and finally a displacement maximum of the probe which is reflected by a plateau [135] (Figure 3-12).

Practically, the MSD after calibration for each respective probe in one dimension is calculated using

$$MSD\ (t) = \frac{1}{N}\sum_{j=1}^{N}\left[x\left(t + t_j\right) \quad x(t_j)\right]^2 \qquad \text{Eq. 3-7}$$

where $x(t_j)$ is the measured particle position at time t_j, N is the total number of measured positions and t the elapsed recording time (Figure 3-12).

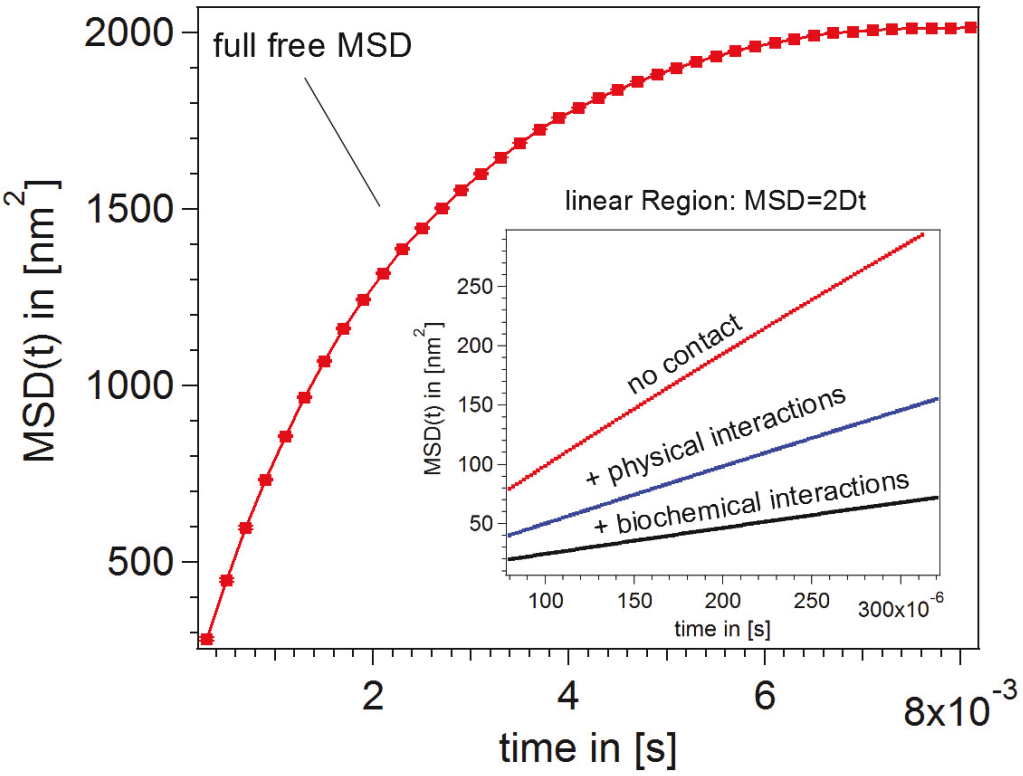

Figure 3-12 – The mean square displacement of a probe is effected by physical and biochemical interactions. MSDs were calculated from experimentally obtained data inside the optical trap recorded with 0.5 MHz under typical experimental conditions in a direction parallel to the surface. The full MSD of a freely diffusing probe with d=900 nm in bulk solution (~12 µm above the surface) is attenuated by the harmonic restoring force after $\tau_k \approx 2\,m\beta$ and saturates into a plateau, reflecting its optical confinement (red, blocked). The inset shows a zoom in on the unblocked MSDs linear region from which diffusion coefficients were obtained: For a probe far away from (red), or in contact with the surface in the absence (blue) and presence of attractive biochemical interactions between Kapβ1 and Nup153 (black). For detailed information and characterization of the probes and surfaces used, see section 3.3 and 3.4.

The as-obtained MSD was fitted in the linear regime (Figure 3-12 inset) using Eq. 3-8 between 1 x 10^{-4} s to 3 x 10^{-4} s , where contributions from the fluid and particle inertia as well as from the trap are negligible for the trapping stiffness used [135], [157]

$$MSD\,(t) = at + b \qquad \text{Eq. 3-8}$$

From a in Eq. 3-8 the diffusion coefficient D can be obtained via Eq. 3-6. The offset b results from limited spatial and temporal resolution which can be estimated from the first point in the MSD [132]. For the PFM-measurements, I calculated a spatiotemporal resolution limit of $\sigma_X = \sigma_Y = \sim 1.6\,nm$ & $2\,\mu s$ and $\sigma_Z = \sim 35\,nm$ & $36\,\mu s$ in the XY- and Z-direction, respectively. Electronic noise contributions below the resolution limit were removed using zero-phase digital filtering as described in Oppenheim *et al.* [158] to post-process the Z-MSDs presented in the results section 4.3. No filtering was applied in the X and Y directions.

As my experiments aim to extract the diffusion coefficient of a Kap-probe interacting with a cNup153-functionalized surface, I considered the influence of (i) the surfaces themselves and (ii) the biochemical protein-protein interactions on the probes motion. In this context, it is important to emphasize that experiments were conducted in PBS supplemented with 1% (w/v) BSA for passivation, i.e. conditions that effectively screen all influence of general hydrophobicity and charge between the surfaces [159], [160]. Experimental prove of passivation is given in section 4.3. Probe diffusion in bulk solution (inset in Figure 3-12, red) is theoretically well described by the Stokes-Einstein relation for the diffusion of a spherical probe in a fluid with drag coefficient γ_0 by

$$D_0 = \frac{k_B T}{\gamma_0};\ \gamma_0 = 6\pi\eta r, \qquad \text{Eq. 3-9}$$

where r is the probes radius and η the fluids viscosity. On the other hand, the physical presence of a surface disturbs the probes diffusion even without direct (biochemical) interaction by inducing a velocity gradient in the water molecules above it. This gradient hampers the probes diffusion when

approaching the surface in both the parallel and perpendicular direction, albeit in asymmetrical fashion, as described by Faxén [161] and Brenner [162], respectively. As the inset in Figure 3-12 shows, these physical interactions are correctly captured in PFM measurements (blue data points). Eq. 3-10 and Eq. 3-11 have been rewritten to describe a probes diffusion coefficients dependence on its height above a surface by combining equation 5 and 6 in supporting reference [163] with Eq. 3-9:

$$D_{\parallel} = D_0\left\{1 \quad \frac{9}{16}\frac{r}{-} + \frac{1}{8}\left(\frac{r}{-}\right)^3 \quad \frac{45}{256}\left(\frac{r}{-}\right)^4 \quad \frac{1}{16}\left(\frac{r}{-}\right)^5\right\} \qquad \text{Eq. 3-10}$$

$$D_{\perp} = D_0\left\{1 \quad \frac{9}{8}\frac{r}{-} + \frac{1}{2}\left(\frac{r}{-}\right)^3 \quad \frac{57}{100}\left(\frac{r}{-}\right)^4 + \frac{1}{5}\left(\frac{r}{-}\right)^5 + \frac{7}{200}\left(\frac{r}{-}\right)^{11} \quad \frac{1}{25}\left(\frac{r}{-}\right)^{12}\right\} \qquad \text{Eq. 3-11}$$

There is currently no comprehensive model to accurately describe the evolution of the diffusion coefficient with respect to attractive (biochemical) interactions. Literature suggests an exponential decay of the diffusion coefficient with $D \propto D_0 e^{-N}$, were N denotes the overall interaction strength [164].

3.4.1 Viscosity of PBS containing 1% BSA

Eq. 3-9 states that the diffusion coefficient of a probe depends on η, the dynamic viscosity of the solution in which the probe is immersed. I therefore determined η for the buffer solution used in PFM experiments (PBS pH 7.2 containing 1% w/v BSA) using a viscometer (Anton Paar AMVn). At 22 °C, η = ~1.018 ± 0.007 cP. Error is given as ± SD.

3.4.2 *In situ* analysis of cNup153-functionalized surfaces and Kap-probes

To clarify if probe functionalization and biochemical activity as described in section 3.2 and 3.3 was preserved in an assembled sample chamber, I performed indirect immunofluorescence *in situ* on the probes and coverslips, respectively.

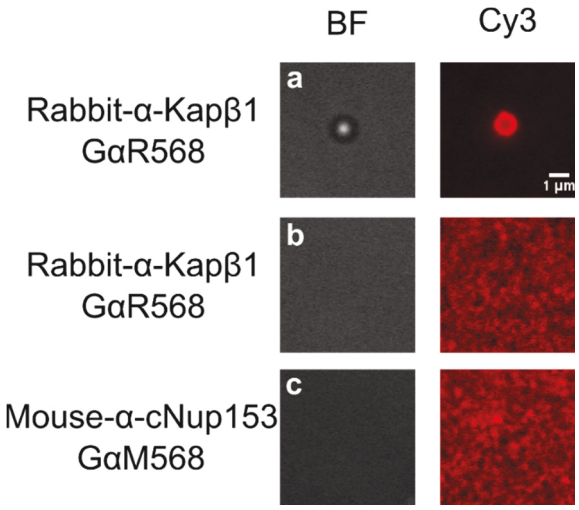

Figure 3-13 – Kap-probe activity *in situ*. Fluorescence microscopy and indirect immunofluorescence on sample chambers disassembled directly after PFM measurements revealed the *in-situ* presence of Kapβ1 (**a**, **b**) and cNup153 (**c**) on the probe and surface, respectively.

Directly after a PFM experiment, the sample chamber was disassembled & washed in PBS pH 7.2. The coverslip including bound Kap-probes were stained for Kapβ1 on probe and surface, respectively (Figure 3-13a & b). A similarly prepared chamber was stained for the presence of cNup153 on the coverslips surface (c). Indirect immunofluorescence and imaging was performed as described in 3.2.2.

Chapter 4

4 Local Kap-probe mobility on FG domain layers

After PFM setup, successful probe generation and surface functionalization, I performed PFM measurements to evaluate Kap-probe behavior on a layer of FG domains. In this chaper I describe how the PFM experiments were carried out and present the obtained results.

4.1 PFM experiment

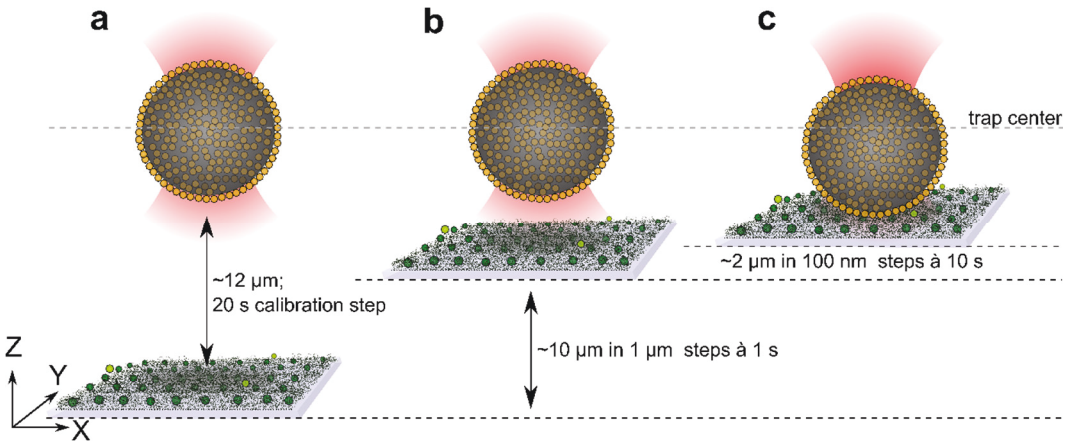

Figure 4-1 – Schematic of a PFM experiment. After a calibration-step 12 µm above the surface (**a**), the cNup153-functionalized slide is approached stepwise towards the probe until contact (**b**). In the vicinity of the surface, the probe experiences attractive force resulting from interactions between Kapβ1 and cNup153, resulting in the probes vertical displacement from the traps center towards the surface (i.e. "jump into contact", see Figure 4-3b and Table 4-1) (**c**). Probe-bound Kapβ1 is colored in orange while cNup153- bound and free floating Kapβ1 is green.

Contents of the sample chamber were replaced with 30 µl of probe solution (at 0.001% solids). The chamber was closed with nail polish that was briefly dried before being mounted upside down into the PFM. Figure 4-1 illustrates how a PFM experiment is performed. Approach measurements were performed with custom-made software using the following protocol: probes were trapped approximately 12 µm above the surface and their position fluctuation recorded for 20 s. The surface was then subsequently approached in 10 steps of 1 µm in 1 s intervals, followed by one step of 0.5 µm. After 10 s of data acquisition, the surface was further approach in 0.1 µm steps until contact. Between each 0.1 µm step, the probes position fluctuations were recorded for 10 s. Data acquisition was performed at 0.5 MHz sampling rate (2 µs per frame) with an average trap stiffness k_X: 4.3 $x10^{-6}$, k_Y: 3.5 $x10^{-6}$, k_Z: 1.1 $x10^{-6}$ N/m (Figure 4-2). I chose the trap to be as weak as possible while still enabling comfortable probe handling. Measurements started routinely ≥ 10 minutes after addition of the probe solution to the sample chamber. Measurements were performed with > 10 different probe at T=22 °C per condition. One dimensional diffusion coefficients of individual probes in contact with the cNup153 layer were calculated as described in 3.2 and normalized to their corresponding bulk diffusion coefficients.

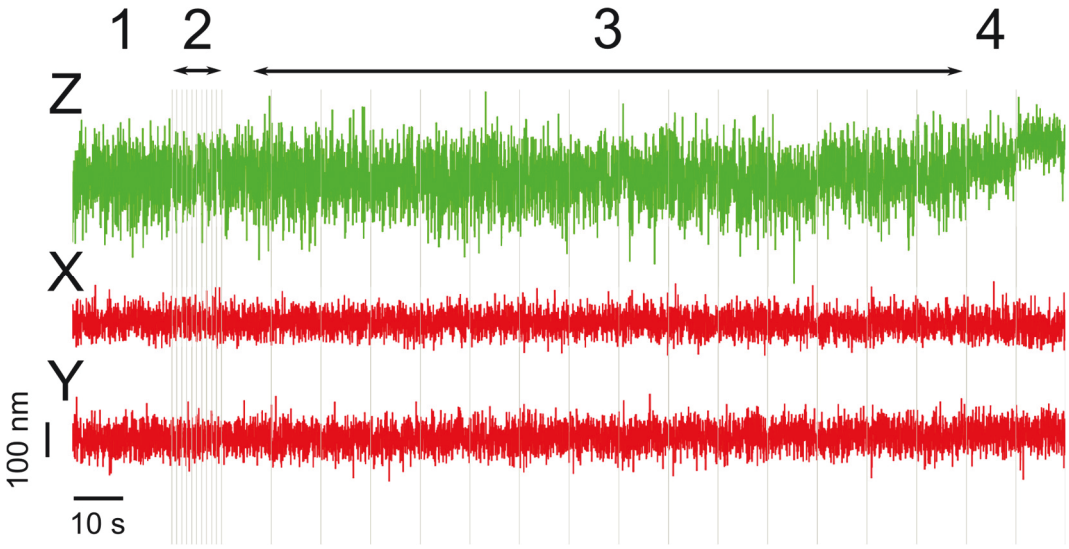

Figure 4-2 – pHis-probe (i.e., probes without Kapβ1) approached by a cNup153 functionalized surface. (1) The probes positional fluctuations are recorded in bulk solution for 20 s. (2) The surface is approached in 10 step à 1 s each. (3) The surface is further approach in steps à 0.1 µm and data is recorded for 10 s following each step until contact (4). The pHis-probe experiences no attractive forces towards the cNup153 layer and is instead push away from the traps center by subsequent ramping steps. Data acquisition was performed at 0.5 MHz sampling rate.

4.2 2D histograms

As introduced in section 3.4, energy landscapes of the probe inside the optical trap can be calculated based on their position histograms (in two dimension, Figure 3-11)

To correct for systematic errors in the XY plane, each in-contact (XY) histogram was decorrelate with respect to a corresponding reference measurement on the same probe in bulk solution ~12 µm away from the surface. To do so, 2D reference data was rotated in space until the off-diagonal elements of the covariance matrix were 0. The as-obtained rotation matrix was then applied to the in-contact data.

The resulting probability histogram can be converted into a free energy landscape using Boltzmann statistics as described in chapter 3.2, Eq. 3-3.

More specifically, maps of the energy landscape were plotted in discrete levels E_i using

$$E_i/k_B T = \quad l\,n(p_i) \qquad \text{Eq. 4-1}$$

where $p_i = N_i/N$ corresponds to the occupancy of level i calculated from the number of data points N_i in level i relative to the total amount of data points N. From the difference in trap stiffness, $k_x > k_y$ follows an elliptical shape of the maps as a consequence of the equipartition-theorem (see chapter 3.2, Eq. 3-5).

4.3 PFM measurements of local Kap-probe mobility

My minimal NPC-inspired system (Figure 4-3a) consists of a surface-tethered FG Nup brush layer of Nup153 (aa 874-1475; 28 FG repeats; modified with 3 N-terminal cysteines; henceforth cNup153 [57]) that is approached towards a weak optically-trapped 1 μm-diameter Kapβ1-functionalized colloidal probe (i.e., Kap-probe) by a piezo-actuator (Z) built within a photonic force microscope [140] (chapter 3). Specifically, the PFM allows for the Brownian motion of the Kap-probe to be recorded in three dimensions with nanometer and microsecond spatiotemporal resolution between successive 100 nm steps. The PFM experiments were conducted in: 0.5, 2, 5, 10 and 30 μM Kapβ1 solutions (i.e., from low to physiological [103] concentrations) to assess the impact of soluble Kapβ1 as a control parameter of Kap-probe mobility, and in bacterial cell lysate (with 0.5 μM Kapβ1) to test for corresponding effects in a more complex physiological environment. Further, because penta-His antibodies (pHis) were used to link Kapβ1 to the Kap-probe (section 3.2.1), I

employed pHis-functionalized probes (without Kapβ1; henceforth denoted as pHis-probes) as a non-FG Nup binding control.

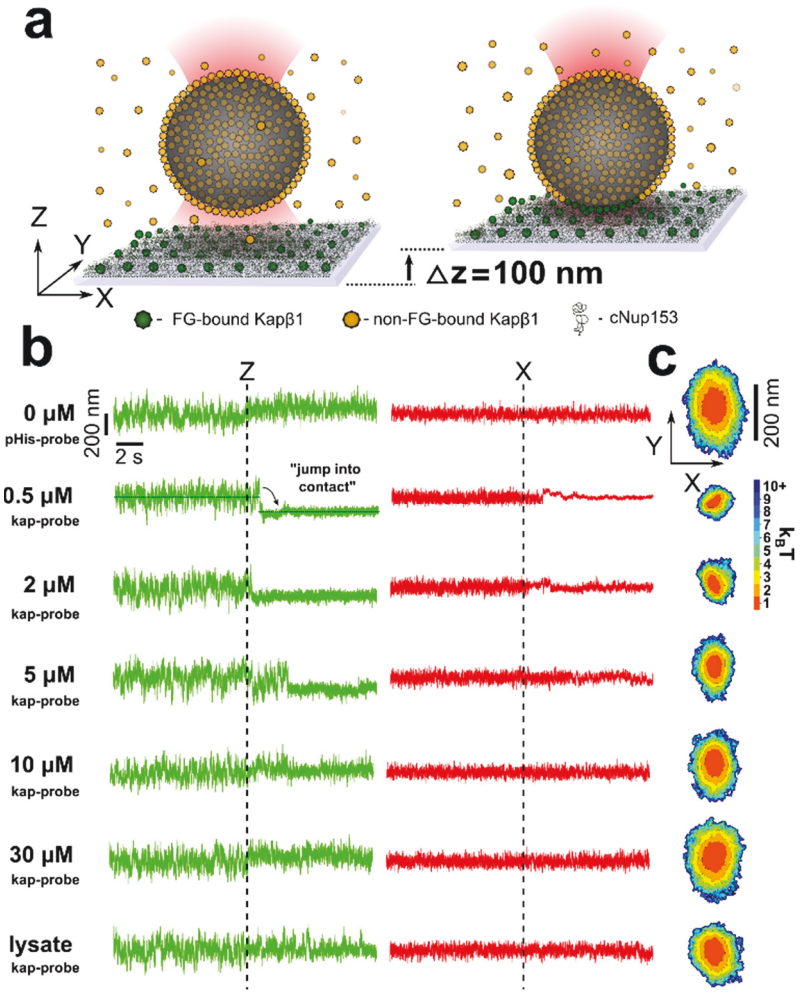

Figure 4-3 – Influence of Kapβ1 concentration on Kap-probe binding and mobility. (a) A cNup153 layer is driven at 100 nm steps towards a Kap-probe (gray). Yellow - non-FG repeat bound Kapβ1 molecules. Dark green - FG repeat bound Kapβ1 molecules. (b) Raw PFM position fluctuations obtained in the Z and X directions illustrate respective probe behavior in the step before and after contact (dashed line) with the cNup153 layer. In Z, attractive "jump-into-contact" forces are observed for Kap-probes in 0.5 μM Kapβ1 and gradually weaken with rising Kapβ1 concentration where binding in 30 μM Kapβ1 is barely distinguishable from the pHis-probe (i.e., non-binding). This is most apparent in the lack of amplitude reduction in the Z and X position fluctuations after probe-cNup153 contact. (c) The 2D free energy (XY) landscapes allow quantitative comparisons between the interactions of each probe with the cNup153 layer. The color scale represents the energy levels of each probe with respect to its lateral equilibrium position (i.e., energy minimum, red).

Figure 4-3b shows the positional fluctuations obtained before and after each respective probe encounters the underlying cNup153 layer. No discernable changes are detected with the pHis-probe except for a slight increase in the Z-axial position that coincides with a 100 nm-step that drives the two surfaces into contact. This verifies that pHis does not exert any measurable interaction with cNup153. In contrast, between 0.5 and 5 μM Kapβ1, the Kap-probe exhibits a "jump-into-contact" (similar to AFM [165]) due to attractive biochemical forces in the immediate vicinity of the cNup153 layer. This indicates that the Kap-probe is now bound via Kap-FG interactions, with an interaction force gradient larger than the trapping stiffness k_Z [166]. This allows us to calculate the attractive force at different background concentrations of Kapβ1 using Hooke's law ($F = k z$) as summarized in Table 4-1. The substantial amplitude reduction that follows in the X and Z directions (Y was found to be similar to X) is further indicative of Kap-probe binding. Subsequent Z analysis reveals that both the attractive interaction force and the adhesion or "rupture" force required for separating the Kap-probe from the cNup153 layer decreases with increasing Kapβ1 concentration (Figure 4-4).

Table 4-1 – Attractive "jump-into-contact" forces at different concentrations of Kapβ1. Values are given in pN together with their standard deviation (SD) and standard error of the mean (SEM), respectively. Negligible attraction was detected between a pHis-probe and the cNup153 layer.

	<F [pN]>	**SD**	**SEM**
0.5 μM	-0.126	0.047	0.011
2 μM	-0.121	0.049	0.012
5 μM	-0.071	0.061	0.011

10 µM	-0.070	0.030	0.005
30 µM	-0.030	0.043	0.013
Lysate	-0.085	0.056	0.014

This weakening represents initial evidence that the number of available FG repeats is decreasing as Kapβ1 occupancy increases within the cNup153 layer [104]. At 30 µM Kapβ1, the positional fluctuations of the Kap-probe are barely distinguishable from the inert pHis-probe interaction. To obtain a quantitative measure of these effects, I apply Boltzmann statistics to compute the influence of Kapβ1 concentration on the in-plane free energy landscape of each probe using the positional probability of its lateral fluctuations (Figure 4-3c; section 4.2). Here, the quasi-symmetric flattening of the energy landscape highlights the gradual transition from strong to weak in-plane interactions (i.e., from 0.5 µM to 30 µM), which approaches non-specific pHis-probe behavior. Interestingly, a similar effect was observed in an independent study [167]. The energy landscape obtained in cell lysate indicates that the presence of non-specific interactions (section 2.4) interferes only marginally with Kap-probe binding (i.e., compare with 10 µM Kapβ1).

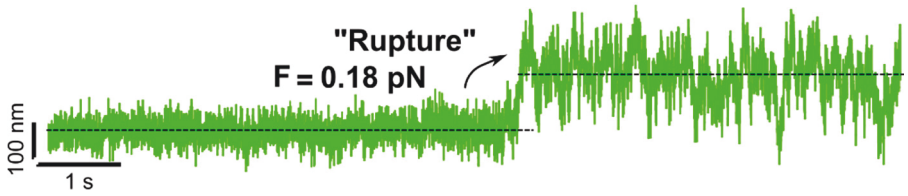

Figure 4-4 – Example rupture event of a Kap-probe from a cNup153-layer at 5 µM Kapβ1 background concentration. Kap-probes bound to the cNup153-layer were displaced vertically by ramping the piezo downwards in 100 nm steps (i.e., away from the trap center) with an average trapping stiffness $k_z = 1.1\,\mu N/m$ until the signal reached the physical limits of the detector. Therefore, the smallest detectable rupture or adhesion force is $F_{min} = 0.11\,pN$. For instance, Kap-probes in 30 µM Kapβ1 and pHis-probes exhibited rupture forces that exist below F_{min} (i.e., adhesion was so weak that the probes remained in

the trap center). At the other extreme, no rupture events were observed in 0.5 & 2 µM Kapβ1 over the measurement time because the probes remained firmly attached to the cNup153-layer, i.e. the corresponding adhesion force exceeded the upper force limit. Rupture events where only measured at 5 & 10 µM with an average force of 0.172 ± 0.06 pN after an average of 2.621 ± 2.353 s. The error is given as SD.

Individual Kap-probe behavior can be further ascertained by computing the MSD from their position fluctuations to derive the respective diffusion coefficient (D) in each dimension. For free diffusion, the MSD is linear with time for X and Z in the aforementioned conditions (Figure 4-5a and b; section 3.4). Linear MSD fits provide D_X and D_Z to which I normalize by D_0 (≈ 0.46 $\mu m^2/s$), the in-bulk diffusion coefficient that was measured for each respective probe. Here, D_0 compares favorably with the Stokes-Einstein equation ($D = k_B T/6\pi\eta R$ where k_B is Boltzmann's constant, T is temperature, η is the viscosity and R is the probe radius), which gives 0.45 $\mu m^2/s$ for a similar sized particle where T is 295.15 K and η is 1.018 cP (section 3.4.1). As shown in Figure 4-5c and d, the non-binding pHis-probe is the most diffusive, while the Kap-probe is the least diffusive in 0.5 µM Kapβ1. Increasing Kapβ1 concentration evokes qualitative increases to $D_X/D_{0,X}$ and $D_Z/D_{0,Z}$, although $D_Z/D_{0,Z}$ is quantitatively less because of the presence of an underlying surface boundary (i.e., Brenner's Law [161]). Again, Kap-probe diffusion approaches pHis-probe behavior at 30 µM Kapβ1. I interpret this to stem from diminishing multivalent interactions between the Kap-probe and the cNup153 layer. This is consistent with SPR measurements, which show that a reduction of free FG repeat binding sites follows from a concentration-dependent increase in the occupancy of soluble Kapβ1 molecules within the cNup153 layer [104] (section 2.3). Likewise, Kap-probe diffusion in cell lysate is remarkably similar to 5-10 µM Kapβ1, which indicates that Kap-probe

binding to cNup153 prevails in spite of interference from non-specific proteins (section 2.4). This is in agreement with previous observations, which showed that Kaps bind to FG domains in a complex solution of cell lysate, albeit with reduced affinity [62].

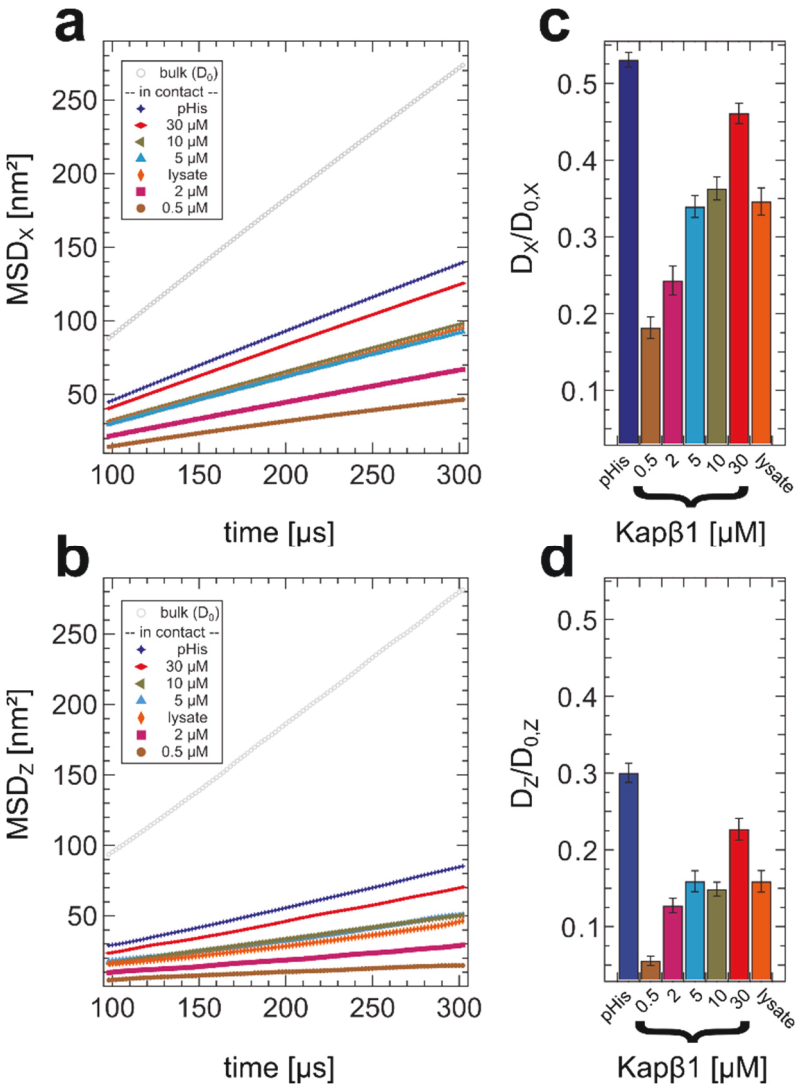

Figure 4-5 – Kap-probe diffusivity at the local probe level upon increasing Kapβ1 concentration. Plots of MSD against time in (**a**) X and (**b**) Z indicate that the probes exhibit free diffusion on cNup153. Bulk-normalized one-dimensional diffusion coefficients in (**c**) X and (**d**) Z as obtained from linear fits to the MSD. With the non-binding pHis-probe being the most diffusive, Kap-probe diffusivity is rectified with increasing Kapβ1 concentration and prevails even when non-specific proteins in the cell lysate are present (see section 2.4). Error bars represent the standard error of the mean.

A summary of the in-contact diffusion coefficients calculated for a 1 µm-diameter probe based on Figure 4-5c and d is given in Table 4-2.

Table 4-2 – Diffusion coefficients for a 1 µm-diameter probe.

	$D_X[\mu m^2/s]$	$D_Z[\mu m^2/s]$
pHis	0.244 ± 0.009	0.138 ± 0.013
0.5 µM	0.084 ± 0.014	0.026 ± 0.006
2 µM	0.112 ± 0.019	0.059 ± 0.009
5 µM	0.156 ± 0.014	0.073 ± 0.014
10 µM	0.167 ± 0.015	0.068 ± 0.009
30 µM	0.212 ± 0.013	0.104 ± 0.014
lysate	0.159 ± 0.018	0.073 ± 0.014

4.4 Discussion

The energy landscapes in Figure 4-3c show a gradual flattening at elevated Kap concentrations, which I attribute to weakened interactions between the Kap-probe and the surface. This is reflected by decreasing attractive forces between Kap-probe and surface with increasing Kapβ1 levels (Figure 4-3b and Table 4-1). At intermediate Kap concentrations (5-10 µM), I observed apparent rupture events with forces in the fN range (Figure 4-4). In contrast, AFM measurements revealed Kapβ1-FG domain rupture forces on the order of 10 pN [168]. Therefore, it is unlikely that these events represent classical rupture forces. Rather, my observations reflect an increased probability of Kap-probe unbinding from the layer at higher Kap concentrations during the observation time (i.e., ”off-rate”).

When analyzing Kap-probe MSDs, I find the reduced lateral diffusion coefficient of the pHis-probe in contact with the surface to be ~1/2 of its bulk value (Figure 4-5c). This agrees well with Eq. 3-10 and previous studies of non-interacting colloidal particles diffusing in close proximity to a surface [169], [170].

When following Kap-binding quantum dots (QD) traversing NPCs in permeabilized cells, Lowe *et al.* found their motion to be dominated by anomalous diffusion (i.e. subdiffusion) after a few seconds of observation [119]. Unlike typical diffusion, subdiffusion is described by a power law, $MSD \propto D_\alpha t^\alpha$, with $\alpha < 1$. In contrast, $\alpha = 1$ for normal diffusion (i.e. Eq. 3-6). The authors attribute this to crowding conditions and confinement inside the NPC, reminiscent of the "trap" in PFM. As illustrated in Figure 3-12 and supporting reference [171], probe diffusivity in a confined environment is sensitive to the timescale analyzed. Therefore, QD behavior remains less clear on the ms timescale relevant to NCT of Kaps *in vivo* [11], which was not accessible to the setup in Lowe *et al.* with 25 ms frame rate [119].

Figure 4-5 shows that Kap-probes undergo normal diffusion on FG domains on a sub-ms timescale. Nevertheless, while Kap-FG interactions reduced the probes diffusion coefficient *per se*, this is rectified at increasing Kap concentrations. I observed analogous rectifying behavior in bacterial cell lysate (Figure 4-5), which binds nonspecifically to FG domains (section 2.4) and interferes with Kap-FG binding [62]. This implies a role for nonspecific protein interactions during NCT in cells.

Overall, my results show how local probe mobility is influenced by changes in the background concentration of Kaps. Based on SPR measurements, I attribute this effect to result from increasing Kap occupancy within the FG domain layer (section 2.3) [102], [104]. Recent publications show that this

scenario is accompanied by a kinetic “fast phase” that is characterized by elevated on- and off-rates that result in lower affinity [102], [104].

My work complements these results and shows that this decreased affinity leads to enhanced mobility on top of FG domain layers.

Chapter 5

5 Two dimensional diffusion regulated by Kapβ1 concentration

Next, I wanted to verify if the result on probe-diffusivity obtained by PFM could influence the balance between Kap-probe selectivity and mobility, thereby leading to a two-dimensional random walk. For this, I switched off the optical trap and recorded videos of Kap-probes moving in relation to the cNup153 layer over several minutes. Ensemble-level Kap-probe behavior was then analyzed using a custom tracking algorithm [172] (section 5.1-5.3) to extract the steady-state probe height (Z) probability distribution and its lateral diffusion coefficients.

Colloidal tracking by optical means has traditionally been utilized to non-intrusively study interactions in biological systems, including both specific [167], [173] and non-specific interactions [169] of directed [174], [175] and random [167], [169] colloidal motion on protein-functionalized surfaces. As the motion of small nm-µm sized colloids in a liquid environment is governed by energies on the order of $k_B T$, this approach is ideally suited to get insights into interactions between proteins, whose reactions are generally governed by energies on the same scale [176]. For example, analysis by video microscopy of individual as well as ensembles of colloidal particles has been used to characterize antibody-antigen interactions [177], RNA polymerase activity

[178], or kinesin- and myosin-driven movements on microtubules and actin cables, respectively [174], [175]. Other studies include protein-carbohydrate [167] and protein-polymer [169] interactions.

5.1 Ensemble Probe Tracking without the PFM

Measurements were performed at T=22 °C using probes at ~0.007% solids and sample chambers that were prepared similarly to a PFM experiment but using the visible light path. Videos were taken between 2 h - 5 h after probes were injected into the sample chamber based on the known probe settling velocity of 2.65 x 10^{-6} cm/s (i.e., supplier value). This ensures that each probe has enough time to travel a maximum distance of 100 μm (i.e., chamber height) to reach the cNup153 layer on the bottom surface.

Automated 3D particle tracking was realized using a custom-written algorithm in LabVIEW. It allows tracking of probes with 900 nm diameter within an axial range up to 1.2 μm above the glass surface with lateral and axial accuracies of 60 nm and 100 nm, respectively. Probes that were between 1.2 μm and 1.4 μm above the surface could also be tracked albeit with lower accuracy before falling out of range. Diffusion coefficients, average interaction times and the probability distribution of the height above the surface was extracted from the obtained particle trajectories. It is noteworthy that the interaction times are not dominated by the gravitational pull F_g on the probe as this is balanced by the buoyancy force F_B of the surrounding fluid

$$F_g \quad F_B = V_{bead} \quad g(\rho_{bead} \quad \rho_{fluid}) \qquad \text{Eq. 5-1}$$

which results in a negligible net-force of ~2.2 x 10^{-16} N acting on a probe with density $\rho_{bead} = 1.06\,\mathrm{g/cm^3}$ and volume V_{bead} with radius $r_{bead} = 450\,nm$ in a fluid of density $\rho_{fluid} = 1\,\mathrm{g/cm^3}$ at T= 22 °C.

5.2 Tracking algorithm

2D tracking in the XY-plane is based on the cross-correlation and centroid method which is widely employed for particle tracking with different microscopy techniques [179]. The Z-position is determined by comparing moments of the light intensity distribution around the particle center to calibration measurements performed with the help of a piezo stage as first proposed by Crocker and Grier [180].

This algorithm gives the 3D trajectories $\bar{r}(t) = \left(r_x(t), r_y(t), r_z(t)\right);\ (t = n\tau; n = 0,1,\dots,N)$ (3412 trajectories in the case of 30 μM competing Kapβ1 in solution, 160 for 1 μM and 950 for the pHis-probes). Here τ denotes the time between successive video frames (in my case 67 ms) and (N+1) is the number of recorded positions for the trajectory.

5.3 Ensemble-analysis of the diffusive motion

Given the recorded 3D trajectories $\bar{r}(t)$, the time-dependent mean squared displacements $MSD(t)$ in all three dimensions for each trajectory were calculated similar to Eq. 3-7 [181]. In the case of free diffusion the *MSD* increases linearly with time. Accounting for systematic error contributions originating from finite image acquisition time (characterized by the shutter

time τ) and limited tracking accuracy (characterized by variances σ^2 on static position measurements [182]), the relationship can be written as

$$MSD\ (t) = 2Dt + \left\{2\sigma^2 \quad \frac{2}{3}D\tau\right\} \qquad \text{Eq. 5-2}$$

The diffusion coefficient D and localization error σ in each dimension (X,Y,Z) can then be obtained for every trajectory most accurately from a linear fit to a subset of the $MSD(t)$ curves [183]. Averaging these values over all trajectories gives the ensemble averaged diffusion coefficients and localization errors.

The interaction time for each trajectory was calculated as follows:

$$t_{life} = (N + 1)\tau \qquad \text{Eq. 5-3}$$

Further, the height-distribution of the particles was determined by binning the Z-positions and assigning every observed particle position to the corresponding bin (Figure 5-1). Interaction times and diffusion coefficients can be height-resolved by decomposing the initial trajectories into subsets that lie entirely in a single Z-position bin and then evaluating the quantities for these subsets in the same way as described above. Trajectories were split once they left a Z-position bin for more than 1 frame.

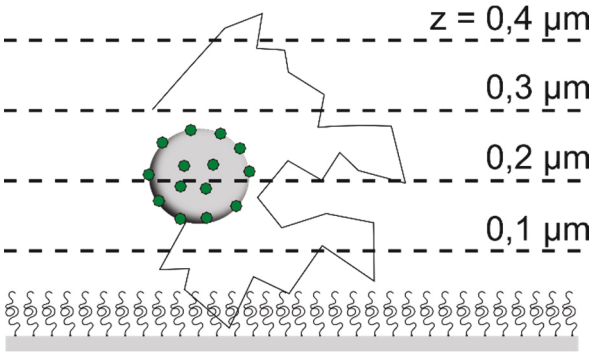

Figure 5-1 – Schematic of height-resolved particle tracking by video microscopy.

5.4 Collective behavior of Kap-probes relative to a cNup153 layer

Representative probes provide direct visual proof of the effects observed by PFM trajectories (see supplemental movies). As expected, pHis-probes that lack FG-binding transiently impinge on the surface and diffuse away (Figure 5-2a). At the other extreme, the Kap-probes become "stuck" with minimal movement in 1 μM Kapβ1 indicating maximal binding with cNup153 (Figure 5-2b). Quite remarkably, I observe that reduction of dimensionality is achieved at 30 μM Kapβ1, where the Kap-probes exhibit a distinctive two-dimensional random walk on the cNup153 layer (Figure 5-2d and Figure 5-3).

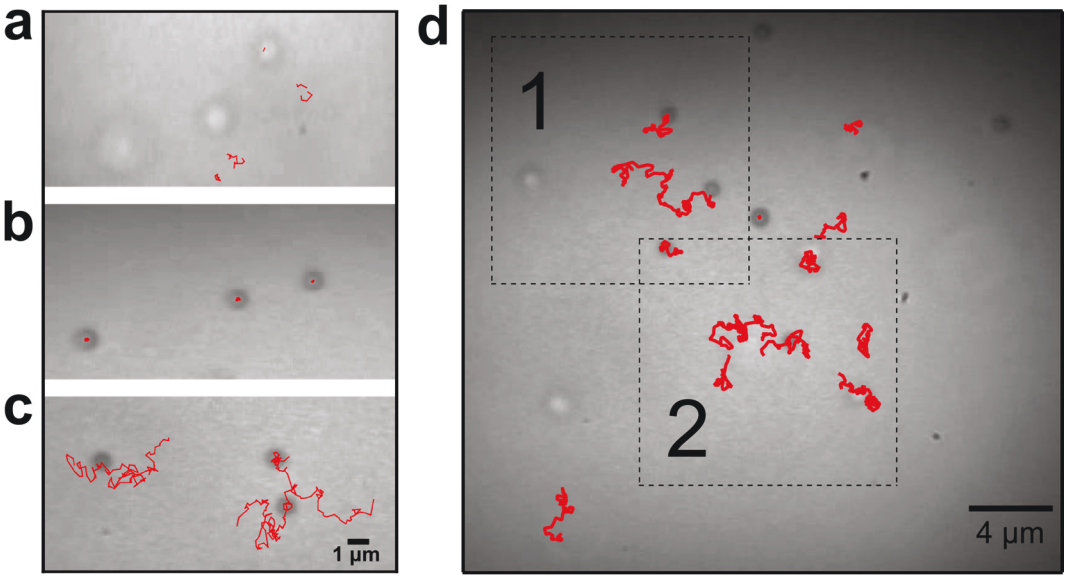

Figure 5-2 – Reduction of dimensionality by the "*dirty velcro effect*". Superimposed trajectories for (**a**) pHis-probe, (**b**) Kap-probe in 1 μM Kapβ1, and (**c**) Kap-probe in 30 μM Kapβ1 in the vicinity of the surface. **d**, A superimposition of the probe-surface contacts shows a distinct two-dimensional random walk in 30 μM Kapβ1 (see Supplementary Movies). All movies were recorded and saved at 15 fps.

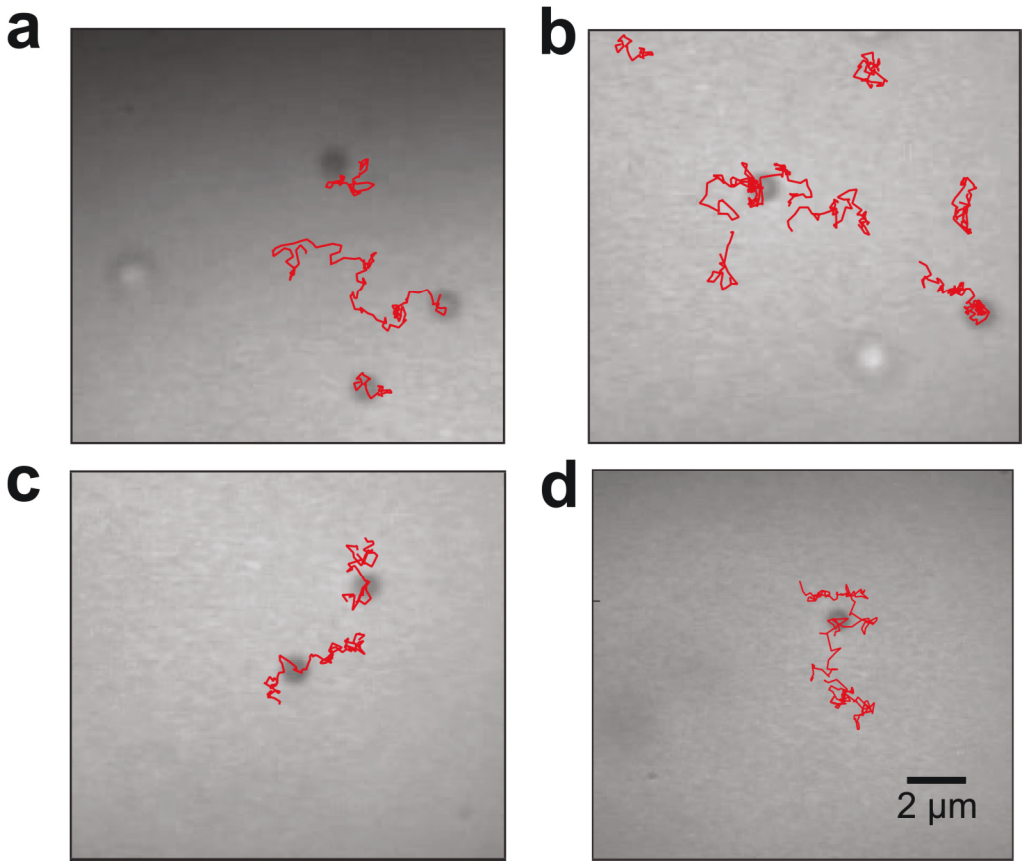

Figure 5-3 – Reduction of dimensionality by the "*dirty velcro effect*" (continued). Trajectories were obtained at 30 μM Kapβ1. **a**,**b** represent zoom-ins corresponding to region 1 and 2 in Figure 5-2d, respectively, while trajectories in (**c**) and (**d**), were recorded independently. All movies were recorded and saved at 15 fps.

Complete statistical analysis of obtained trajectories presented in Figure 5-4a shows that ~100% of the Kap-probes are located in the immediate vicinity of the cNup153 layer ($Z < 0.2$ μm) in 1 μM Kapβ1 with 70% being in direct contact. In 30 μM Kapβ1, the population of Kap-probes that contact the layer is reduced to 25%. The lateral diffusion coefficients (D_{XY}; $Z = 0.1$ μm) as calculated from the linear MSD_{XY} plots in Figure 5-4b are 0.004 ± 0.001 and 0.217 ± 0.009 $\mu m^2/s$ for the Kap-probe in 1 μM and 30 μM Kapβ1, respectively. It is noteworthy that the latter ensemble averaged D_{XY} agrees with the PFM local-probe value ($D_x = 0.212 \pm 0.013$ um^2/s; Figure 4-5c and

Table 4-2). This proves that Kap-probe behavior is diffusive and scales linearly over six orders of magnitude from μs to s timescales. In comparison, the pHis-probe interaction is unmistakably non-selective based on its negligible population ($< 1\%$) at the surface, which are far too infrequent to provide any measurable MSD.

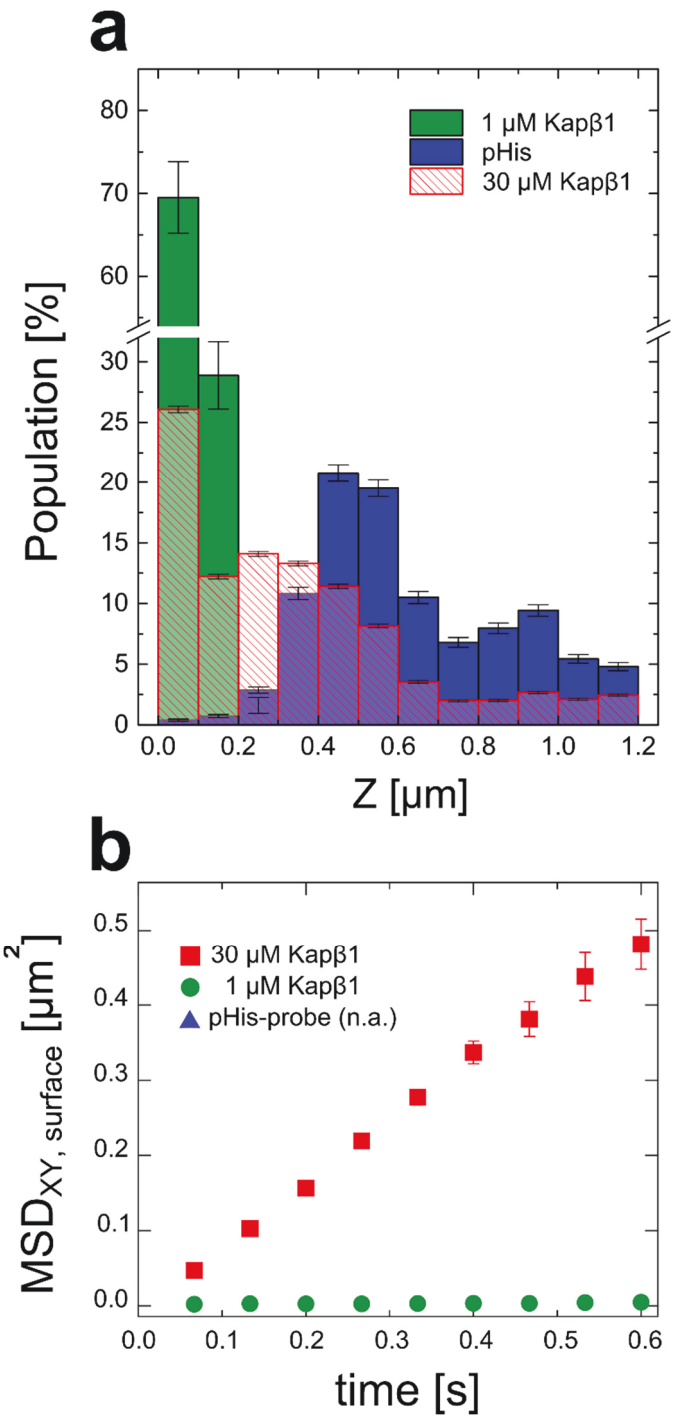

Figure 5-4 – Effect of Kapβ1 concentration on ensemble Kap-probe steady-state probability distribution and lateral diffusivity. (**a**) Kap-probe probability distribution as a function of (Z) height. The pHis-probe is unmistakably non-selective while the Kap-probe is the most strongly selective in 1 μM Kapβ1. Selectivity is preserved but reduced at 30 μM Kapβ1 concentration. Error bars represent the standard error of the mean. (**b**) The slope in the ensemble-level MSD corresponds to $D_{XY} = 0.217 \pm 0.009$ μm²/s in 30 μM Kapβ1. Diffusion is negligible in 1 μM Kapβ1 because the Kap-probes adhere to the surface over the experimental duration. Note that the analysis is not applicable to pHis-probes given their

extremely low occupancy and transient behavior on the cNup153 surface. Error bars represent the standard error of the mean.

In terms of their average (Z) interaction times (Figure 5-5 and Methods 5.1-5.3), Kap-probes are permanently immobilized (i.e., longer than the observation time) on the surface in 1 μM Kapβ1. However, this reduces to 0.5 s in 30 μM Kapβ1, which suggests that their long-lived trajectories (e.g., 8 s) involve various colloidal diffusion mechanisms [76] (e.g., hopping, sliding, rolling, etc.) in the immediate vicinity of the surface.

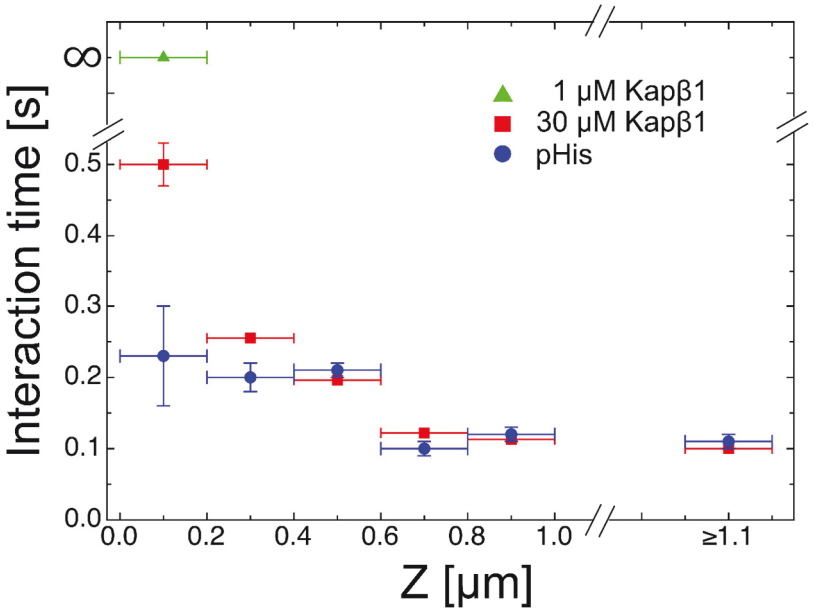

Figure 5-5 – Average probe interaction time as a function of (Z) height. Selectivity is preserved with increasing Kapβ1 concentration (30 μM) in spite of a reduction in the average Kap-probe interaction time on cNup153. Whereas Kap-probe interaction lifetime is infinite in 1 μM Kapβ1 (i.e., they adhere permanently within the observation time), this reduces to 0.5 s in 30 μM Kapβ1 and is shortest for the unspecific pHis-probe. Error bars represent the standard error of the mean.

As postulated by Adam and Delbrück [1], my work demonstrates how multivalent interactions can be modulated to exert sufficient strength to maintain selectivity but yet are weak enough to permit delocalized two-

dimensional diffusion. In Figure 5-6 I consider the Kap-probe and cNup153 layer as opposing surfaces of molecular "velcro", respectively. When the concentration of soluble Kapβ1 is low (i.e., 1 μM), the Kap-probes are immobile on the cNup153 layer because of maximal binding avidity with largely unoccupied FG repeats. An interesting observation is that this leads to the near 100% population of Kap-probes on the surface thereby suggesting possible superselectivity [74]. In contrast, 25% of Kap-probes exhibit two-dimensional diffusion in 30 μM Kapβ1 solution due to limited access to FG repeats on a cNup153 layer pre-occupied with soluble Kapβ1. Overall, the weakened binding is reminiscent of a "*dirty velcro effect*", where in physical terms Kap-probe adhesion and protein friction [184] with the FG Nup layer is significantly reduced. A further ramification is that Kap-probes would exhibit non-binding behavior (e.g., pHis-probe) under conditions that saturate the cNup153 layer with soluble Kapβ1 or other non-specific binders.

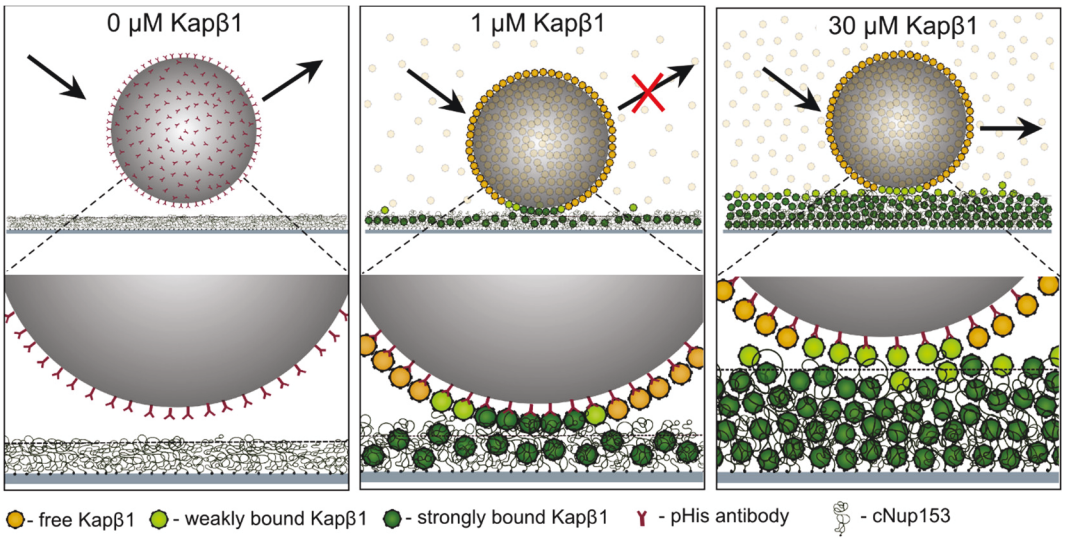

Figure 5-6 – Model of various probe interactions with respect to the cNup153 molecular environment (not drawn to scale). (left) A pHis-probe lacks FG-binding and diffuses away from the surface. (middle) Binding of the Kap-probe to an excess of FG repeats in the cNup153 layer at 1 μM Kapβ1 leads to sticking. (right) At 30 μM Kapβ1, the Kap-probe is held to the surface by a reduced number of Kap-

FG interactions due to a pre-occupation of the cNup153 layer by large numbers of free Kapβ1 molecules (i.e., "dirty velcro"). In this state, the cNup153 layer is strong enough to maintain binding but sufficiently weak to permit diffusion along the interface.

Taken together, these differences in probability distribution and diffusivity define the inverse correlation between selectivity and the microscopic mobility of each Kap-probe as controlled by the soluble Kapβ1 concentration (Figure 5-7).

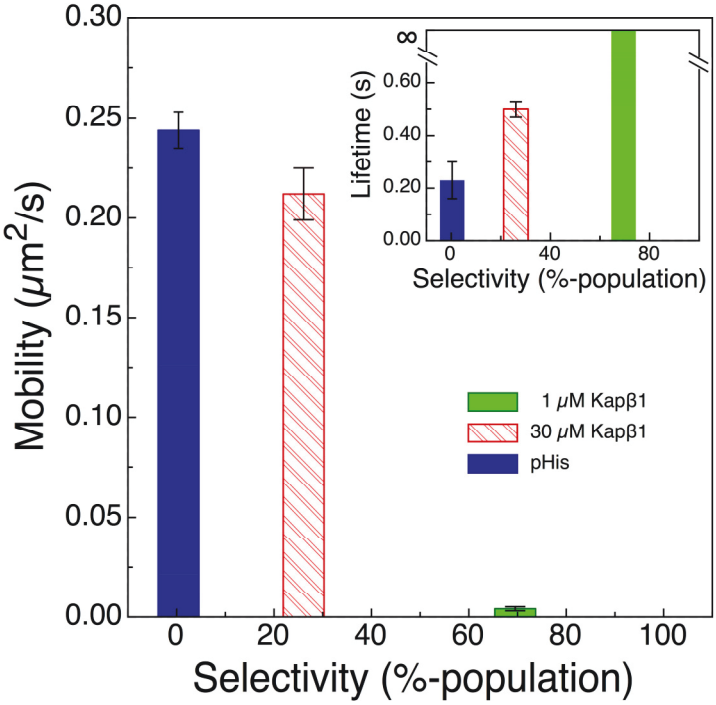

Figure 5-7 – Mobility vs Selectivity. Graphical representation of the inverse correlation between the probes diffusion coefficient (i.e. mobility) or interaction times (inset) and their respective population (i.e. selectivity) at the surface (≤ 100 nm) at 0 (pHis, unspecific), 30 µM and 1 µM Kapβ1 in the bulk solution. Error bars represent the standard error of the mean.

Interestingly, this recapitulates the observation that increasing Kapβ1 concentration regulates NPC functionality by increasing import efficiency while reducing interaction time [30]. On a related note, Peters [2] proposed a

ROD-based scenario where Kaps can diffuse in two dimensions (instead of three) along a layer of FG Nups that lines the central pore. Although this has not been confirmed *in vivo*, the physical display of ROD suggests that it can play a functional role in expediting selective transport through the biological NPC, particularly with respect to large cargoes that bind multiple Kaps [185].

5.5 Discussion

In a study comparable to the work presented here, Eichmann *et al.* [167] recorded the trajectories and mean force potentials of concanavalin A (ConA) decorated colloids moving on a dextran-presenting surface in the presence of glucose. High concentrations of glucose, which competes with dextran for ConA binding sites, led to a widening in the energy potential between the dextran surface and colloids due to preoccupied ConA receptors. This is reminiscent of the flattened energy landscapes observed for Kap-probes at increasing concentrations of Kapβ1 (Figure 4-5) and underscores my conclusion that this flattening is due to preoccupied FG domains. In contrast, the experiments by Eichmann *et al.* did not reveal ROD behavior. In the absence of glucose, ConA-colloids adhered firmly to the surface with minimal movement. At elevated glucose levels colloid-surface interaction times were reduced, which lead to their diffusion over the dextran surface. However, trajectories revealed that during their diffusion, colloids where predominantly unbound and "levitated" above the surface in a nonspecific fashion.

Further discrepancies stem from size (d ~2.34 µm) and material of the colloids used (i.e. silica) [167]. Based on their higher density ($\rho_{silica} = 2.0\ \mathrm{g/cm^3}$) and radii, ConA-colloids experience an enhanced gravitational pull by more than

2 orders of magnitude as compared to Kap-probes, and are hence biased towards the surface. In contrast, the very light polystyrene-probes used in this work are not pinned to the surface by gravity, which underscores the importance of biochemical interactions between Kaps and FG domains in the observed reduction of dimensionality.

Studies of surface diffusion in different systems have shown that the diffusion coefficient of surface-bound molecules is reduced 2-3 orders of magnitude as compared to bulk diffusion [107], [110]. In contrast, two dimensional Kap-probe diffusion on the FG domain layer is reduced by only ~60%. Overall, my results demonstrate how Kap-FG interactions balance the tradeoff between mobility and specificity, which leads to a reduction of dimensionality in Kapβ1 mediated transport on FG domains.

Chapter 6

6 Conclusions and Outlook

6.1 Conclusions

To conclude, my nuclear pore complex-inspired system shows (i) how Kap concentration regulates the tradeoff between specificity and mobility and (ii) attests to the relevance of reduction of dimensionality in controlling selective two-dimensional transport in an artificial context. Unlike the lateral diffusion of lipid bilayer-bound membrane proteins [186], the transition from bulk to surface diffusion demonstrated here provides a general strategy to regulate the controlled capture, targeting and release of selective cargoes. This complements synthetic strategies using different environmental conditions (e.g., temperature, solvent conditions) to induce motion of nano-objects [187] on polymer brushes, particularly in physiological conditions. Nevertheless, the use of Kapβ1 concentration as a single adjustable control parameter retains physiological aqueous conditions, which is advantageous when implementing ROD-based trafficking of biological cargoes. Still, compared against other multivalent receptor-ligand interactions [76], [167], my system exploits the unique functional advantages of IDPs, which include one-to-many and many-to-one binding that follows from a decoupling of specificity from binding strength (i.e., specificity is achieved by the binding avidity of several low-affinity interactions) [188]. As opposed to monoclonal antibody systems [189],

a single FG Nup can bind several copies of the same Kap (one-to-many) while several FG Nups can bind to the same Kap simultaneously (many-to-one). Moreover, their characteristic binding promiscuity enables the FG Nups to serve as transport hubs for approximately 20 different karyopherins in humans, which shuttle key regulatory proteins into the nucleus (e.g. transcription factors) [26]. Accordingly, reduction of dimensionality-based translocation can be implemented along surface-patterned diffusional guides consisting of different FG Nups for instance, to examine Kap-cargo movement and related transport phenomena *in vitro*. In other respects, this underscores the emergence of IDPs as important biomaterials [56] with innate functional properties that may be beneficial to biosensing and other biotechnological applications.

6.2 Outlook

In this work, I have demonstrated the unique advantages of IDPs in concert with multivalent binding partners by regulating the mobility of specific colloids from highly constrained motion to two-dimensional surface diffusion. As such, the *in-vitro*-control over the dimensionality of diffusional processes combined with a bio-recognition function as presented in this work can be utilized in future molecular devices, for example to speed up search processes on a molecular scale. Since the findings are entirely based on affinities between biomolecules, they can further be exploited as a sorting mechanism for marker-molecules, for instance by using diffusional guides (i.e. patterned surfaces), with potential benefit for analytical and preparative applications (e.g. in a “lab-on-a-chip”- device [190], [191]). In contrast, selective transport in microfluidic devices often requires externally controlled pressure or electric

field-driven flows, as well as elaborately designed pumps, channels and valves [192]. Here, ROD represents an alternative transport mode that relies on facilitated diffusion using thermal energy (k_BT) without any additional energetic demands. A further ramification of my results directly concerns predictions made by the Kap-centric barrier mechanism, as it shows that Kap concentration is indeed directly linked to mobility on FG domains.

6.3 Fabrication of micropatterned surfaces to guide Kap-probe diffusion

As pointed out in section 6.1, future devices can exploit reduced dimensionality in Kap-facilitated diffusive processes when guided along a surface patterned with FG Nups. Towards this goal, I produced micropatterned surfaces repetitively displaying stripes of cNup153 to guide fluorescent Kap-probes. Micropatterning was realized via PDMS masks adherent to thiol-reactive glass coverslips to restrict cNup153 attachment to the desired pattern. Characterization by indirect immunofluorescence microscopy using an anti-Nup153 (QE5) primary and secondary goat-anti-mouse antibody coupled to the Alexa 488 fluorochrome revealed successful attachment of cNup153 in a stripe-like pattern (Figure 6-1a and b). As prove of concept, Kapβ1 functionalized fluorescent probes were specifically targeted to cNup153 presenting stripes while being excluded from the BSA- passivated glass surface (Figure 6-1c). In contrast, no targeting was observed for passivated probes (data not shown). Future experimentation utilizing video

microscopy can provide evidence of probe-transport along the patterned surface.

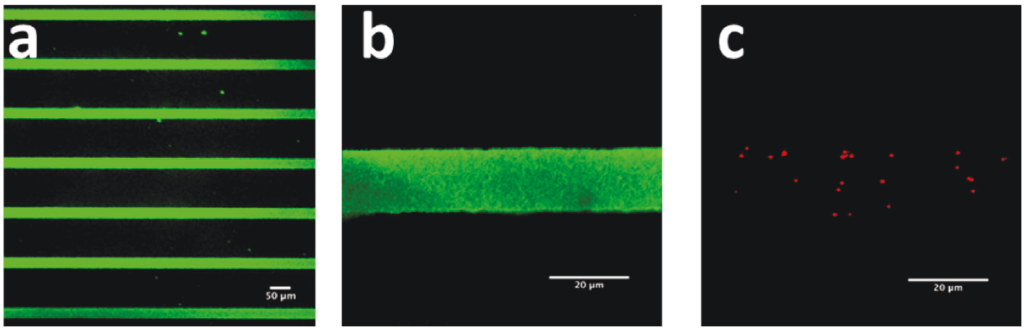

Figure 6-1 – Targeting of fluorescent Kap-probes to cNup153-stripes. (**a**, **b**). Before the immunostaining procedure, fluorescent Kap-probes were added in a background of low (0.5 µM) Kapβ1 concentration and successfully targeted to the cNup153-stripes as their arrangement resembled the underlining stripe-pattern of the cNup153 (**c**). Error bars in (**a**) are 50 µm and 20 µm in (**b**) and (**c**), respectively.

6.4 Towards verifying the Kap-centric barrier mechanism *in vivo*

Besides compelling results obtained *in vitro* suggesting a central role of Kapβ1 in the NPCs barrier mechanism [101], [104], it remains unknown how Kaps might regulate NPC functionality in living cells. Therefore, I seek to ascertain if such a Kap-centric NPC mechanism exists *in vivo*. To this end, I apply fluorescence recovery after photobleaching (FRAP) microscopy on transfected live cells to quantitatively elucidate the transport rates of (i) passive cargoes (i.e., r < 5 nm; EGFP), which traverse NPCs by free diffusion and (ii) signal-specific EGFP-tagged M9 model cargos that are actively shuttled by Kapβ2 (transportin, see Figure 6-2).

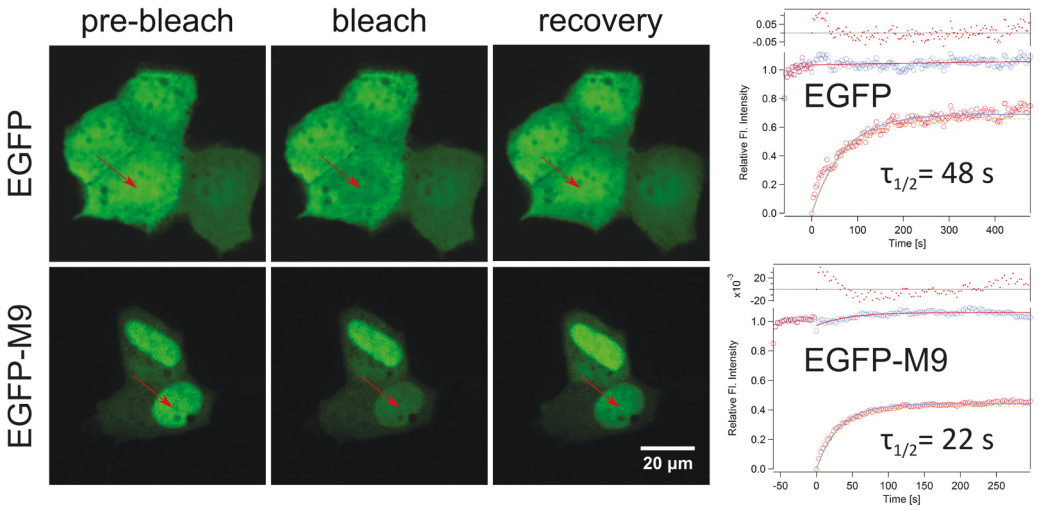

Figure 6-2 – Nucleocytoplasmic transport as revealed by fluorescence recovery after photobleaching. Wt MDCK t23 cells were transfected as indicated. *Left:* Whole nuclei are uniformly bleached (red arrow) and their fluorescence recovery is monitored. Since recovery is only possible by fluorescent molecules entering the nucleus from the cytoplasm via NPCs, this measurement quantifies the molecular flux into the nucleus. Before analysis of the recovery curves, images were corrected for in-plane-drift and cell movements. *Right:* Fluorescence recovery is recorded until steady state is reached. After background subtraction and normalization, recovery curves are fitted with a single-exponential function (red open circles, blue fit). Fits are corrected for global photobleaching and z-drift by the fluorescence of an unbleached reference cell in the same image (blue open circles, red fit). Fits then yield the characteristic time of the recovery process ($\tau_{1/2}$).

Median recovery times were approximately 54 s and 26 s with a nuclear to cytoplasmic fluorescence ratio in equilibrium of about 1.1 and 3.5 for passive (EGFP) and active (EGFP-M9) transport, respectively (see appendix, Figure 10-3). To gain further insights into nucleocytoplasmic shuttling, additional parameters besides the ones collected in FRAP experiments are required (e.g. the nuclear volume). By additionally accessing the number of individual NPCs per cell (& per µm² NE), quantitative statements can be extended to the single NPC level. By utilizing the parameters gained from FRAP and SIM experiments (see appendix Figure 10-1), additional biophysical characteristics of NCT can be calculated using for example the formalism presented in

Bizzarri *et al.* [193]. This yielded a median passive permeability coefficient of the NE (i.e. ~3000 NPCs) of about 10 µm³/s for EGFP. The permeability for actively transport EGFP-M9 was ca. 30 µm³/s, in good agreement with previously published values [193], [194] (see appendix, Figure 10-3). On the single NPC level, these permeabilities translate into $\sim 3.3 \ \frac{10^{-3}\ \mu m^3}{s\ NPC}$ for EGFP and $\sim 10 \ \frac{10^{-3}\ \mu m^3}{s\ NPC}$ for EGFP-M9, which compares well to previous studies (ca. $1.8 \ \frac{10^{-3}\ \mu m^3}{s\ NPC}$ for GFP [195]).

Future experiments may address how NPC permeability is changed depending on Kap-concentration, which can be manipulated in the living cell via gene silencing, conferred ideally via the same vector as used for transient EGFP expression (see appendix, Figure 10-4). In such a construct, the EGFP(-fusion) protein serves as an indicator of positive transfection, silencing RNA expression as well as probe for NCT. I anticipate that changes in molecular flux caused by Kapβ1 silencing compared to a wild-type background will provide insight as to how Kapβ1 regulates NPC barrier functionality.

7 References

[1] G. Adam and M. Delbrueck, "Reduction of dimensionality in biological diffusive processes," in *Structural Chemistry and Molecular Biology*, A. Rich and N. Davidson, Eds. New York: W.H. Freeman and Co., 1968, pp. 198–215.

[2] R. Peters, "Translocation through the nuclear pore complex: selectivity and speed by reduction-of-dimensionality.," *Traffic*, vol. 6, no. 5, pp. 421–7, May 2005.

[3] B. Alberts, A. Johnson, J. Lewis, M. Raff, K. Roberts, and P. Walter, *Molecular Biology of The Cell*, 4th ed. New York, NY, USA: Garland, 2002.

[4] M. Beck, F. Förster, M. Ecke, J. M. Plitzko, F. Melchior, G. Gerisch, W. Baumeister, and O. Medalia, "Nuclear pore complex structure and dynamics revealed by cryoelectron tomography.," *Science*, vol. 306, no. 5700, pp. 1387–90, Nov. 2004.

[5] O. Keminer and R. Peters, "Permeability of single nuclear pores.," *Biophys. J.*, vol. 77, no. 1, pp. 217–28, Jul. 1999.

[6] P. L. Paine, L. C. Moore, and S. B. Horowitz, "Nuclear envelope permeability.," *Nature*, vol. 254, no. 5496, pp. 109–14, Mar. 1975.

[7] M. Mammen, S.-K. Choi, and G. M. Whitesides, "Polyvalent Interactions in Biological Systems: Implications for Design and Use of Multivalent Ligands and Inhibitors," *Angew. Chemie Int. Ed.*, vol. 37, no. 20, pp. 2754–2794, Nov. 1998.

[8] J. Bednenko, G. Cingolani, and L. Gerace, "Importin beta contains a COOH-terminal nucleoporin binding region important for nuclear transport.," *J. Cell Biol.*, vol. 162, no. 3, pp. 391–401, Aug. 2003.

[9] I. Ben-Efraim and L. Gerace, "Gradient of increasing affinity of importin beta for nucleoporins along the pathway of nuclear import.," *J. Cell Biol.*, vol. 152, no. 2, pp. 411–7, Jan. 2001.

[10] K. Lott, A. Bhardwaj, G. Mitrousis, N. Pante, and G. Cingolani, "The Importin beta Binding Domain Modulates the Avidity of Importin beta for the Nuclear Pore Complex," *J. Biol. Chem.*, vol. 285, no. 18, pp. 13769–13780, 2010.

[11] D. Grünwald, R. H. Singer, and M. Rout, "Nuclear export dynamics of RNA-protein complexes.," *Nature*, vol. 475, no. 7356, pp. 333–41, Jul. 2011.

[12] J. Reece, L. Urry, M. Cain, S. Wasserman, P. Minorsky, and R. Jackson, *Campbell Biology (10th Edition)*, 10th ed. Benjamin Cummings, 2013.

[13] C. de Duve, "The origin of eukaryotes: a reappraisal.," *Nat. Rev. Genet.*, vol. 8, no. 5, pp. 395–403, May 2007.

[14] E. Grossman, O. Medalia, and M. Zwerger, "Functional architecture of the nuclear pore complex.," *Annu. Rev. Biophys.*, vol. 41, no. 1, pp. 557–84, Jan. 2012.

[15] K. Ribbeck and D. Görlich, "Kinetic analysis of translocation through nuclear pore complexes.," *EMBO J.*, vol. 20, no. 6, pp. 1320–30, Mar. 2001.

[16] G. Riddick and I. G. Macara, "A systems analysis of importin-{alpha}-{beta} mediated nuclear protein import.," *J. Cell Biol.*, vol. 168, no. 7, pp. 1027–38, Mar. 2005.

[17] N. Panté and M. Kann, "Nuclear pore complex is able to transport macromolecules with diameters of about 39 nm.," *Mol. Biol. Cell*, vol. 13, no. 2, pp. 425–34, Feb. 2002.

[18] J. P. Siebrasse and R. Peters, "Rapid translocation of NTF2 through the nuclear pore of isolated nuclei and nuclear envelopes.," *EMBO Rep.*, vol. 3, no. 9, pp. 887–92, Sep. 2002.

[19] J. M. Cronshaw, A. N. Krutchinsky, W. Zhang, B. T. Chait, and M. J. Matunis, "Proteomic analysis of the mammalian nuclear pore complex.," *J. Cell Biol.*, vol. 158, no. 5, pp. 915–27, Sep. 2002.

[20] D. Stoffler, B. Feja, B. Fahrenkrog, J. Walz, D. Typke, and U. Aebi, "Cryo-electron Tomography Provides Novel Insights into Nuclear Pore Architecture: Implications for Nucleocytoplasmic Transport," *J. Mol. Biol.*, vol. 328, no. 1, pp. 119–130, Apr. 2003.

[21] M. Beck, F. Förster, M. Ecke, J. M. Plitzko, F. Melchior, G. Gerisch, W. Baumeister, and O. Medalia, "Nuclear pore complex structure and dynamics revealed by cryoelectron tomography.," *Science*, vol. 306, no. 5700, pp. 1387–90, Nov. 2004.

[22] M. Beck, V. Lučić, F. Förster, W. Baumeister, and O. Medalia, "Snapshots of nuclear pore complexes in action captured by cryo-electron tomography.," *Nature*, vol. 449, no. 7162, pp. 611–5, Oct. 2007.

[23] N. Elad, T. Maimon, D. Frenkiel-Krispin, R. Y. H. Lim, and O. Medalia, "Structural analysis of the nuclear pore complex by integrated approaches.," *Curr. Opin. Struct. Biol.*, vol. 19, no. 2, pp. 226–32, Apr. 2009.

[24] T. Maimon, N. Elad, I. Dahan, and O. Medalia, "The human nuclear pore complex as revealed by cryo-electron tomography.," *Structure*, vol. 20, no. 6, pp. 998–1006, Jun. 2012.

[25] B. Fahrenkrog and U. Aebi, "The nuclear pore complex: nucleocytoplasmic transport and beyond.," *Nat. Rev. Mol. Cell Biol.*, vol. 4, no. 10, pp. 757–66, Oct. 2003.

[26] Y. M. Chook and K. E. Sueel, "Nuclear import by karyopherin-betas: Recognition and inhibition," *Biochim. Biophys. Acta-Molecular Cell Res.*, vol. 1813, no. 9, pp. 1593–1606, 2011.

[27] M. Fuxreiter, A. Tóth-Petróczy, D. a Kraut, A. T. Matouschek, R. Y. H. Lim, B. Xue, L. Kurgan, and V. N. Uversky, "Disordered Proteinaceous Machines.," *Chem. Rev.*, Apr. 2014.

[28] A. Lange, R. E. Mills, C. J. Lange, M. Stewart, S. E. Devine, and A. H. Corbett, "Classical nuclear localization signals: definition, function, and interaction with importin alpha.," *J. Biol. Chem.*, vol. 282, no. 8, pp. 5101–5, Feb. 2007.

[29] R. Bayliss, T. Littlewood, and M. Stewart, "Structural basis for the interaction between FxFG nucleoporin repeats and importin-beta in nuclear trafficking.," *Cell*, vol. 102, no. 1, pp. 99–108, Jul. 2000.

[30] W. Yang and S. M. Musser, "Nuclear import time and transport efficiency depend on importin beta concentration.," *J. Cell Biol.*, vol. 174, no. 7, pp. 951–61, Sep. 2006.

[31] W. Yang, J. Gelles, and S. M. Musser, "Imaging of single-molecule translocation through nuclear pore complexes.," *Proc. Natl. Acad. Sci. U. S. A.*, vol. 101, no. 35, pp. 12887–92, Aug. 2004.

[32] S. J. Lee, Y. Matsuura, S. M. Liu, and M. Stewart, "Structural basis for nuclear import complex dissociation by RanGTP.," *Nature*, vol. 435, no. 7042, pp. 693–6, Jun. 2005.

[33] M. Stewart, "Molecular mechanism of the nuclear protein import cycle.," *Nat. Rev. Mol. Cell Biol.*, vol. 8, no. 3, pp. 195–208, Mar. 2007.

[34] R. B. Kopito and M. Elbaum, "Reversibility in nucleocytoplasmic transport.," *Proc. Natl. Acad. Sci. U. S. A.*, vol. 104, no. 31, pp. 12743–8, Jul. 2007.

[35] R. B. Kopito and M. Elbaum, "Nucleocytoplasmic transport: a thermodynamic mechanism.," *HFSP J.*, vol. 3, no. 2, pp. 130–41, Jan. 2009.

[36] M. Hieda, T. Tachibana, F. Yokoya, S. Kose, N. Imamoto, and Y. Yoneda, "A monoclonal antibody to the COOH-terminal acidic portion of Ran inhibits both the recycling of Ran and nuclear protein import in living cells.," *J. Cell Biol.*, vol. 144, no. 4, pp. 645–55, Feb. 1999.

[37] E. Izaurralde, U. Kutay, C. von Kobbe, I. W. Mattaj, and D. Görlich, "The asymmetric distribution of the constituents of the Ran system is essential for transport into and out of the nucleus.," *EMBO J.*, vol. 16, no. 21, pp. 6535–47, Nov. 1997.

[38] U. Fischer, J. Huber, W. C. Boelens, L. W. Mattajt, and R. Lührmann, "The HIV-1 Rev Activation Domain is a nuclear export signal that accesses an export pathway used by specific cellular RNAs," *Cell*, vol. 82, no. 3, pp. 475–483, Aug. 1995.

[39] T. Monecke, A. Dickmanns, and R. Ficner, "Allosteric control of the exportin CRM1 unraveled by crystal structure analysis," *FEBS J.*, p. n/a–n/a, May 2014.

[40] F. R. Bischoff and D. Görlich, "RanBP1 is crucial for the release of RanGTP from importin beta-related nuclear transport factors.," *FEBS Lett.*, vol. 419, no. 2–3, pp. 249–54, Dec. 1997.

[41] K. Ribbeck, G. Lipowsky, H. M. Kent, M. Stewart, and D. Görlich,

"NTF2 mediates nuclear import of Ran.," *EMBO J.*, vol. 17, no. 22, pp. 6587–6598, Nov. 1998.

[42] A. Smith, A. Brownawell, and I. G. Macara, "Nuclear import of Ran is mediated by the transport factor NTF2.," *Curr. Biol.*, vol. 8, no. 25, pp. 1403–1406, 1998.

[43] L. Renault, J. Kuhlmann, A. Henkel, and A. Wittinghofer, "Structural basis for guanine nucleotide exchange on Ran by the regulator of chromosome condensation (RCC1).," *Cell*, vol. 105, no. 2, pp. 245–55, Apr. 2001.

[44] P. Kalab, K. Weis, and R. Heald, "Visualization of a Ran-GTP gradient in interphase and mitotic Xenopus egg extracts.," *Science*, vol. 295, no. 5564, pp. 2452–6, Mar. 2002.

[45] D. Gorlich, M. J. Seewald, and K. Ribbeck, "Characterization of Ran-driven cargo transport and the RanGTPase system by kinetic measurements and computer simulation," *EMBO J.*, vol. 22, no. 5, pp. 1088–1100, 2003.

[46] M. V Nachury and K. Weis, "The direction of transport through the nuclear pore can be inverted.," *Proc. Natl. Acad. Sci. U. S. A.*, vol. 96, no. 17, pp. 9622–7, Aug. 1999.

[47] O. Peleg and R. Y. H. Lim, "Converging on the function of intrinsically disordered nucleoporins in the nuclear pore complex.," *Biol. Chem.*, vol. 391, no. 7, pp. 719–30, Jul. 2010.

[48] L. A. Strawn, T. Shen, N. Shulga, D. S. Goldfarb, and S. R. Wente, "Minimal nuclear pore complexes define FG repeat domains essential for transport.," *Nat. Cell Biol.*, vol. 6, no. 3, pp. 197–206, Mar. 2004.

[49] S. R. Solmaz, R. Chauhan, G. Blobel, and I. Melčák, "Molecular architecture of the transport channel of the nuclear pore complex.,"

Cell, vol. 147, no. 3, pp. 590–602, Oct. 2011.

[50] P. Tompa, "Intrinsically unstructured proteins.," *Trends Biochem. Sci.*, vol. 27, no. 10, pp. 527–33, Oct. 2002.

[51] a K. Dunker, I. Silman, V. N. Uversky, and J. L. Sussman, "Function and structure of inherently disordered proteins.," *Curr. Opin. Struct. Biol.*, vol. 18, no. 6, pp. 756–64, Dec. 2008.

[52] J. Yamada, J. L. Phillips, S. Patel, G. Goldfien, A. Calestagne-Morelli, H. Huang, R. Reza, J. Acheson, V. V Krishnan, S. Newsam, A. Gopinathan, E. Y. Lau, M. E. Colvin, V. N. Uversky, and M. F. Rexach, "A bimodal distribution of two distinct categories of intrinsically disordered structures with separate functions in FG nucleoporins.," *Mol. Cell. Proteomics*, vol. 9, no. 10, pp. 2205–24, Oct. 2010.

[53] V. N. Uversky and A. K. Dunker, "Multiparametric analysis of intrinsically disordered proteins: looking at intrinsic disorder through compound eyes.," *Anal. Chem.*, vol. 84, no. 5, pp. 2096–104, Mar. 2012.

[54] Y. Huang and Z. Liu, "Kinetic advantage of intrinsically disordered proteins in coupled folding-binding process: a critical assessment of the 'fly-casting' mechanism.," *J. Mol. Biol.*, vol. 393, no. 5, pp. 1143–59, Nov. 2009.

[55] H.-X. Zhou, "Intrinsic disorder: signaling via highly specific but short-lived association.," *Trends Biochem. Sci.*, vol. 37, no. 2, pp. 43–8, Feb. 2012.

[56] N. Srinivasan and S. Kumar, "Ordered and disordered proteins as nanomaterial building blocks.," *Wiley Interdiscip. Rev. Nanomed. Nanobiotechnol.*, vol. 4, no. 2, pp. 204–18, 2012.

[57] S. W. Kowalczyk, L. Kapinos, T. R. Blosser, T. Magalhães, P. van Nies, R. Y. H. Lim, and C. Dekker, "Single-molecule transport across an

individual biomimetic nuclear pore complex.," *Nat. Nanotechnol.*, vol. 6, no. 7, pp. 433–8, Jul. 2011.

[58] T. Jovanovic-Talisman, J. Tetenbaum-Novatt, A. S. McKenney, A. Zilman, R. Peters, M. P. Rout, and B. T. Chait, "Artificial nanopores that mimic the transport selectivity of the nuclear pore complex.," *Nature*, vol. 457, no. 7232, pp. 1023–7, Feb. 2009.

[59] R. Y. H. Lim, N.-P. Huang, J. Köser, J. Deng, K. H. A. Lau, K. Schwarz-Herion, B. Fahrenkrog, and U. Aebi, "Flexible phenylalanine-glycine nucleoporins as entropic barriers to nucleocytoplasmic transport.," *Proc. Natl. Acad. Sci. U. S. A.*, vol. 103, no. 25, pp. 9512–7, Jun. 2006.

[60] R. Y. H. Lim, B. Fahrenkrog, J. Köser, K. Schwarz-Herion, J. Deng, and U. Aebi, "Nanomechanical basis of selective gating by the nuclear pore complex.," *Science*, vol. 318, no. 5850, pp. 640–3, Oct. 2007.

[61] S. S. Patel, B. J. Belmont, J. M. Sante, and M. F. Rexach, "Natively unfolded nucleoporins gate protein diffusion across the nuclear pore complex.," *Cell*, vol. 129, no. 1, pp. 83–96, Apr. 2007.

[62] J. Tetenbaum-Novatt, L. E. Hough, R. Mironska, A. S. McKenney, and M. P. Rout, "Nucleocytoplasmic Transport: A Role for Nonspecific Competition in Karyopherin-Nucleoporin Interactions," *Mol. Cell. Proteomics*, vol. 11, no. 5, pp. 31–46, May 2012.

[63] D. Xu, A. Farmer, and Y. M. Chook, "Recognition of nuclear targeting signals by Karyopherin-β proteins," *Curr. Opin. Struct. Biol.*, pp. 1–9, Oct. 2010.

[64] T. a Isgro and K. Schulten, "Binding dynamics of isolated nucleoporin repeat regions to importin-beta.," *Structure*, vol. 13, no. 12, pp. 1869–79, Dec. 2005.

[65] C. Fasting, C. a Schalley, M. Weber, O. Seitz, S. Hecht, B. Koksch, J. Dernedde, C. Graf, E.-W. Knapp, and R. Haag, "Multivalency as a chemical organization and action principle.," *Angew. Chem. Int. Ed. Engl.*, vol. 51, no. 42, pp. 10472–98, Oct. 2012.

[66] R. J. Pieters, "Maximising multivalency effects in protein-carbohydrate interactions.," *Org. Biomol. Chem.*, vol. 7, no. 10, pp. 2013–25, May 2009.

[67] B. R. Miller, M. Powers, M. Park, W. Fischer, and D. J. Forbes, "Identification of a new vertebrate nucleoporin, Nup188, with the use of a novel organelle trap assay.," *Mol. Biol. Cell*, vol. 11, no. 10, pp. 3381–96, Oct. 2000.

[68] C. C. Malbon, "Insulin signalling: putting the 'G-' in protein–protein interactions," *Biochem. J.*, vol. 380, no. 3, p. e11, Jun. 2004.

[69] N. a Sallee, G. M. Rivera, J. E. Dueber, D. Vasilescu, R. D. Mullins, B. J. Mayer, and W. a Lim, "The pathogen protein EspF(U) hijacks actin polymerization using mimicry and multivalency.," *Nature*, vol. 454, no. 7207, pp. 1005–8, Aug. 2008.

[70] P. Li, S. Banjade, H.-C. Cheng, S. Kim, B. Chen, L. Guo, M. Llaguno, J. V Hollingsworth, D. S. King, S. F. Banani, P. S. Russo, Q.-X. Jiang, B. T. Nixon, and M. K. Rosen, "Phase transitions in the assembly of multivalent signalling proteins.," *Nature*, vol. 483, no. 7389, pp. 336–40, Mar. 2012.

[71] G. Cingolani, C. Petosa, K. Weis, and C. W. Müller, "Structure of importin-beta bound to the IBB domain of importin-alpha.," *Nature*, vol. 399, no. 6733, pp. 221–9, May 1999.

[72] J. K. Forwood, A. Lange, U. Zachariae, M. Marfori, C. Preast, H. Grubmüller, M. Stewart, A. H. Corbett, and B. Kobe, "Quantitative structural analysis of importin-β flexibility: paradigm for solenoid

protein structures.," *Structure*, vol. 18, no. 9, pp. 1171–83, Sep. 2010.

[73] G. V Dubacheva, T. Curk, B. M. Mognetti, R. Auzély-Velty, D. Frenkel, and R. P. Richter, "Superselective targeting using multivalent polymers.," *J. Am. Chem. Soc.*, vol. 136, no. 5, pp. 1722–5, Feb. 2014.

[74] F. J. Martinez-Veracoechea and D. Frenkel, "Designing super selectivity in multivalent nano-particle binding.," *Proc. Natl. Acad. Sci. U. S. A.*, vol. 108, no. 27, pp. 10963–8, Jul. 2011.

[75] S. Knecht, D. Ricklin, A. N. Eberle, and B. Ernst, "Oligohis-tags: mechanisms of binding to Ni2+-NTA surfaces.," *J. Mol. Recognit.*, vol. 22, no. 4, pp. 270–9, 2009.

[76] A. Perl, A. Gomez-Casado, D. Thompson, H. H. Dam, P. Jonkheijm, D. N. Reinhoudt, and J. Huskens, "Gradient-driven motion of multivalent ligand molecules along a surface functionalized with multiple receptors.," *Nat. Chem.*, vol. 3, no. 4, pp. 317–22, Apr. 2011.

[77] T. K. Dam and C. F. Brewer, "Effects of clustered epitopes in multivalent ligand-receptor interactions.," *Biochemistry*, vol. 47, no. 33, pp. 8470–6, Aug. 2008.

[78] R. Peters, "Translocation through the nuclear pore: Kaps pave the way.," *Bioessays*, vol. 31, no. 4, pp. 466–77, Apr. 2009.

[79] G. Chatel, S. H. Desai, A. L. Mattheyses, M. a Powers, and B. Fahrenkrog, "Domain topology of nucleoporin Nup98 within the nuclear pore complex.," *J. Struct. Biol.*, vol. 177, no. 1, pp. 81–9, Jan. 2012.

[80] M. P. Rout, J. D. Aitchison, a Suprapto, K. Hjertaas, Y. Zhao, and B. T. Chait, "The yeast nuclear pore complex: composition, architecture, and transport mechanism.," *J. Cell Biol.*, vol. 148, no. 4, pp. 635–51, Feb. 2000.

[81] C. E. Atkinson, A. L. Mattheyses, M. Kampmann, and S. M. Simon, "Conserved spatial organization of FG domains in the nuclear pore complex.," *Biophys. J.*, vol. 104, no. 1, pp. 37–50, Jan. 2013.

[82] F. Cardarelli, L. Lanzano, and E. Gratton, "Capturing directed molecular motion in the nuclear pore complex of live cells.," *Proc. Natl. Acad. Sci. U. S. A.*, vol. 109, no. 25, pp. 9863–8, Jun. 2012.

[83] V. N. Uversky, "Natively unfolded proteins: a point where biology waits for physics.," *Protein Sci.*, vol. 11, no. 4, pp. 739–56, Apr. 2002.

[84] S. Frey, R. P. Richter, and D. Görlich, "FG-rich repeats of nuclear pore proteins form a three-dimensional meshwork with hydrogel-like properties.," *Science*, vol. 314, no. 5800, pp. 815–7, Nov. 2006.

[85] S. Frey and D. Görlich, "FG/FxFG as well as GLFG repeats form a selective permeability barrier with self-healing properties.," *EMBO J.*, vol. 28, no. 17, pp. 2554–67, Sep. 2009.

[86] S. Milles, K. Huy Bui, C. Koehler, M. Eltsov, M. Beck, and E. A. Lemke, "Facilitated aggregation of FG nucleoporins under molecular crowding conditions.," *EMBO Rep.*, vol. 14, no. 2, pp. 178–83, Feb. 2013.

[87] K. Ribbeck and D. Görlich, "The permeability barrier of nuclear pore complexes appears to operate via hydrophobic exclusion.," *EMBO J.*, vol. 21, no. 11, pp. 2664–71, Jun. 2002.

[88] A. a Labokha, S. Gradmann, S. Frey, B. B. Hülsmann, H. Urlaub, M. Baldus, and D. Görlich, "Systematic analysis of barrier-forming FG hydrogels from Xenopus nuclear pore complexes.," *EMBO J.*, pp. 1–15, Nov. 2012.

[89] S. Frey and D. Görlich, "A saturated FG-repeat hydrogel can reproduce the permeability properties of nuclear pore complexes.," *Cell*, vol. 130,

no. 3, pp. 512–23, Aug. 2007.

[90] C. Ader, S. Frey, W. Maas, H. B. Schmidt, D. Görlich, and M. Baldus, "Amyloid-like interactions within nucleoporin FG hydrogels.," *Proc. Natl. Acad. Sci. U. S. A.*, vol. 107, no. 14, pp. 6281–5, Apr. 2010.

[91] M. Petri, S. Frey, A. Menzel, D. Görlich, and S. Techert, "Structural Characterization of Nanoscale Meshworks within a Nucleoporin FG Hydrogel.," *Biomacromolecules*, May 2012.

[92] J. Ma, Z. Liu, N. Michelotti, S. Pitchiaya, R. Veerapaneni, J. R. Androsavich, N. G. Walter, and W. Yang, "High-resolution three-dimensional mapping of mRNA export through the nuclear pore," *Nat. Commun.*, vol. 4, pp. 1–9, Sep. 2013.

[93] J. Ma, A. Goryaynov, A. Sarma, and W. Yang, "Self-regulated viscous channel in the nuclear pore complex.," *Proc. Natl. Acad. Sci. U. S. A.*, vol. 109, no. 19, pp. 7326–31, May 2012.

[94] J. Fiserova, S. a Richards, S. R. Wente, and M. W. Goldberg, "Facilitated transport and diffusion take distinct spatial routes through the nuclear pore complex.," *J. Cell Sci.*, Jul. 2010.

[95] M. Rout, "Virtual gating and nuclear transport: the hole picture," *Trends Cell Biol.*, vol. 13, no. 12, pp. 622–628, Dec. 2003.

[96] I. Macara, "Transport into and out of the nucleus," *Microbiol. Mol. Biol. Rev.*, vol. 65, no. 4, 2001.

[97] J. M. Rogers, A. Steward, and J. Clarke, "Folding and binding of an intrinsically disordered protein: fast, but not 'diffusion-limited'.," *J. Am. Chem. Soc.*, vol. 135, no. 4, pp. 1415–22, Jan. 2013.

[98] K. Luby-Phelps, "Cytoarchitecture and physical properties of

cytoplasm: volume, viscosity, diffusion, intracellular surface area.," *Int. Rev. Cytol.*, vol. 192, pp. 189–221, Jan. 2000.

[99] S. T. Milner, "Polymer brushes.," *Science*, vol. 251, no. 4996, pp. 905–14, Feb. 1991.

[100] K. Chattopadhyay, E. L. Elson, and C. Frieden, "The kinetics of conformational fluctuations in an unfolded protein measured by fluorescence methods.," *Proc. Natl. Acad. Sci. U. S. A.*, vol. 102, pp. 2385–2389, 2005.

[101] R. L. Schoch, L. E. Kapinos, and R. Y. H. Lim, "Nuclear transport receptor binding avidity triggers a self-healing collapse transition in FG-nucleoporin molecular brushes.," *Proc. Natl. Acad. Sci. U. S. A.*, vol. 109, no. 42, pp. 16911–6, Oct. 2012.

[102] R. L. Schoch, L. E. Kapinos, and R. Y. H. Lim, "Nuclear transport receptor binding avidity triggers a self-healing collapse transition in FG-nucleoporin molecular brushes.," *Proc. Natl. Acad. Sci. U. S. A.*, vol. 109, no. 42, pp. 16911–6, Oct. 2012.

[103] A. Paradise, M. K. Levin, G. Korza, and J. H. Carson, "Significant proportions of nuclear transport proteins with reduced intracellular mobilities resolved by fluorescence correlation spectroscopy," *J Mol Biol*, vol. 365, no. 1, pp. 50–65, 2007.

[104] L. E. Kapinos, R. L. Schoch, R. S. Wagner, K. D. Schleicher, and R. Y. H. Lim, "Karyopherin-centric control of nuclear pores based on molecular occupancy and kinetic analysis of multivalent binding with FG nucleoporins.," *Biophys. J.*, vol. 106, no. 8, pp. 1751–62, Apr. 2014.

[105] R. Gamini, W. Han, J. E. Stone, and K. Schulten, "Assembly of nsp1 nucleoporins provides insight into nuclear pore complex gating.," *PLoS Comput. Biol.*, vol. 10, no. 3, p. e1003488, Mar. 2014.

[106] O. G. Berg and P. H. von Hippel, "Diffusion-controlled macromolecular interactions.," *Annu. Rev. Biophys. Biophys. Chem.*, vol. 14, pp. 131–60, Jan. 1985.

[107] J. Gorman and E. C. Greene, "Visualizing one-dimensional diffusion of proteins along DNA," *Nat. Struct. Mol. Biol.*, vol. 15, no. 8, pp. 768–774, 2008.

[108] A. Revzin and P. H. Von Hippel, "Direct measurement of association constants for the binding of Escherichia coli lac repressor to non-operator DNA," *Biochemistry*, vol. 16, no. 22, pp. 4769–4776, 1977.

[109] P. L. deHaseth, T. M. Lohman, and M. T. Record, "Nonspecific interaction of lac repressor with DNA: an association reaction driven by counterion release.," *Biochemistry*, vol. 16, pp. 4783–4790, 1977.

[110] Y. Yuan, O. D. Velev, and A. M. Lenhoff, "Mobility of adsorbed proteins studied by fluorescence recovery after photobleaching," *Langmuir*, vol. 19, pp. 3705–3711, 2003.

[111] R. Peters, "Functionalization of a nanopore: the nuclear pore complex paradigm.," *Biochim. Biophys. Acta*, vol. 1793, no. 10, pp. 1533–9, Oct. 2009.

[112] A. V. Chechkin, I. M. Zaid, M. A. Lomholt, I. M. Sokolov, and R. Metzler, "Bulk-mediated surface diffusion along a cylinder: Propagators and crossovers," *Phys. Rev. E - Stat. Nonlinear, Soft Matter Phys.*, vol. 79, 2009.

[113] M. G. Opferman, R. D. Coalson, D. Jasnow, and A. Zilman, "Morphology of polymer brushes infiltrated by attractive nanoinclusions of various sizes.," *Langmuir*, vol. 29, no. 27, pp. 8584–91, Jul. 2013.

[114] M. G. Opferman, R. D. Coalson, D. Jasnow, and A. Zilman,

"Morphological control of grafted polymer films via attraction to small nanoparticle inclusions," *Phys. Rev. E*, vol. 86, no. 3, p. 031806, Sep. 2012.

[115] M. Kahms, J. Hüve, R. Wesselmann, J. C. Farr, V. Baumgärtel, and R. Peters, "Lighting up the nuclear pore complex.," *Eur. J. Cell Biol.*, vol. 90, no. 9, pp. 751–8, Sep. 2011.

[116] M. Tokunaga, N. Imamoto, and K. Sakata-Sogawa, "Highly inclined thin illumination enables clear single-molecule imaging in cells," *Nat. Methods*, vol. 5, no. 2, pp. 159–161, 2008.

[117] J. Ma and W. Yang, "Three-dimensional distribution of transient interactions in the nuclear pore complex obtained from single-molecule snapshots.," *Proc. Natl. Acad. Sci. U. S. A.*, vol. 107, no. 16, pp. 7305–10, Apr. 2010.

[118] B. Zeitler and K. Weis, "The FG-repeat asymmetry of the nuclear pore complex is dispensable for bulk nucleocytoplasmic transport in vivo.," *J. Cell Biol.*, vol. 167, no. 4, pp. 583–90, Nov. 2004.

[119] A. R. Lowe, J. J. Siegel, P. Kalab, M. Siu, K. Weis, and J. T. Liphardt, "Selectivity mechanism of the nuclear pore complex characterized by single cargo tracking.," *Nature*, vol. 467, no. 7315, pp. 600–3, Sep. 2010.

[120] R. Bayliss, K. Ribbeck, D. Akin, H. M. Kent, C. M. Feldherr, D. Görlich, and M. Stewart, "Interaction between NTF2 and xFxFG-containing nucleoporins is required to mediate nuclear import of RanGDP.," *J. Mol. Biol.*, vol. 293, no. 3, pp. 579–93, Oct. 1999.

[121] B. Fahrenkrog, B. Maco, A. M. Fager, J. Köser, U. Sauder, K. S. Ullman, and U. Aebi, "Domain-specific antibodies reveal multiple-site topology of Nup153 within the nuclear pore complex.," *J. Struct. Biol.*, vol. 140, no. 1–3, pp. 254–67, 2002.

[122] R. Y. H. Lim, J. Köser, N.-P. Huang, K. Schwarz-Herion, and U. Aebi, "Nanomechanical interactions of phenylalanine-glycine nucleoporins studied by single molecule force-volume spectroscopy.," *J. Struct. Biol.*, vol. 159, no. 2, pp. 277–89, Aug. 2007.

[123] J. Kyte and R. Doolittle, "A simple method for displaying the hydropathic character of a protein," *J. Mol. Biol.*, vol. 157, no. 1, pp. 105–132, May 1982.

[124] S. Xu and M. a Powers, "In vivo analysis of human nucleoporin repeat domain interactions.," *Mol. Biol. Cell*, vol. 24, no. 8, pp. 1222–31, Apr. 2013.

[125] B. Xue, R. L. Dunbrack, R. W. Williams, A. K. Dunker, and V. N. Uversky, "PONDR-FIT: a meta-predictor of intrinsically disordered amino acids.," *Biochim. Biophys. Acta*, vol. 1804, no. 4, pp. 996–1010, Apr. 2010.

[126] O. Tcherkasskaya, E. A. Davidson, and V. N. Uversky, "Biophysical Constraints for Protein Structure Prediction," *J. Proteome Res.*, vol. 2, no. 1, pp. 37–42, Feb. 2003.

[127] R. L. Schoch and R. Y. H. Lim, "Non-interacting molecules as innate structural probes in surface plasmon resonance.," *Langmuir*, vol. 29, no. 12, pp. 4068–76, Mar. 2013.

[128] M. Tagliazucchi, O. Peleg, M. Kröger, Y. Rabin, and I. Szleifer, "Effect of charge, hydrophobicity, and sequence of nucleoporins on the translocation of model particles through the nuclear pore complex.," *Proc. Natl. Acad. Sci. U. S. A.*, Feb. 2013.

[129] L. J. Colwell, M. P. Brenner, and K. Ribbeck, "Charge as a selection criterion for translocation through the nuclear pore complex.," *PLoS Comput. Biol.*, vol. 6, no. 4, p. e1000747, Jan. 2010.

[130] A. Goryaynov and W. Yang, "Role of molecular charge in nucleocytoplasmic transport.," *PLoS One*, vol. 9, no. 2, p. e88792, Jan. 2014.

[131] T. Franosch, M. Grimm, M. Belushkin, F. M. Mor, G. Foffi, L. Forró, and S. Jeney, "Resonances arising from hydrodynamic memory in Brownian motion.," *Nature*, vol. 478, no. 7367, pp. 85–8, Oct. 2011.

[132] R. Huang, I. Chavez, K. M. Taute, B. Lukić, S. Jeney, M. G. Raizen, and E.-L. Florin, "Direct observation of the full transition from ballistic to diffusive Brownian motion in a liquid," *Nat. Phys.*, vol. 7, no. 7, pp. 576–580, Mar. 2011.

[133] S. Jeney, E. H. K. Stelzer, H. Grubmüller, and E.-L. Florin, "Mechanical properties of single motor molecules studied by three-dimensional thermal force probing in optical tweezers.," *Chemphyschem*, vol. 5, no. 8, pp. 1150–8, Aug. 2004.

[134] T. Franosch and S. Jeney, "Persistent correlation of constrained colloidal motion," *Phys. Rev. E*, vol. 79, no. 3, p. 031402, Mar. 2009.

[135] S. Jeney, B. Lukić, C. Guzmán, and L. Forró, "Probing Hydrodynamic Fluctuations with a Brownian Particle," in *Nanotechnology Volume 6: Nanoprobes*, 1st ed., H. Fuchs, Ed. Wiley-VCH, 2009.

[136] K. C. Neuman and S. M. Block, "Optical trapping.," *Rev. Sci. Instrum.*, vol. 75, no. 9, pp. 2787–809, Sep. 2004.

[137] D. J. Stevenson, F. Gunn-Moore, and K. Dholakia, "Light forces the pace: optical manipulation for biophotonics.," *J. Biomed. Opt.*, vol. 15, no. 4, p. 041503, 2012.

[138] F. Gittes and C. Schmidt, "Interference model for back-focal-plane displacement detection in optical tweezers," *Opt. Lett.*, vol. 23, no. 1, pp. 7–9, 1998.

[139] A. Rohrbach and E. H. K. Stelzer, "Three-dimensional position detection of optically trapped dielectric particles," *J. Appl. Phys.*, vol. 91, no. 8, p. 5474, 2002.

[140] S. Jeney, F. Mor, R. Koszali, L. Forró, and V. T. Moy, "Monitoring ligand-receptor interactions by photonic force microscopy.," *Nanotechnology*, vol. 21, no. 25, p. 255102, Jun. 2010.

[141] M. W. Allersma, F. Gittes, M. J. deCastro, R. J. Stewart, and C. F. Schmidt, "Two-dimensional tracking of ncd motility by back focal plane interferometry.," *Biophys. J.*, vol. 74, no. 2 Pt 1, pp. 1074–85, Feb. 1998.

[142] E. J. G. Peterman, M. a. van Dijk, L. C. Kapitein, and C. F. Schmidt, "Extending the bandwidth of optical-tweezers interferometry," *Rev. Sci. Instrum.*, vol. 74, no. 7, p. 3246, 2003.

[143] J. T. Hyotyla, J. Deng, and R. Y. H. Lim, "Synthetic protein targeting by the intrinsic biorecognition functionality of poly(ethylene glycol) using PEG antibodies as biohybrid molecular adaptors.," *ACS Nano*, vol. 5, no. 6, pp. 5180–7, Jun. 2011.

[144] K. Okuda, I. Urabe, Y. Yamada, and H. Okada, "Reaction of glutaraldehyde with amino and thiol compounds," *J. Ferment. Bioeng.*, vol. 71, no. 2, pp. 100–105, 1991.

[145] I. Migneault, C. Dartiguenave, M. J. Bertrand, and K. C. Waldron, "Glutaraldehyde: behavior in aqueous solution, reaction with proteins, and application to enzyme crosslinking.," *Biotechniques*, vol. 37, no. 5, pp. 790–6, 798–802, Nov. 2004.

[146] Bangs Laboratories Inc, "Ask 'The Particle Doctor,'" 2011.

[147] I. Gromova and J. Celis, "Protein detection in gels by silver staining: A procedure compatible with mass-spectrometry," *Cell Biol. A Lab. Handb.*, vol. 4, pp. 421–429, 2006.

[148] T. Fester, R. H. Berg, and C. G. Taylor, "An easy method using glutaraldehyde-introduced fluorescence for the microscopic analysis of plant biotrophic interactions.," *J. Microsc.*, vol. 231, no. 2, pp. 342–8, Aug. 2008.

[149] J. Razumovitch, K. de França, F. Kehl, M. Wiki, W. Meier, and C. Vebert, "Optimal hybridization efficiency upon immobilization of oligonucleotide double helices.," *J. Phys. Chem. B*, vol. 113, no. 24, pp. 8383–90, Jun. 2009.

[150] N. B. Eisele, F. I. Andersson, S. Frey, and R. P. Richter, "Viscoelasticity of thin biomolecular films: a case study on nucleoporin phenylalanine-glycine repeats grafted to a histidine-tag capturing QCM-D sensor.," *Biomacromolecules*, vol. 13, no. 8, pp. 2322–32, Aug. 2012.

[151] N. B. Eisele, S. Frey, J. Piehler, D. Görlich, and R. P. Richter, "Ultrathin nucleoporin phenylalanine-glycine repeat films and their interaction with nuclear transport receptors.," *EMBO Rep.*, vol. 11, no. 5, pp. 366–72, May 2010.

[152] K. Berg-Sørensen and H. Flyvbjerg, "Power spectrum analysis for optical tweezers," *Rev. Sci. Instrum.*, vol. 75, no. 3, p. 594, 2004.

[153] S. F. Tolić-No rrelykke, E. Schaffer, J. Howard, F. S. Pavone, F. Julicher, and H. Flyvbjerg, "Calibration of optical tweezers with positional detection in the back focal plane," *Rev. Sci. Instrum.*, vol. 77, no. 10, p. 103101, 2006.

[154] P. M. Hansen, I. M. Tolić-Nørrelykke, H. Flyvbjerg, and K. Berg-Sørensen, "tweezercalib 2.0: Faster version of MatLab package for

precise calibration of optical tweezers," *Comput. Phys. Commun.*, vol. 174, no. 6, pp. 518–520, Mar. 2006.

[155] A. Rohrbach, "Stiffness of Optical Traps: Quantitative Agreement between Experiment and Electromagnetic Theory," *Phys. Rev. Lett.*, vol. 95, no. 16, pp. 1–4, Oct. 2005.

[156] A. Einstein, "Über die von der molekularkinetischen Theorie der Wärme geforderte Bewegung von in ruhenden Flüssigkeiten suspendierten Teilchen," *Ann. Phys.*, vol. 322, no. 8, pp. 549–560, 1905.

[157] B. Lukić, S. Jeney, C. Tischer, a. Kulik, L. Forró, and E.-L. Florin, "Direct Observation of Nondiffusive Motion of a Brownian Particle," *Phys. Rev. Lett.*, vol. 95, no. 16, p. 160601, Oct. 2005.

[158] A. V Oppenheim and R. W. Schafer, *Discrete-time signal processing*, 3rd ed., vol. 5. Prentice Hall Signal Processing, 2009.

[159] T. T. Perkins, "Optical traps for single molecule biophysics: a primer," *Laser Photonics Rev.*, vol. 3, no. 1–2, pp. 203–220, Feb. 2009.

[160] K. Feldman, G. Hähner, N. D. Spencer, P. Harder, and M. Grunze, "Probing Resistance to Protein Adsorption of Oligo(ethylene glycol)-Terminated Self-Assembled Monolayers by Scanning Force Microscopy," *J. Am. Chem. Soc.*, vol. 121, no. 43, pp. 10134–10141, Nov. 1999.

[161] J. Happel and H. Brenner, *Low Reynolds Number Hydrodynamics*, vol. 1, no. 12. Dordrecht: Springer Netherlands, 1981.

[162] H. Brenner, "The slow motion of a sphere through a viscous fluid towards a plane surface," *Chem. Eng. Sci.*, vol. 16, no. 3–4, pp. 242–251, Dec. 1961.

[163] E. Schäffer, S. F. Nørrelykke, and J. Howard, "Surface forces and drag coefficients of microspheres near a plane surface measured with optical tweezers.," *Langmuir*, vol. 23, no. 7, pp. 3654–65, Mar. 2007.

[164] A. Becskei and I. W. Mattaj, "Quantitative models of nuclear transport.," *Curr. Opin. Cell Biol.*, vol. 17, no. 1, pp. 27–34, Feb. 2005.

[165] N. A. Burnham, R. J. Colton, and H. M. Pollock, "Interpretation issues in force microscopy," *J. Vac. Sci. Technol. A Vacuum, Surfaces, Film.*, vol. 9, no. 4, p. 2548, Jul. 1991.

[166] B. Cappella and G. Dietler, "Force-distance curves by atomic force microscopy," *Surf. Sci. Rep.*, vol. 34, no. 1–3, pp. 1–104, Jan. 1999.

[167] S. L. Eichmann, G. Meric, J. C. Swavola, and M. A. Bevan, "Diffusing colloidal probes of protein-carbohydrate interactions," *Langmuir*, vol. 29, no. 7, pp. 2299–2310, 2013.

[168] S. Otsuka, S. Iwasaka, Y. Yoneda, K. Takeyasu, and S. H. Yoshimura, "Individual binding pockets of importin-beta for FG-nucleoporins have different binding properties and different sensitivities to RanGTP.," *Proc. Natl. Acad. Sci. U. S. A.*, vol. 105, no. 42, pp. 16101–6, Oct. 2008.

[169] W. N. Everett, H.-J. Wu, S. G. Anekal, H.-J. Sue, and M. a Bevan, "Diffusing colloidal probes of protein and synthetic macromolecule interactions.," *Biophys. J.*, vol. 92, no. 3, pp. 1005–13, Feb. 2007.

[170] S. Jeney, B. Lukić, J. a. Kraus, T. Franosch, and L. Forró, "Anisotropic Memory Effects in Confined Colloidal Diffusion," *Phys. Rev. Lett.*, vol. 100, no. 24, p. 240604, Jun. 2008.

[171] J. Sprakel, J. van der Gucht, M. Cohen Stuart, and N. Besseling, "Rouse Dynamics of Colloids Bound to Polymer Networks," *Phys. Rev. Lett.*, vol. 99, no. 20, pp. 1–4, Nov. 2007.

[172] S. L. Dettmer, U. F. Keyser, and S. Pagliara, "Local characterization of hindered Brownian motion by using digital video microscopy and 3D particle tracking.," *Rev. Sci. Instrum.*, vol. 85, no. 2, p. 023708, Feb. 2014.

[173] W. N. Everett, D. J. Beltran-Villegas, and M. a Bevan, "Concentrated diffusing colloidal probes of Ca2+-dependent cadherin interactions.," *Langmuir*, vol. 26, no. 24, pp. 18976–84, Dec. 2010.

[174] J. Gelles, B. J. Schnapp, and M. P. Sheetz, "Tracking kinesin-driven movements with nanometre-scale precision.," *Nature*, vol. 331, no. 6155, pp. 450–3, Mar. 1988.

[175] M. Sheetz and J. Spudich, "Movement of myosin-coated fluorescent beads on actin cables in vitro," *Nature*, 1983.

[176] M. a. Bevan and S. L. Eichmann, "Optical microscopy measurements of kT-scale colloidal interactions," *Curr. Opin. Colloid Interface Sci.*, vol. 16, no. 2, pp. 149–157, Apr. 2011.

[177] R. B. Liebert and D. C. Prieve, "Species-specific long range interactions between receptor/ligand pairs.," *Biophys. J.*, vol. 69, no. 1, pp. 66–73, Jul. 1995.

[178] D. A. Schafer, J. Gelles, M. P. Sheetz, and R. Landick, "Transcription by single molecules of RNA polymerase observed by light microscopy.," *Nature*, vol. 352, no. 6334, pp. 444–8, Aug. 1991.

[179] B. C. Carter, G. T. Shubeita, and S. P. Gross, "Tracking single particles: a user-friendly quantitative evaluation.," *Phys. Biol.*, vol. 2, no. 1, pp. 60–72, Mar. 2005.

[180] J. Crocker, D. Grier, and I. Introduction, "Methods of digital video

microscopy for colloidal studies," *J. Colloid Interface Sci.*, vol. 310, no. 179, pp. 298–310, 1996.

[181] H. Qian, M. P. Sheetz, and E. L. Elson, "Single particle tracking. Analysis of diffusion and flow in two-dimensional systems.," *Biophys. J.*, vol. 60, no. 4, pp. 910–21, Oct. 1991.

[182] T. Savin and P. S. Doyle, "Static and dynamic errors in particle tracking microrheology.," *Biophys. J.*, vol. 88, no. 1, pp. 623–38, Jan. 2005.

[183] X. Michalet, "Mean square displacement analysis of single-particle trajectories with localization error: Brownian motion in an isotropic medium," *Phys. Rev. E*, vol. 82, no. 4, p. 041914, Oct. 2010.

[184] V. Bormuth, V. Varga, J. Howard, and E. Schäffer, "Protein friction limits diffusive and directed movements of kinesin motors on microtubules.," *Science*, vol. 325, no. 5942, pp. 870–3, Aug. 2009.

[185] L.-C. Tu, G. Fu, A. Zilman, and S. M. Musser, "Large cargo transport by nuclear pores: implications for the spatial organization of FG-nucleoporins.," *EMBO J.*, vol. 32, no. 24, pp. 3220–30, Dec. 2013.

[186] K. Jacobson, A. Ishihara, and R. Inman, "Lateral diffusion of proteins in membranes," *Annu. Rev. Physiol.*, vol. 49, no. 1, pp. 163–175, 1987.

[187] S. Santer and J. Rühe, "Motion of nano-objects on polymer brushes," *Polymer (Guildf).*, vol. 45, no. 25, pp. 8279–8297, Nov. 2004.

[188] V. N. Uversky, "Intrinsically disordered proteins from A to Z.," *Int. J. Biochem. Cell Biol.*, vol. 43, no. 8, pp. 1090–103, Aug. 2011.

[189] A. Pierres, A. M. Benoliel, and P. Bongrand, "Measuring the lifetime of bonds made between surface-linked molecules.," *J. Biol. Chem.*, vol.

270, no. 44, pp. 26586–92, Nov. 1995.

[190] D. Janasek, J. Franzke, and A. Manz, "Scaling and the design of miniaturized chemical-analysis systems.," *Nature*, vol. 442, no. 7101, pp. 374–80, Jul. 2006.

[191] H. Craighead, "Future lab-on-a-chip technologies for interrogating individual molecules.," *Nature*, vol. 442, no. 7101, pp. 387–93, Jul. 2006.

[192] G. M. Whitesides, "The origins and the future of microfluidics," *Nature*, vol. 442, no. 7101, pp. 368–373, 2006.

[193] R. Bizzarri, F. Cardarelli, M. Serresi, and F. Beltram, "Fluorescence recovery after photobleaching reveals the biochemistry of nucleocytoplasmic exchange.," *Anal. Bioanal. Chem.*, vol. 403, no. 8, pp. 2339–51, Jun. 2012.

[194] S. Kim and M. Elbaum, "Enzymatically Driven Transport: A Kinetic Theory for Nuclear Export," *Biophys. J.*, vol. 105, no. 9, pp. 1997–2005, Nov. 2013.

[195] N. I. Kiskin, J. P. Siebrasse, and R. Peters, "Optical microwell assay of membrane transport kinetics.," *Biophys. J.*, vol. 85, no. 4, pp. 2311–22, Oct. 2003.

[196] S. Fan, V. Fogg, Q. Wang, X.-W. Chen, C.-J. Liu, and B. Margolis, "A novel Crumbs3 isoform regulates cell division and ciliogenesis via importin beta interactions.," *J. Cell Biol.*, vol. 178, no. 3, pp. 387–98, Jul. 2007.

[197] S. R. Bond and C. C. Naus, "RF-Cloning.org: an online tool for the design of restriction-free cloning projects.," *Nucleic Acids Res.*, vol. 40, no. Web Server issue, pp. W209–13, Jul. 2012.

8 List of publications

Schleicher, K. D., Dettmer, S. L., Kapinos, L. E., Pagliara, S., Keyser, U. F., Jeney, S., & Lim, R. Y. Selective transport control on molecular velcro made from intrinsically disordered proteins. *Nat. Nanotechnol,* 9(7), 525-530 (**2014**).

Kapinos, L. E., Schoch, R. L., Wagner, R. S., **Schleicher, K. D.** & Lim, R. Y. H. Karyopherin-Centric Control of Nuclear Pores Based on Molecular Occupancy and Kinetic Analysis of Multivalent Binding with FG Nucleoporins. *Biophys. J.* 106**,** 1751–1762 (**2014**).

9 Acknowledgments

First and foremost, my gratitude belongs to my PhD advisor Roderick Lim, for giving me the chance to work in his lab, and for the benefit of the doubt by introducing a biologist to the world of physical science. I learned many things during my time as PhD in his lab, and am especially grateful for the freedom I was given to explore science on my own. I thank him for his guidance and his constant support of my project.

Special thanks go to Sylvia Jeney, who supported my beginnings in photonic force microscopy and was always there to provide assistance, and in addition took the time to be on my committee. Thanks go to Michael Elbaum, for discussing my project with me, for the invitation to the Weizmann institute, for the skiing trips and for being on my committee.

Many thanks go to all my colleagues in the lab, Bref, Janne, Lajko, Matthias, Philipp, Rafael, Marko, Marija and Larisa, who went out of their ways more than once to help me. I want to thank everyone not only for their support, but also for the activities besides science and, most importantly, their friendship. Thanks go to all the rest of the lab, Chantal, Yusuke, Selim, and team Artidis.

In particular, I thank L. E. Kapinos and R. L. Schoch who, in the framework of their recently published study [104], collected and analyzed all SPR data presented here. I further thank R.L. Schoch, M. Grimm and F.M. Mor for assistance and useful discussions of PFM data. My gratitude goes to Stefano Pagliara and especially Simon Lee Dettmer for his great collaboration and analysis of the probe videos as well as Professor Ulrich F. Keyser for his support of the particle tracking experiments. Thanks to Thomas Pfohl and Natalja Strelnikova for photolithography, designing the photomasks and for

producing the wafer masters. Acknowledgments go to Friederike Benning for the production of cNup153-stripes, fluorescent Kap-probes and fluorescence microscopy. I thank the Imaging Core facility (IMCF, University of Basel) and in particular Alexia Isabelle Ferrand for the technical assistance provided on the 3i spinning disc. Thanks to Chantal Rencurel for her help during my cloning efforts.

10 Appendix

Table 10-1 – Complete result of the pull-down in Figure 2-8 as identified by mass-spectrometry.

Band	MW [kDa]	calc pI	Score	Name (Protein from e. coli)
1	77.5	5.38	516.09	Elongation factor G OS=Escherichia coli O139:H28 (strain E24377A / ETEC) GN=fusA PE=3 SV=1 - [EFG_ECO24]
	90.60	5.15	224.08	Outer membrane protein assembly factor yaeT OS=Escherichia coli O1:K1 / APEC GN=yaeT PE=3 SV=1 - [YAET_ECOK1]
	95.50	5.52	193.06	Chaperone protein ClpB OS=Escherichia coli O157:H7 GN=clpB PE=3 SV=1 - [CLPB_ECO57]
	66.1	5.17	142.65	Dihydrolipoyllysine-residue acetyltransferase component of pyruvate dehydrogenase complex OS=Escherichia coli (strain K12) GN=aceF PE=1 SV=3 - [ODP2_ECOLI]
	95.9	5.81	119.06	Alanine--tRNA ligase OS=Escherichia coli O1:K1 / APEC GN=alaS PE=3 SV=1 - [SYA_ECOK1]
	84.7	5.92	91.24	5-methyltetrahydropteroyltriglutamate--homocysteine methyltransferase OS=Escherichia coli O1:K1 / APEC GN=metE PE=3 SV=1 - [METE_ECOK1]
	97.3	6.07	74.75	Translation initiation factor IF-2 OS=Escherichia coli O139:H28 (strain E24377A / ETEC) GN=infB PE=3 SV=1 - [IF2_ECO24]
	89.6	5.30	66.86	LPS-assembly protein lptD OS=Escherichia coli O1:K1 / APEC GN=lptD PE=3 SV=1 - [LPTD_ECOK1]
	43.3	5.45	59.72	RecName: Full=Elongation factor Tu 1; Short=EF-Tu 1; - [EFTU1_ECO24]
	89.9	6.06	57.60	DNA gyrase subunit B OS=Escherichia coli O157:H7 GN=gyrB PE=3 SV=2 - [GYRB_ECO57]
	87.4	5.06	46.85	Phosphoenolpyruvate synthase OS=Escherichia coli (strain K12) GN=ppsA PE=1 SV=5 - [PPSA_ECOLI]
	39.3	4.96	45.68	Outer membrane protein F OS=Escherichia coli (strain K12) GN=ompF PE=1 SV=1 - [OMPF_ECOLI]
	70.2	4.79	45.52	RNA polymerase sigma factor rpoD OS=Escherichia coli (strain K12) GN=rpoD PE=1 SV=2 - [RPOD_ECOLI]
	69.1	7.03	41.49	Glutathione import ATP-binding protein GsiA OS=Escherichia coli O1:K1 / APEC GN=gsiA PE=3 SV=2 - [GSIA_ECOK1]
	24.3	5.34	28.18	RecName: Full=Stringent starvation protein A; - [SSPA_ECO57]
2	72.2	5.67	427.39	Transketolase 1 OS=Escherichia coli (strain K12) GN=tktA PE=1 SV=5 - [TKT1_ECOLI]
	64.4	6.27	405.85	Succinate dehydrogenase flavoprotein subunit OS=Escherichia coli O157:H7 GN=sdhA PE=3 SV=1 - [DHSA_ECO57]
	76.2	5.86	169.31	Methionyl-tRNA synthetase OS=Escherichia coli O139:H28 (strain E24377A / ETEC) GN=metG PE=3 SV=1 - [SYM_ECO24]

	61.1	4.98	159.17	RecName: Full=30S ribosomal protein S1; - [RS1_ECO57]
	71.4	5.21	126.95	Chaperone protein htpG OS=Escherichia coli O1:K1 / APEC GN=htpG PE=3 SV=1 - [HTPG_ECOK1]
	69.1	4.97	115.35	RecName: Full=Chaperone protein dnaK;AltName: Full=Heat shock protein 70;AltName: Full=Heat shock 70 kDa protein;AltName: Full=HSP70; - [DNAK_ECO24]
	57.3	4.94	115.15	RecName: Full=60 kDa chaperonin 1;AltName: Full=Protein Cpn60 1;AltName: Full=groEL protein 1; - [CH601_ECOK1]
	63.8	5.85	102.96	Trehalose-6-phosphate hydrolase OS=Escherichia coli (strain K12) GN=treC PE=3 SV=3 - [TREC_ECOLI]
	69.5	6.64	83.25	tRNA uridine 5-carboxymethylaminomethyl modification enzyme MnmG OS=Escherichia coli O139:H28 (strain E24377A / ETEC) GN=mnmG PE=3 SV=1 - [MNMG_ECO24
	73.9	6.19	74.45	Threonyl-tRNA synthetase OS=Escherichia coli O139:H28 (strain E24377A / ETEC) GN=thrS PE=3 SV=1 - [SYT_ECO24]
	74.2	6.80	73.26	Bifunctional polymyxin resistance protein ArnA OS=Escherichia coli O139:H28 (strain E24377A / ETEC) GN=arnA PE=3 SV=1 - [ARNA_ECO24]
	77.5	5.74	71.61	Peptidyl-dipeptidase dcp OS=Escherichia coli (strain K12) GN=dcp PE=1 SV=4 - [DCP_ECOLI]
	41.1	5.22	53.64	Phosphoglycerate kinase OS=Escherichia coli O139:H28 (strain E24377A / ETEC) GN=pgk PE=3 SV=1 - [PGK_ECO24]
	66.1	5.17	45.68	Dihydrolipoyllysine-residue acetyltransferase component of pyruvate dehydrogenase complex OS=Escherichia coli (strain K12) GN=aceF PE=1 SV=3 - [ODP2_ECOLI]
	69.1	7.03	44.50	Glutathione import ATP-binding protein GsiA OS=Escherichia coli O1:K1 / APEC GN=gsiA PE=3 SV=2 - [GSIA_ECOK1]
	67.5	6.62	40.78	1-deoxy-D-xylulose-5-phosphate synthase OS=Escherichia coli O139:H28 (strain E24377A / ETEC) GN=dxs PE=3 SV=1 - [DXS_ECO24]
	63.3	6.24	40.52	Hydrogenase-4 component G OS=Escherichia coli (strain K12) GN=hyfG PE=1 SV=1 - [HYFG_ECOLI]
	43.3	5.45	39.19	RecName: Full=Elongation factor Tu 1; Short=EF-Tu 1; - [EFTU1_ECO24]
	14.9	9.63	32.92	50S ribosomal protein L11 OS=Escherichia coli O139:H28 (strain E24377A / ETEC) GN=rplK PE=3 SV=1 - [RL11_ECO24]
3	70.5	8.72	755.82	Cold-shock DEAD box protein A OS=Escherichia coli O6:H1 (strain CFT073 / ATCC 700928 / UPEC) GN=deaD PE=3 SV=2 - [DEAD_ECOL6]
	57.3	4.94	608.83	RecName: Full=60 kDa chaperonin 1;AltName: Full=Protein Cpn60 1;AltName: Full=groEL protein 1; - [CH601_ECOK1]
	65.7	5.19	345.91	Chaperone protein HscA OS=Escherichia coli O139:H28 (strain E24377A / ETEC) GN=hscA PE=3 SV=1 - [HSCA_ECO24]
	63.4	6.28	296.32	Glutamine--tRNA ligase OS=Escherichia coli O139:H28 (strain E24377A / ETEC) GN=glnS PE=3 SV=1 - [SYQ_ECO24]
	64.4	6.27	249.21	Succinate dehydrogenase flavoprotein subunit OS=Escherichia coli O157:H7 GN=sdhA PE=3 SV=1 - [DHSA_ECO57]
	77.1	5.26	200.62	Oligopeptidase A OS=Escherichia coli (strain K12) GN=prlC PE=3 SV=3 - [OPDA_ECOLI]

	57.6	5.24	192.02	Lysyl-tRNA synthetase OS=Escherichia coli O6 GN=lysS PE=3 SV=2 - [SYK1_ECOL6]
	65.8	5.77	147.25	Aspartyl-tRNA synthetase OS=Escherichia coli O139:H28 (strain E24377A / ETEC) GN=aspS PE=3 SV=1 - [SYD_ECO24]
	68.2	6.42	138.89	NADH-quinone oxidoreductase subunit C/D OS=Escherichia coli (strain K12) GN=nuoC PE=1 SV=3 - [NUOCD_ECOLI]
	57.8	5.24	123.02	Lysyl-tRNA synthetase, heat inducible OS=Escherichia coli O157:H7 GN=lysU PE=3 SV=2 - [SYK2_ECO57]
	43.3	5.45	80.12	RecName: Full=Elongation factor Tu 1; Short=EF-Tu 1; - [EFTU1_ECO24]
	47.1	5.77	54.97	D-tagatose-1,6-bisphosphate aldolase subunit gatZ OS=Escherichia coli O139:H28 (strain E24377A / ETEC) GN=gatZ PE=3 SV=1 - [GATZ_ECO24]
	54.8	4.64	52.91	Transcription elongation protein nusA OS=Escherichia coli O157:H7 GN=nusA PE=3 SV=1 - [NUSA_ECO57]
	32.3	5.77	47.44	Malate dehydrogenase OS=Escherichia coli O139:H28 (strain E24377A / ETEC) GN=mdh PE=3 SV=1 - [MDH_ECO24]
	14.6	9.39	33.14	Protein traK OS=Escherichia coli GN=traK PE=3 SV=4 - [TRAK5_ECOLX]
4	43.3	5.45	981.87	RecName: Full=Elongation factor Tu 1; Short=EF-Tu 1; - [EFTU1_ECO24]
	41.1	5.22	218.39	Phosphoglycerate kinase OS=Escherichia coli O139:H28 (strain E24377A / ETEC) GN=pgk PE=3 SV=1 - [PGK_ECO24]
	44.5	7.36	160.20	N-acetylglucosamine repressor OS=Escherichia coli O157:H7 GN=nagC PE=3 SV=1 - [NAGC_ECO57]
	43.0	6.09	147.79	3-oxoacyl-[acyl-carrier-protein] synthase 2 OS=Escherichia coli O157:H7 GN=fabF PE=3 SV=2 - [FABF_ECO57]
	44.8	6.16	134.77	UDP-N-acetylglucosamine 1-carboxyvinyltransferase OS=Escherichia coli O139:H28 (strain E24377A / ETEC) GN=murA PE=3 SV=1 - [MURA_ECO24]
	45.1	6.37	125.20	Cysteine desulfurase OS=Escherichia coli O139:H28 (strain E24377A / ETEC) GN=iscS PE=3 SV=1 - [ISCS_ECO24]
	45.3	6.48	98.49	Serine hydroxymethyltransferase OS=Escherichia coli O139:H28 (strain E24377A / ETEC) GN=glyA PE=3 SV=1 - [GLYA_ECO24]
	47.5	5.81	94.44	Tyrosyl-tRNA synthetase OS=Escherichia coli O139:H28 (strain E24377A / ETEC) GN=tyrS PE=3 SV=1 - [SYY_ECO24]
	42.6	5.54	93.62	3-oxoacyl-[acyl-carrier-protein] synthase 1 OS=Escherichia coli O6 GN=fabB PE=3 SV=1 - [FABB_ECOL6]
	39.1	5.86	92.76	Fructose-bisphosphate aldolase class 2 OS=Escherichia coli O157:H7 GN=fbaA PE=3 SV=2 - [ALF_ECO57]
	48.6	6.40	90.56	NADP-specific glutamate dehydrogenase OS=Escherichia coli (strain K12) GN=gdhA PE=1 SV=1 - [DHE4_ECOLI]
	40.6	5.39	85.56	DNA polymerase III subunit beta OS=Escherichia coli O157:H7 GN=dnaN PE=3 SV=1 - [DPO3B_ECO57]
	46.1	5.59	77.31	3-phosphoshikimate 1-carboxyvinyltransferase OS=Escherichia coli O139:H28 (strain E24377A / ETEC) GN=aroA PE=3 SV=1 - [AROA_ECO24]

	43.1	5.97	68.35	Putative 8-amino-7-oxononanoate synthase/2-amino-3-ketobutyrate coenzyme A ligase OS=Escherichia coli O157:H7 GN=Z5044 PE=3 SV=1 - [BIKB_ECO57]
	32.3	5.77	67.42	Malate dehydrogenase OS=Escherichia coli O139:H28 (strain E24377A / ETEC) GN=mdh PE=3 SV=1 - [MDH_ECO24]
	43.5	6.14	67.08	UDP-glucose 6-dehydrogenase OS=Escherichia coli GN=ugd PE=3 SV=1 - [UDG8_ECOLX]
	47.6	6.62	66.59	RecName: Full=D-amino acid dehydrogenase small subunit; EC=1.4.99.1; - [DADA_ECO24]
	40.5	5.77	60.23	dTDP-glucose 4,6-dehydratase 1 OS=Escherichia coli (strain K12) GN=rfbB PE=3 SV=2 - [RMLB1_ECOLI]
	40.1	9.51	59.95	Murein hydrolase activator NlpD OS=Escherichia coli (strain K12) GN=nlpD PE=1 SV=1 - [NLPD_ECOLI]
	44.0	5.14	57.81	Molybdopterin molybdenumtransferase OS=Escherichia coli (strain K12) GN=moeA PE=1 SV=1 - [MOEA_ECOLI]
	41.0	6.70	57.31	Maltose/maltodextrin import ATP-binding protein MalK OS=Escherichia coli O157:H7 GN=malK PE=3 SV=1 - [MALK_ECO57]
	39.6	4.96	49.45	GTP-dependent nucleic acid-binding protein engD OS=Escherichia coli O157:H7 GN=engD PE=3 SV=2 - [ENGD_ECO57]
	43.1	6.99	49.29	Ribosomal RNA large subunit methyltransferase N OS=Escherichia coli O139:H28 (strain E24377A / ETEC) GN=rlmN PE=3 SV=1 - [RLMN_ECO24]
	45.5	6.43	46.99	Protein HflK OS=Escherichia coli O157:H7 GN=hflK PE=3 SV=1 - [HFLK_ECO57]
	44.4	5.35	37.65	Phosphopentomutase OS=Escherichia coli O1:K1 / APEC GN=deoB PE=3 SV=1 - [DEOB_ECOK1]
	45.6	5.48	36.72	Enolase OS=Escherichia coli O139:H28 (strain E24377A / ETEC) GN=eno PE=3 SV=1 - [ENO_ECO24]
	45.5	6.25	32.43	Glutamate-pyruvate aminotransferase AlaA OS=Escherichia coli O6:H1 (strain CFT073 / ATCC 700928 / UPEC) GN=alaA PE=3 SV=1 - [ALAA_ECOL6]
	48.5	7.84	30.37	sn-glycerol-3-phosphate-binding periplasmic protein ugpB OS=Escherichia coli O1:K1 / APEC GN=ugpB PE=3 SV=1 - [UGPB_ECOK1]
5	41.1	5.22	500.42	Phosphoglycerate kinase OS=Escherichia coli O139:H28 (strain E24377A / ETEC) GN=pgk PE=3 SV=1 - [PGK_ECO24]
	43.1	5.97	422.25	Putative 8-amino-7-oxononanoate synthase/2-amino-3-ketobutyrate coenzyme A ligase OS=Escherichia coli O157:H7 GN=Z5044 PE=3 SV=1 - [BIKB_ECO57]
	43.3	5.45	404.50	RecName: Full=Elongation factor Tu 1; Short=EF-Tu 1; - [EFTU1_ECO24]
	40.3	4.78	382.51	RecName: Full=Cell division protein ftsZ; - [FTSZ_ECO57]
	40.7	6.21	342.64	4-hydroxy-3-methylbut-2-en-1-yl diphosphate synthase OS=Escherichia coli O139:H28 (strain E24377A / ETEC) GN=ispG PE=3 SV=1 - [ISPG_ECO24]
	39.1	5.86	324.92	Fructose-bisphosphate aldolase class 2 OS=Escherichia coli O157:H7 GN=fbaA PE=3 SV=2 - [ALF_ECO57]

36.5	5.06	302.19	RecName: Full=DNA-directed RNA polymerase subunit alpha; Short=RNAP subunit alpha; EC=2.7.7.6;AltName: Full=Transcriptase subunit alpha;AltName: Full=RNA polymerase subunit alpha; - [RPOA_ECO24]
39.3	4.96	293.09	Outer membrane protein F OS=Escherichia coli (strain K12) GN=ompF PE=1 SV=1 - [OMPF_ECOLI]
43.1	6.68	194.53	P-protein OS=Escherichia coli O157:H7 GN=pheA PE=3 SV=1 - [PHEA_ECO57]
43.5	5.77	181.22	Aspartate aminotransferase OS=Escherichia coli (strain K12) GN=aspC PE=1 SV=1 - [AAT_ECOLI]
41.4	6.70	178.33	Erythronate-4-phosphate dehydrogenase OS=Escherichia coli (strain ATCC 8739 / DSM 1576 / Crooks) GN=pdxB PE=3 SV=1 - [PDXB_ECOLC]
41.4	5.52	163.89	RecName: Full=Succinyl-CoA ligase [ADP-forming] subunit beta; EC=6.2.1.5;AltName: Full=Succinyl-CoA synthetase subunit beta; Short=SCS-beta; - [SUCC_ECO24]
39.0	5.97	133.16	PhoH-like protein OS=Escherichia coli O157:H7 GN=ybeZ PE=3 SV=2 - [PHOL_ECO57]
37.9	5.19	125.97	RecName: Full=Protein recA;AltName: Full=Recombinase A; - [RECA_ECO24]
35.8	5.50	115.29	Fructose-1,6-bisphosphatase class 2 OS=Escherichia coli O6:H1 (strain CFT073 / ATCC 700928 / UPEC) GN=glpX PE=3 SV=1 - [GLPX_ECOL6]
44.4	8.28	110.74	D-alanyl-D-alanine carboxypeptidase dacA OS=Escherichia coli O157:H7 GN=dacA PE=3 SV=1 - [DACA_ECO57]
42.3	7.42	103.61	Putative ABC transporter periplasmic-binding protein ydcS OS=Escherichia coli (strain K12) GN=ydcS PE=3 SV=1 - [YDCS_ECOLI]
38.6	6.89	102.67	Lactose operon repressor OS=Escherichia coli (strain K12) GN=lacI PE=1 SV=3 - [LACI_ECOLI]
41.6	6.71	100.04	UDP-4-amino-4-deoxy-L-arabinose--oxoglutarate aminotransferase OS=Escherichia coli O139:H28 (strain E24377A / ETEC) GN=arnB PE=3 SV=1 - [ARNB_ECO24]
43.5	5.48	96.43	Aromatic-amino-acid aminotransferase OS=Escherichia coli (strain K12) GN=tyrB PE=1 SV=1 - [TYRB_ECOLI]
41.0	7.84	96.06	Chaperone protein DnaJ OS=Escherichia coli O139:H28 (strain E24377A / ETEC) GN=dnaJ PE=3 SV=1 - [DNAJ_ECO24]
37.4	6.38	83.62	Galactitol-1-phosphate 5-dehydrogenase OS=Escherichia coli O157:H7 GN=gatD PE=3 SV=1 - [GATD_ECO57]
39.0	6.54	76.18	Glutamate 5-kinase OS=Escherichia coli O139:H28 (strain E24377A / ETEC) GN=proB PE=3 SV=1 - [PROB_ECO24]
49.3	8.56	74.64	Protease do OS=Escherichia coli O157:H7 GN=degP PE=3 SV=1 - [DEGP_ECO57]
39.8	5.74	71.00	Phosphoserine aminotransferase OS=Escherichia coli O139:H28 (strain E24377A / ETEC) GN=serC PE=3 SV=1 - [SERC_ECO24]
39.1	7.05	66.39	Alanine racemase, biosynthetic OS=Escherichia coli (strain K12) GN=alr PE=1 SV=1 - [ALR1_ECOLI]
57.3	4.94	57.79	RecName: Full=60 kDa chaperonin 1;AltName: Full=Protein Cpn60 1;AltName: Full=groEL protein 1; - [CH601_ECOK1]

	47.6	6.62	54.61	RecName: Full=D-amino acid dehydrogenase small subunit; EC=1.4.99.1; - [DADA_ECO24]
	69.1	4.97	50.21	RecName: Full=Chaperone protein dnaK;AltName: Full=Heat shock protein 70;AltName: Full=Heat shock 70 kDa protein;AltName: Full=HSP70; - [DNAK_ECO24]
	69.1	7.03	41.11	Glutathione import ATP-binding protein GsiA OS=Escherichia coli O1:K1 / APEC GN=gsiA PE=3 SV=2 - [GSIA_ECOK1]
	45.3	4.86	38.99	Glutamate-1-semialdehyde 2,1-aminomutase OS=Escherichia coli O139:H28 (strain E24377A / ETEC) GN=hemL PE=3 SV=1 - [GSA_ECO24]
	44.7	6.19	34.33	4-aminobutyrate aminotransferase PuuE OS=Escherichia coli (strain K12) GN=puuE PE=1 SV=1 - [PUUE_ECOLI]
	43.1	6.99	30.85	Ribosomal RNA large subunit methyltransferase N OS=Escherichia coli O139:H28 (strain E24377A / ETEC) GN=rlmN PE=3 SV=1 - [RLMN_ECO24]
	32.7	5.20	30.34	Nicotinate-nucleotide pyrophosphorylase [carboxylating] OS=Escherichia coli (strain K12) GN=nadC PE=1 SV=7 - [NADC_ECOLI]
	37.1	5.86	29.07	L-asparaginase 1 OS=Escherichia coli O157:H7 GN=ansA PE=3 SV=1 - [ASPG1_ECO57]
	96.2	7.20	27.51	Outer membrane usher protein focD OS=Escherichia coli GN=focD PE=3 SV=1 - [FOCD_ECOLX]
	41.9	4.91	26.25	Lipoprotein yfgL OS=Escherichia coli (strain K12) GN=yfgL PE=1 SV=1 - [YFGL_ECOLI]
6	39.3	4.96	497.22	Outer membrane protein F OS=Escherichia coli (strain K12) GN=ompF PE=1 SV=1 - [OMPF_ECOLI]
	35.5	7.11	180.24	Glyceraldehyde-3-phosphate dehydrogenase A OS=Escherichia coli O157:H7 GN=gapA PE=3 SV=2 - [G3P1_ECO57]
	36.4	5.60	151.22	Adenosine deaminase OS=Escherichia coli O139:H28 (strain E24377A / ETEC) GN=add PE=3 SV=1 - [ADD_ECO24]
	36.0	9.85	150.81	Ribosomal large subunit pseudouridine synthase C OS=Escherichia coli (strain K12) GN=rluC PE=1 SV=1 - [RLUC_ECOLI]
	36.1	7.42	150.29	HTH-type transcriptional regulator CysB OS=Escherichia coli O157:H7 GN=cysB PE=3 SV=1 - [CYSB_ECO57]
	39.1	5.86	140.71	Fructose-bisphosphate aldolase class 2 OS=Escherichia coli O157:H7 GN=fbaA PE=3 SV=2 - [ALF_ECO57]
	32.3	5.77	132.48	Malate dehydrogenase OS=Escherichia coli O139:H28 (strain E24377A / ETEC) GN=mdh PE=3 SV=1 - [MDH_ECO24]
	30.6	5.44	117.37	NH(3)-dependent NAD(+) synthetase OS=Escherichia coli O139:H28 (strain E24377A / ETEC) GN=nadE PE=3 SV=1 - [NADE_ECO24]
	40.3	4.78	109.07	RecName: Full=Cell division protein ftsZ; - [FTSZ_ECO57]
	35.2	5.21	94.88	Transaldolase B OS=Escherichia coli O157:H7 GN=talB PE=3 SV=2 - [TALB_ECO57]
	34.8	5.72	71.94	6-phosphofructokinase isozyme 1 OS=Escherichia coli O157:H7 GN=pfkA PE=3 SV=1 - [K6PF1_ECO57]
	36.9	5.26	71.24	Rod shape-determining protein mreB OS=Escherichia coli O6 GN=mreB PE=3 SV=1 - [MREB_ECOL6]

37.4	6.54	68.37	GMP reductase OS=Escherichia coli O139:H28 (strain E24377A / ETEC) GN=guaC PE=3 SV=1 - [GUAC_ECO24]
38.8	6.05	65.28	3-dehydroquinate synthase OS=Escherichia coli O139:H28 (strain E24377A / ETEC) GN=aroB PE=3 SV=1 - [AROB_ECO24]
38.1	8.63	62.62	Uncharacterized protein ybjS OS=Escherichia coli (strain K12) GN=ybjS PE=4 SV=2 - [YBJS_ECOLI]
43.3	5.45	56.52	RecName: Full=Elongation factor Tu 1; Short=EF-Tu 1; - [EFTU1_ECO24]
37.4	6.74	52.17	Tryptophan--tRNA ligase OS=Escherichia coli (strain K12) GN=trpS PE=1 SV=3 - [SYW_ECOLI]
37.4	6.38	50.22	Galactitol-1-phosphate 5-dehydrogenase OS=Escherichia coli O157:H7 GN=gatD PE=3 SV=1 - [GATD_ECO57]
37.6	6.80	48.66	Ribosomal RNA small subunit methyltransferase C OS=Escherichia coli O1:K1 / APEC GN=rsmC PE=3 SV=1 - [RSMC_ECOK1]
36.0	7.94	45.34	Lipoyl synthase OS=Escherichia coli O139:H28 (strain E24377A / ETEC) GN=lipA PE=3 SV=1 - [LIPA_ECO24]
69.1	7.03	41.20	Glutathione import ATP-binding protein GsiA OS=Escherichia coli O1:K1 / APEC GN=gsiA PE=3 SV=2 - [GSIA_ECOK1]
32.4	5.36	38.76	6-phosphofructokinase isozyme 2 OS=Escherichia coli (strain K12) GN=pfkB PE=1 SV=2 - [K6PF2_ECOLI]

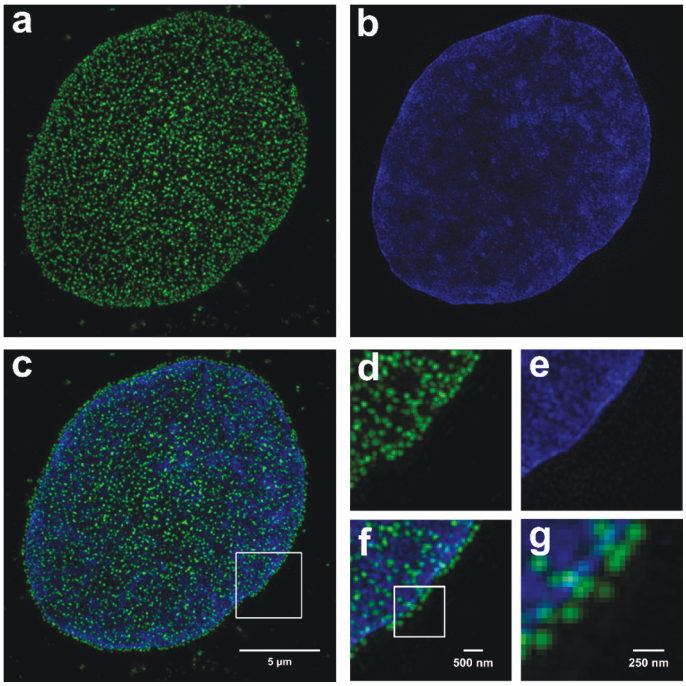

Figure 10-1 – Structured illumination microscopy of NPCs in fixed wt MDCK cells. SIM provides insight into NPC/NE integrity, average NPC copy number per cell (& per µm² NE) and nuclear volume. (**a**) Indirect immunofluorescence using a FXFG-repeat recognizing primary antibody (Mab414) and an Alexa488 conjugated secondary antibody reveals a dense NPC distribution throughout the NE. (**b**) DNA was stained with DAPI and the resulting signal was used to reconstruct the nuclear volume. (**c**) Merge of channels presented in (**a**) and (**b**). (**d-f**) 10x zoom-in on the nuclear envelope as indicated (white square in c). (**g**) Further 2x zoom-in on a region in (**f**) (white square) revealed individual NPCs as diffraction-limited spots. For illustrative purposes, all images are presented as 2D projections of the 3D-dataset.

High resolution three dimensional structured illumination microscopy (3D-SIM, Figure 10-1) of fixed MDCK t23 wt cells yields an average of approximately 3000 NPCs per cell (5±1 NPCs per µm² NE, Figure 10-1a) with a median nuclear volume of 717 µm² and ellipsoidal shape as derived from DAPI staining (Figure 10-1b and appendix, Figure 10-2). Notably, SIM results revealed that the height of a nucleus d_z can be expressed as $d_z = \frac{1}{2} d_y$, i.e. half of the smaller semi-principal axis in the horizontal plane (see appendix, Figure 10-2). Measurements from confocal stacks of living cells confirmed this result (see appendix, Figure 10-2). With this relation, it is

possible to estimate the nuclear volume of a single cell from 2D images in the horizontal plane.

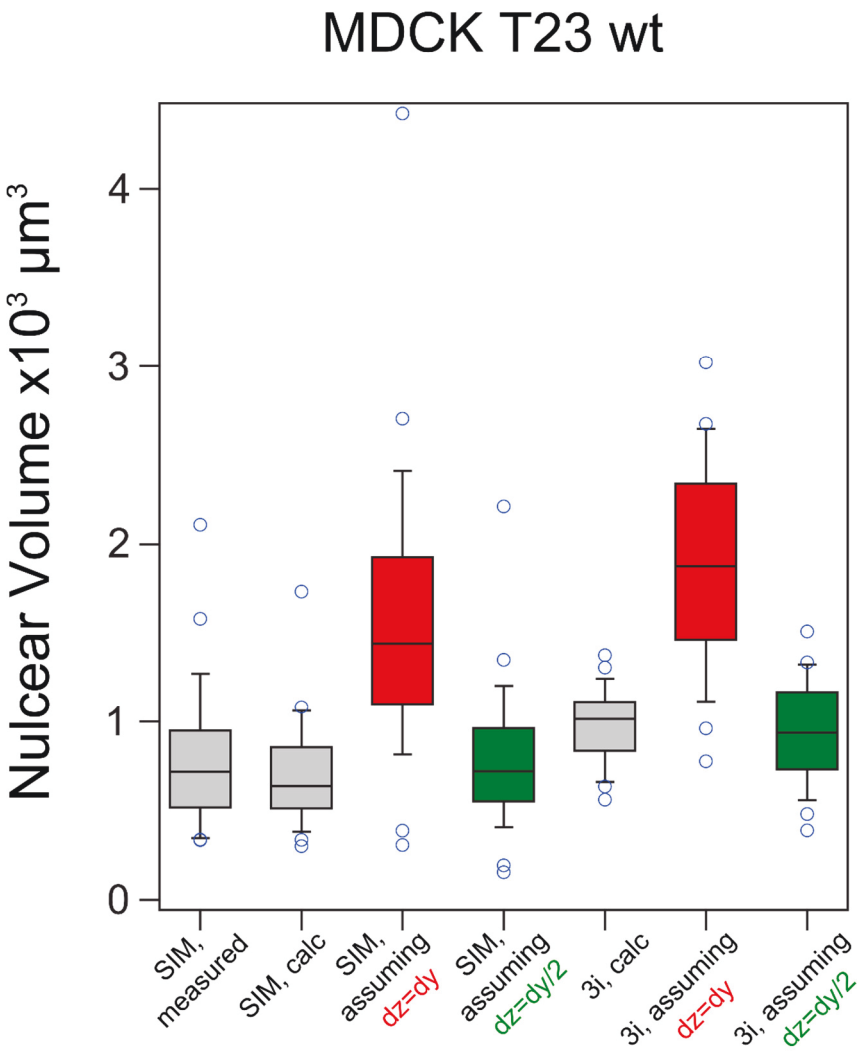

Figure 10-2 – Nuclear volume of MDCK t23 cells. Here, volume measurements based on SIM and DAPI staining agree with calculations based on the width of the defining axis of the nucleus assuming an ellipsoid ($V_N = \left(\frac{4\pi}{3}\right) r_x r_y r_z$). In contrast to a previous study performed in CHO cells [193], nuclear height d_z was related to the minor in-plane axis by $d_z = d_y/2$ (green) rather than $d_z = d_y$ (red). Confocal spinning

disc microscopy (3i) of EGFP and EGFP-M9 transfected MDCK t23 cells verified this relation.

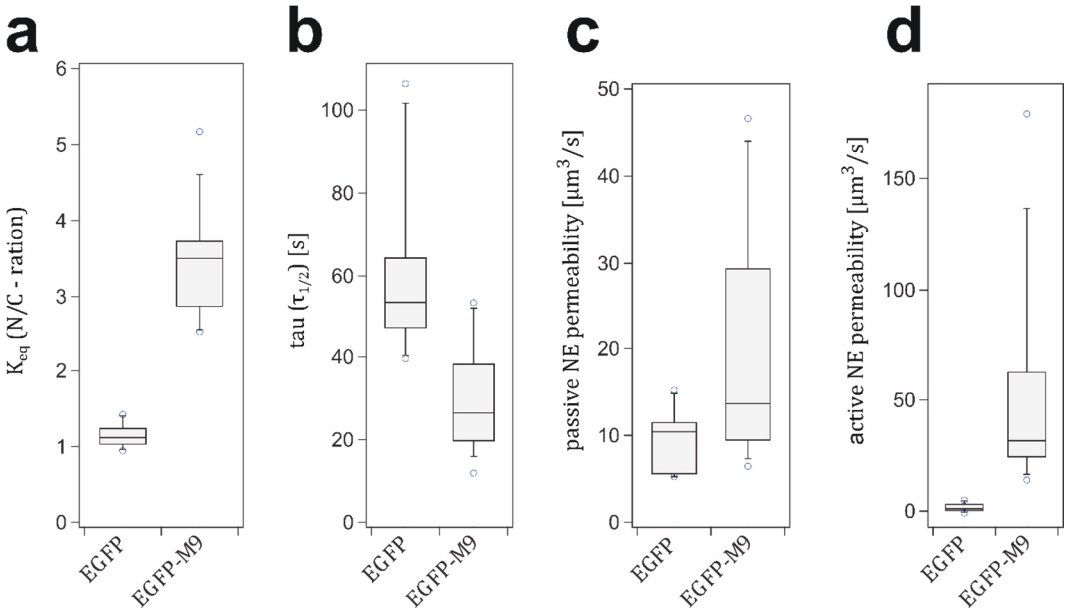

Figure 10-3 – Distribution of measured and calculated parameters from FRAP experiments. Further quantitative insight into NCT can be obtained by correlation of the measured quantities (**a**, **b**) with the nuclear volume [193] which allows for the calculation of permeability coefficient of the respective cargos used (**c**, **d**). Median values 1.1 and 3.5 (a); 54 s and 26 s (b); 10 µm³/s and 14 µm³/s (c); 1.1 µm³/s and 32 µm³/s (d) for passive (EGFP) and active (EGFP-M9) cargo, respectively.

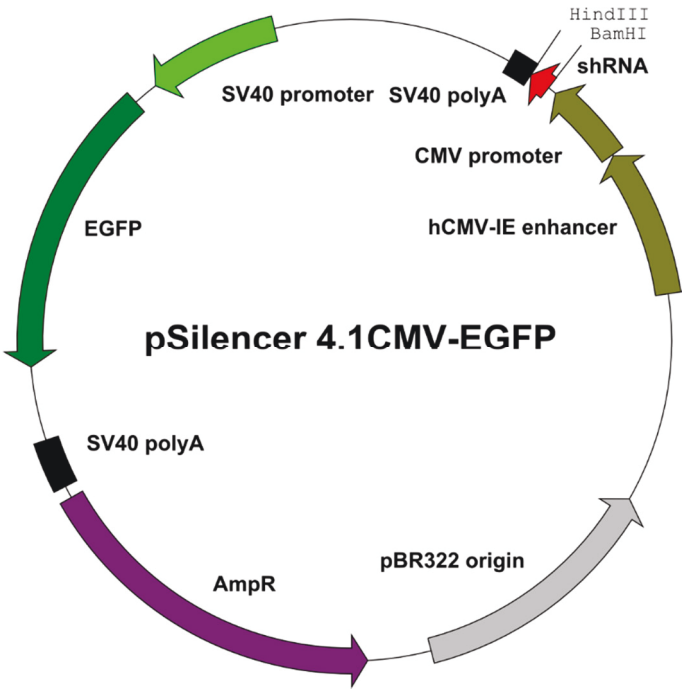

Figure 10-4 – Construct for Kapβ1 silencing and simultaneous EGFP expression. Adaptation of the pSilencer4.1-CMV.neo vector containing shRNA against canine Kapβ1 (a kind gift from Shuling Fan

[196]) was accomplished by exchanging the neomycin-resistance gene with EGFP from the pEGFP-C1 vector using a restriction-free cloning method [197] (available online via http://www.rf-cloning.org/) with primers 5'-CGA ACC CCA GAG TCC CGC TCA GCT TGT ACA GCT CGT CCA TGC-3' (forward) and 5'-AGA GAC AGG ATG AGG ATC GTT TCG CAT GGT GAG CAA GGG CGA G-3' (reverse), resulting in plasmid pSilencer4.1-CMV.EGFP.